THE JOURNAL OF PHYSICAL CHEMISTRY B

Feature Article

Cite This: J. Phys. Chem. B 2019, 123, 1453−1480

pubs.acs.org/JPCB

Integrated NMR, Fluorescence, and Molecular Dynamics Benchmark Study of Protein Mechanics and Hydrodynamics

Christina Möckel,[†,‡,#] Jakub Kubiak,[§,#] Oliver Schillinger,[‡,∥,#] Ralf Kühnemuth,[§] Dennis Della Corte,[‡] Gunnar F. Schröder,[‡,⊥] Dieter Willbold,[†,‡] Birgit Strodel,[*,‡,∥] Claus A. M. Seidel,[*,§] and Philipp Neudecker[*,†,‡]

[†]Institut für Physikalische Biologie, Heinrich-Heine-Universität Düsseldorf, 40225 Düsseldorf, Germany
[‡]Institute of Complex Systems (ICS-6: Structural Biochemistry), Forschungszentrum Jülich, 52425 Jülich, Germany
[§]Lehrstuhl für Molekulare Physikalische Chemie, Heinrich-Heine-Universität Düsseldorf, 40225 Düsseldorf, Germany
[∥]Institut für Theoretische Chemie und Computerchemie, Heinrich-Heine-Universität Düsseldorf, 40225 Düsseldorf, Germany
[⊥]Physics Department, Heinrich-Heine-Universität Düsseldorf, 40225 Düsseldorf, Germany

Supporting Information

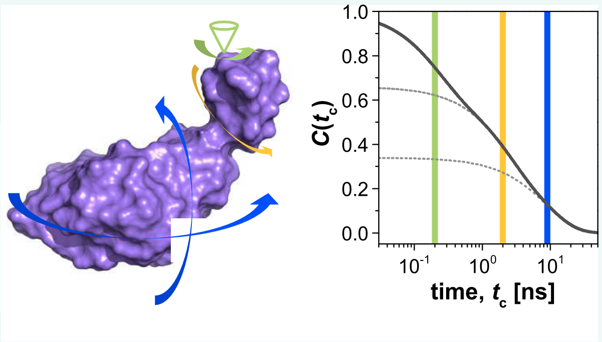

ABSTRACT: Understanding the function of a protein requires not only knowledge of its tertiary structure but also an understanding of its conformational dynamics. Nuclear magnetic resonance (NMR) spectroscopy, polarization-resolved fluorescence spectroscopy and molecular dynamics (MD) simulations are powerful methods to provide detailed insight into protein dynamics on multiple time scales by monitoring global rotational diffusion and local flexibility (order parameters) that are sensitive to inter- and intramolecular interactions, respectively. We present an integrated approach where data from these techniques are analyzed and interpreted within a joint theoretical description of depolarization and diffusion, demonstrating their conceptual similarities. This integrated approach is then applied to the autophagy-related protein GABARAP in its cytosolic form, elucidating its dynamics on the pico- to nanosecond time scale and its rotational and translational diffusion for protein concentrations spanning 9 orders of magnitude. We compare the dynamics of GABARAP as monitored by ^{15}N spin relaxation of the backbone amide groups, fluorescence anisotropy decays and fluorescence correlation spectroscopy of side chains labeled with BODIPY FL, and molecular movies of the protein from MD simulations. The recovered parameters agree very well between the distinct techniques if the different measurement conditions (probe localization, sample concentration) are taken into account. Moreover, we propose a method that compares the order parameters of the backbone and side chains to identify potential hinges for large-scale, functionally relevant intradomain motions, such as residues 27/28 at the interface between the two subdomains of GABARAP. In conclusion, the integrated concept of cross-fertilizing techniques presented here is fundamental to obtaining a comprehensive quantitative picture of multiscale protein dynamics and solvation. The possibility to employ these validated techniques under cellular conditions and combine them with fluorescence imaging opens up the perspective of studying the functional dynamics of GABARAP or other proteins in live cells.

1. INTRODUCTION

1.1. Protein Dynamics on the Pico- to Nanosecond Time Scale. Conformational dynamics is a prerequisite for proteins to be able to fold and exert their physiological functions. Understanding the physicochemical mechanisms underlying folding and function of a protein therefore requires knowledge of both structure and dynamics in atomic detail. Protein conformational dynamics is observed on a wide range of time scales.[1] By their structural origin and typical time scales, these dynamical processes can roughly be divided into three groups: (1) local backbone and side-chain motions, (2) conformational flexibility of secondary, tertiary, and supertertiary structural units, and (3) global rotational diffusion, depending on the total size and shape of the assembly (Figure 1A,B). On the most fundamental level, polypeptide chains in aqueous solution at ambient temperature are highly mobile on the pico- to nanosecond time scale unless these motions are restricted by stable tertiary interactions. In globular proteins with a stable tertiary fold the residual internal dynamics on the picosecond to nanosecond time scale such as side-chain rotations, hydrogen bond formation, and backbone motions in loops and at the termini can be separated conceptually from the overall rotational diffusion of the

Received: September 11, 2018
Revised: November 30, 2018
Published: December 10, 2018

DOI: 10.1021/acs.jpcb.8b08903
J. Phys. Chem. B 2019, 123, 1453−1480

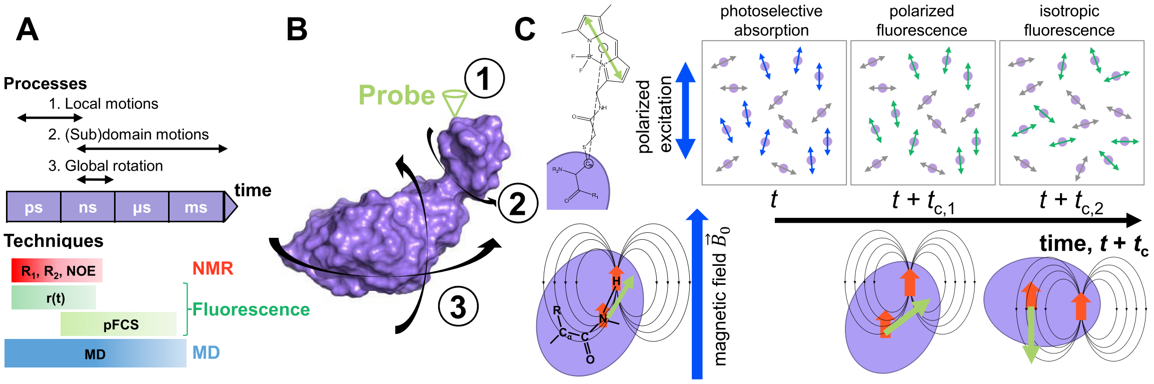

Figure 1. Protein dynamics and time scales sensed by our integrated approach. Protein dynamics is governed by motions on different time scales, as listed in (A) and sketched in (B). NMR and fluorescence spectroscopy and MD simulations are able to monitor these motions ranging from picoseconds to microseconds, using different probes, as shown in (C). The depolarization of the transition dipoles of chromophores is measured in fluorescence spectroscopy, the dipolar coupling between two spins allows the measurement of molecular reorientation in NMR spectroscopy, while in MD simulations the orientation of bonds is directly monitored in the protein dynamics trajectories.

molecule, which is governed by the hydrodynamic properties of the protein. If the protein is approximately spherical in shape, the rotational diffusion is isotropic and described by the global rotational correlation time ρ_{global}. It is typically of the order of several nanoseconds for moderately sized proteins and approximately proportional to the viscosity of the solvent and the molecular weight of the solute according to the Stokes−Einstein−Debye law.[2] By contrast, processes such as protein folding or other large-scale protein motions that involve significant rearrangements of larger secondary structure elements, subdomains or even entire domains relative to each other are often limited by the rate of intrachain diffusion and by sizable activation barriers and thus most commonly observed on the micro- to millisecond time scale or slower.[3,4]

For a variety of reasons a detailed knowledge of the picosecond to nanosecond dynamics of a protein is a key element in understanding its structural biology. First, identification of well-ordered and disordered regions of the polypeptide chain is an important step in the high-resolution structure determination by X-ray crystallography and/or NMR spectroscopy because the degree of disorder has serious implications for the interpretation of the experimental data (e.g., lack of crystal formation, electron density map, nuclear Overhauser effect (NOE) restraints) as well as of the resulting structural model (e.g., crystal packing artifacts, precision and accuracy, plasticity). Second, picosecond to nanosecond dynamics is a major contribution to the conformational entropy of a protein,[5−7] and hence to the thermodynamics of biochemical processes such as protein folding, ligand binding, allosteric regulation, enzyme catalysis, etc. Moreover, the hydrodynamic properties governing the rotational diffusion are a sensitive probe of the overall shape and size of the solvation shell,[8] of the oligomerization state of the protein,[9,10] and of environmental effects such as subcellular localization.[11,12] Most importantly, conformational dynamics on the picosecond to nanosecond time scale is often required for function. For instance, it has been shown that ligand binding is governed not only by chemical properties of the binding site but also by its dynamics augmenting binding specificity.[13] In enzymes the dynamics of the residues in the active site lead to active site substates, of which usually one is catalytically competent and all others are not, directly affecting the catalytic activity.[14] Protein dynamics is also crucial for posttranslational modifications as has been demonstrated for the phosphorylation of the cystic fibrosis transmembrane conductance regulator (CFTR) region.[15] CFTR is an intrinsically disordered protein interacting with different partners for regulatory processes, which is facilitated by fast, phosphorylation-dependent dynamics for rapid exchange between different protein states. For the autophagy-related protein GATE-16 it was revealed that its C-terminus is highly flexible, which can lead to a state where the C-terminus is solvent-exposed facilitating lipidation, which in turn is important for autophagy.[16] Another example for the necessity of fast protein dynamics is given by the process of proteolysis, where proteases catalyze the hydrolysis of peptide bonds within different protein substrates. While this cleavage takes place at a specific site within the substrate, the substrates do not usually share any recognizable consensus motif. However, there is indication that the conformational dynamics of the substrate might contribute to substrate recognition and thus to cleavage specificity.[17]

1.2. Conformational Dynamics Sensed by Depolarization.

The temporal behavior of these local motions is sensed by molecular probes such as nuclear spins in NMR spectroscopy, transition dipoles of chromophores in fluorescence spectroscopy, or the orientation of bonds as monitored in molecular dynamics (MD) simulations (Figure 1C). The loss of orientation of these probes can be monitored by the depolarization of spins and transition dipoles and is quantified by order parameters and depolarization times. In fluorescence spectroscopy, the rotational motion of the chromophore label is superimposed upon that of the entire protein it is attached to.[18] Different types of internal rotations of the label are possible and include rotation of the chromophore about the bond linking it to the protein, rotational wobble resulting from local motions of the protein in proximity to the label, and rotations of molecular domains within the label if it contains rotatable bonds.[19] In practice, a superposition of these rotations and overall protein rotation is usually present, causing the reorientation of the transition dipole moments of the chromophore, which is directly reflected in a multiexponential decay of the fluorescence anisotropy.

In NMR spectroscopy, the reorientation of two dipolar coupled spins is caused by internal motions and overall rotational diffusion that result in stochastic fluctuations of the local magnetic field (Figure 1C). This leads to relaxation of the spins to thermal equilibrium parallel (longitudinal relaxation) and perpendicular (transverse relaxation) to the direction of the externally applied magnetic field. The relaxation rates are described by R_1 and R_2 for longitudinal and transverse relaxation, respectively. These relaxation rates are different for each spin and indicate the internal motion on the picosecond to nanosecond time scale. The relaxation rates are determined by a series of NMR experiments at different strengths of the external magnetic field and for distinct time intervals as the peak intensity depends exponentially on the time interval and R_1. First, R_1 and $R_{1\rho}$, which is the longitudinal relaxation in a rotating frame, are determined. Thereafter, the transverse relaxation rate R_2 can be obtained. Additional information on the dynamics of the N−H bond vector is retrieved by $\{^1H\}$-^{15}N heteronuclear NOE[20] experiments. Flexible regions in the protein structure are reflected in bond vector dynamics, which leads to low NOE values compared to the case of rigid residues.

While NMR and fluorescence spectroscopy are the most widely used methods to characterize protein dynamics experimentally, MD simulations are the only method capturing protein dynamics directly at atomic resolution[21] and can thus be considered as a "computational microscope".[22] Nowadays, MD simulations can reach microseconds and even milliseconds[23] and the resulting trajectories can be viewed like videos of atomic and molecular motion. More importantly, statistical properties of the conformational ensemble, such as quantities characterizing the structure of the protein, time-dependent averages of spectroscopically observable quantities, or probabilities for the transitions between certain conformations can be calculated from the trajectories. For many experimental methods including fluorescence and NMR spectroscopy, the underlying theories permit the computation of experimental observables directly from the positions and movements of the protein atoms.[20,24,25] MD simulations can therefore be validated against experimental data, assessing if they sample all relevant protein conformations with the correct probabilities. However, even more important is that MD simulations provide direct evidence of the structures and the molecular processes giving rise to the signals measured in experiments. In the context of the current work, it is of significance that one can directly follow the reorientation of bonds of the protein, which can result from local motions as well as overall rotation. The depolarization of the bond vector orientations can thus directly be calculated from the MD trajectories and compared to the corresponding quantities probed by fluorescence and NMR spectroscopy.

1.3. Integrated Approaches to Studying Protein Dynamics. In practice, the three techniques, i.e., NMR, fluorescence, and MD differ markedly in terms of requirements (sample concentration, sample labeling, buffer, and/or cellular environment, etc.) as well as information content (sensitivity, temporal, and spatial resolution, etc.). A comprehensive understanding of the conformational dynamics of a protein at atomic resolution and covering all relevant time scales and environmental conditions can therefore only be expected from an integrated approach combining these three complementary techniques in a common, experimentally validated, analytical framework. Numerous studies exist that combined any two of the three techniques. For instance, fluorescence spectroscopy and MD simulations have been jointly applied to various problems, which is also based on the fact that the analysis of fluorescence anisotropy decay is a tool to elucidate internal motion and diffusion of biomolecules and is a topic of broad theoretical consideration.[26−30] MD can be used to validate the fluorescence anisotropy for studying the flexibility of proteins,[25,31] but these approaches suffered from lack of adequate fluorescence analysis,[32] suboptimal dye selection, and relying on not validated dye force fields. More often, when MD is combined with fluorescence, it is used either to explain the molecular basis of a fluorescence observable[25,33−35] or to validate the parametrization of dye models[36,37] for further modeling of FRET-based structures.[38−40] Further information and examples for the combination of fluorescence spectroscopy and MD can be found in a review by Stella et al.,[41] which highlights the complementarity of both techniques and the resulting potential for their synergistic application. The combination of NMR and fluorescence spectroscopy was applied to small organic molecules to estimate precise absolute diffusion coefficients[42,43] where the fluorescence was used to estimate the effects of protein concentration. In another study, NMR was used to characterize molecular interactions found by fluorescence techniques.[44] The fast dynamics of a small peptide was measured by combining NMR spectroscopy and intrinsic fluorescence anisotropy, yielding information on the local dynamics of the peptide chain and side chains.[45] Probably the most often applied combination of the three techniques under consideration is the synergistic application of NMR spectroscopy and MD simulations to study protein dynamics. NMR and MD can be combined in many different ways as both methods provide information on the atomistic level and probe the protein dynamics on similar time scales (Figure 1). The popularity of the combination of NMR and MD is also reflected by the fact that several reviews have already been published on this topic.[46−48] In many joint applications of NMR and MD, static NMR parameters (i.e., chemical shielding and J couplings) were determined and MD simulations used as tool for the analysis of the NMR data in terms of structural properties of the proteins. Here, we focus on the connection of protein dynamics as observed from MD simulations with that derived from NMR spectral quantities. Using MD simulations to interpret structural and dynamical NMR data, Ángyán and Gáspári demonstrated the importance of treating the NMR observables and parameters derived from them as structural ensembles over relevant time scales rather than individual protein conformers.[49] Important contributions to the combination of MD and NMR were made by Brüschweiler et al. They developed a general framework for the interpretation of NMR relaxation data of proteins based on MD simulations.[50,51] Calligari and Abergel demonstrated that also chemical shifts can be used to study protein dynamics using the fluctuations in ^{15}N chemical shifts measured in experiments combined with chemical shift time correlation functions calculated from MD simulations to identify the underlying motions.[52] Palmer et al. studied the partially disordered yeast transcription factor GCN4 by combining spin-relaxation and back-calculated chemical shifts, which provide information about residual secondary structure, and MD simulations providing the order parameters, which yielded detailed insight into secondary structure elements and their dynamics.[53] These few examples already demonstrate the power of combining MD and NMR for studying protein conformational dynamics and for further applications the reader is referred to the review by Mocci and Laaksonen.[48] In a recent review by Palmer the application of NMR spin relaxation experiments to study the dynamics of enzymes is surveyed, which includes examples of the combination both with MD simulations and with fluorescence spectroscopy.[54]

DOI: 10.1021/acs.jpcb.8b08903
J. Phys. Chem. B 2019, 123, 1453−1480

To the best of our knowledge, no work has been published yet where all three techniques are jointly applied to study protein dynamics. To overcome this gap, we here develop an integrated approach using ^{15}N NMR spin relaxation, fluorescence techniques based on time-resolved anisotropy and fluorescence correlation spectroscopy (FCS), and MD simulations to characterize protein dynamics. Our approach is based on the seminal work by Lipari and Szabo, who in 1980 developed the theory to demonstrate the connection between fluorescence depolarization and NMR relaxation in biomacromolecules.[55] They showed that the limiting fluorescence emission anisotropy is proportional to the square of the order parameter of the probe, which is a measure of the spatial restriction that the probe experiences in a molecular reference frame. In 1982 they published the model-free approach to the interpretation of NMR relaxation, which has become the standard method for the calculation of order parameters and forms the basis of the current work.[56] We apply our integrated NMR/fluorescence/MD approach to study the most fundamental level of protein dynamics, that is, the picosecond to nanosecond dynamics and hydrodynamics using the autophagy-related protein GABARAP in its soluble form as a prototype for a folded but flexible protein. First, we present the common theoretical framework before applying it to GABARP, followed by a thorough interpretation of the results as well as providing a cross-validation of the three techniques. Intriguingly, the quantification of the picosecond to nanosecond conformational dynamics already reveals several implications for self-association of GABARAP and its internal mechanics on slower time scales. Our work presented here lays the foundation for studying the dynamics of GABARAP in more complex environments and on longer time scales in order to elucidate its contribution to the autophagic machinery in cells at a submolecular level.

2. EXPERIMENTAL QUANTIFICATION AND THEORETICAL CONCEPTS

NMR and fluorescence spectroscopy are the most widely used methods providing experimental insight into dynamics on virtually all relevant time scales from picoseconds to days.[1,57,58] It has long been recognized that the physical mechanisms underlying fluorescence depolarization on the one hand and NMR relaxation on the other hand are closely related to each other.[55] An understanding of how these different experimental methods complement each other is obtained by revisiting the relevant theory with a particular emphasis on the conceptual similarities.

2.1. Time-Resolved Fluorescence Anisotropy. In a nutshell, the anisotropy $r(t+t_c)$ of the fluorescence intensity emitted at time $t + t_c$ after excitation at time t is shown to depend on the orientation of the (electric) transition dipole moment for emission, indicated by the unit vector $\vec{\mu}_e$, according to

$$\begin{aligned} r(t+t_c) &= \frac{F_p(t+t_c) - F_s(t+t_c)}{F_p(t+t_c) + 2F_s(t+t_c)} = \langle (3(\vec{e}_p\cdot\vec{\mu}_e(t+t_c))^2 - 1)/2\rangle \\ &= \langle P_2(\vec{e}_p\cdot\vec{\mu}_e(t+t_c))\rangle \end{aligned} \tag{1}$$

where F_p and F_s are the emission intensities with polarization parallel (p) and perpendicular (s), respectively, to the polarization of the excitation beam indicated by the unit vector $\vec{e}_p$, $P_2(x) = (3x^2 - 1)/2$ is the second Legendre polynomial, and the angular brackets denote ensemble averaging.[28] Taking into account that the excitation of each molecule depends on the orientation of the (electric) transition dipole moment for absorption, indicated by the unit vector $\vec{\mu}_a$, at time t with respect to the polarization of the incident beam, and making use of the addition theorem for second-order spherical harmonics, eq 1 can be recast into

$$r(t+t_c) = \frac{2}{5}\langle P_2(\vec{\mu}_a(t)\cdot\vec{\mu}_e(t+t_c))\rangle \tag{2}$$

which now depends only on the relative orientation of the transition dipole moments for absorption and emission at two different time points.[28] Again making use of the addition theorem for second-order spherical harmonics, this relative orientation can be further separated into the relative orientation of the transition dipole moments of the chromophore itself and the reorientation of the chromophore between absorption and emission,

$$\begin{aligned} r(t+t_c) &= \frac{2}{5}P_2(\cos\delta)\langle P_2(\vec{\mu}_e(t)\cdot\vec{\mu}_e(t+t_c))\rangle \\ &= r_0\langle P_2(\vec{\mu}_e(t)\cdot\vec{\mu}_e(t+t_c))\rangle = r_0 C(t_c) \end{aligned} \tag{3}$$

where δ denotes the angle between the transition dipole moments for absorption and emission of the chromophore.[28,55] In this expression, $r(t_c{=}0) = r_0 = 0.4\cdot P_2(\cos\delta)$ is a constant for a given chromophore and the decay of the fluorescence anisotropy is therefore determined by the loss of autocorrelation of the second Legendre polynomial of the orientation of the chromophore,

$$C(t_c) = \langle P_2(\vec{\mu}_e(t)\cdot\vec{\mu}_e(t+t_c))\rangle = \langle (3\cos^2\theta(t+t_c) - 1)/2\rangle \tag{4}$$

where θ is the angle of the chromophore at time $t + t_c$ with respect to its orientation at time t.

2.2. NMR Spin Relaxation. A nuclear spin, $\vec{I}$, is associated with a magnetic moment of $\vec{\mu}_I = \gamma_I\vec{I}$, where γ_I is called the gyromagnetic ratio of spin $\vec{I}$. The vector sum of all the magnetic moments in a thermodynamic ensemble of nuclear spins gives rise to a net macroscopic magnetization, $\vec{M}$, which can be parallel (longitudinal) or perpendicular (transverse) to the static external magnetic field $\vec{B}_0$. Longitudinal magnetization is caused by differential population of the different spin eigenstates (spin-up or spin-down for nuclei with spin quantum number $I = {}^1/_2$, such as ^{1}H, ^{13}C, ^{15}N); in thermal equilibrium, the population difference described by the Boltzmann distribution results in a finite longitudinal magnetization. By contrast, transverse magnetization does not correspond to any spin eigenstates but is caused by phase coherence of the ensemble of spins; in thermal equilibrium, the phase coherence and hence the transverse magnetization is zero. NMR spin relaxation, the (exponential) process of the magnetization returning to its thermal equilibrium following a perturbation, is mediated by anisotropic local magnetic fields. In practice, NMR relaxation of a particular spin $\vec{I}$ of interest is usually dominated by the magnetic dipole−dipole (DD) coupling to a spin that is close in space, e.g., to the directly bonded amide ^{1}H in the case of backbone amide ^{15}N spin relaxation. The magnetic dipole moment associated with the neighboring spin $\vec{S}$, $\vec{\mu}_S = \gamma_S\vec{S}$, generates a magnetic dipole field, whose interaction with $\vec{\mu}_I = \gamma_I\vec{I}$ is described by the usual magnetic dipole−dipole coupling Hamiltonian:

$$H_{DD} = -\frac{\mu_0}{4\pi}\frac{\gamma_I\gamma_S}{r_{IS}^{\;3}}(3(\vec{I}\cdot\vec{\mu}_{IS})(\vec{S}\cdot\vec{\mu}_{IS}) - \vec{I}\cdot\vec{S}) = \vec{I}^{\,T}\cdot\bar{\bar{D}}_{IS}\cdot\vec{S} \tag{5}$$

where μ_0 is the permeability of the vacuum, γ_S is the gyromagnetic ratio of spin $\vec{S}$, r_{IS} is the distance, and $\vec{\mu}_{IS}$ the direction of the internuclear vector connecting $\vec{I}$ and $\vec{S}$. The symmetric second-rank tensor describing this interaction,

$$\overline{\overline{D}}_{IS} = -\frac{\mu_0}{4\pi}\frac{\gamma_I\gamma_S}{r_{IS}^{3}}(3\vec{\mu}_{IS}\vec{\mu}_{IS} - \overline{\overline{1}}) \tag{6}$$

is traceless because the dipole−dipole coupling is fully anisotropic without any isotropic component. To first-order perturbation theory (the so-called secular approximation), the longitudinal magnetic dipole field component generated by the longitudinal component of $\vec{S}$,

$$\begin{aligned} B_{\mathrm{DD}}(t{+}t_{\mathrm{c}}) &= \frac{\mu_0}{4\pi}\frac{\gamma_S}{r_{IS}^{3}(t{+}t_{\mathrm{c}})}2P_2(\vec{e}_z\cdot\vec{\mu}_{\mathrm{IS}}(t{+}t_{\mathrm{c}}))S_z \\ &= \frac{\mu_0}{4\pi}\frac{\gamma_S}{r_{IS}^{3}(t{+}t_{\mathrm{c}})}(3\cos^2\beta(t{+}t_{\mathrm{c}}) - 1)S_z \end{aligned} \tag{7}$$

where $\vec{e}_z$ is the direction of the static external magnetic field $\vec{B}_0 = B_0\vec{e}_z$, β is the angle of the internuclear vector $\vec{\mu}_{IS}$ with respect to $\vec{B}_0$, and S_z is the component of $\vec{S}$ in the direction of $\vec{B}_0$, adds to the external magnetic field and modulates the (instantaneous) resonance frequency of $\vec{I}$ to $\omega_I = -\gamma_I(B_0{+}B_{\mathrm{DD}})$.[55]

The distance r_{IS} (e.g., the ^{1}H−^{15}N bond length) usually varies little. By contrast, the direction of the internuclear vector, $\vec{\mu}_{IS}$, and hence of the dipolar coupling tensor, $\overline{\overline{D}}_{IS}$, depends on the orientation of the molecule, while the orientation of the spins $\vec{I}$ and $\vec{S}$ is determined by the direction of the external magnetic field $\vec{B}_0$ irrespective of molecular orientation. As shown in Figure 1C, this means that any reorientation of the spin pair gives rise to a fluctuating magnetic field, and eq 7 reveals that the dependence of the dipole field on the orientation relative to the laboratory frame follows a mathematical form similar to that of the fluorescence anisotropy (eq 1), as expected from the close analogy between (electric) transition dipole moments and (magnetic) nuclear dipole moments. Accordingly, it can be shown that the fluctuation of the magnetic dipole−dipole interaction (or other axially symmetric second-rank tensorial interaction including chemical shift anisotropy (CSA)) is described by the same autocorrelation function as above:

$$C(t_{\mathrm{c}}) = \langle P_2(\vec{\mu}_{\mathrm{IS}}(t)\cdot\vec{\mu}_{\mathrm{IS}}(t{+}t_{\mathrm{c}}))\rangle = \langle(3\cos^2\theta(t{+}t_{\mathrm{c}}) - 1)/2\rangle \tag{8}$$

where θ is the angle of $\vec{\mu}_{IS}$ at time $t + t_{\mathrm{c}}$ with respect to its orientation at time t.[55,56]

2.3. Autocorrelation Function for Rotational Diffusion.

The orientation θ is modulated by both overall rotational diffusion and internal motions, which are assumed to be independent of each other so that the autocorrelation function can be separated into the autocorrelation function for the overall rotational diffusion, C_{global}, and the autocorrelation function for the internal motions, C_{int}:

$$C(t_{\mathrm{c}}) = C_{\mathrm{int}}(t_{\mathrm{c}})\, C_{\mathrm{global}}(t_{\mathrm{c}}) \tag{9}$$

Thus, in order to evaluate the ensemble average in autocorrelation functions (4) and (8), we have to solve the rotational diffusion equation first. Autocorrelation functions of diffusive (more generally, Markovian stochastic) motions can be expressed as a sum of exponentials. In the case of isotropic rotational diffusion, the conditional probability density $p(\vec{\mu}_0(t)|\vec{\mu}(t{+}t_{\mathrm{c}}))$ of finding the molecule in orientation $\vec{\mu}(t\,{+}t_{\mathrm{c}})$ at time $t + t_{\mathrm{c}}$ after finding it in orientation $\vec{\mu}_0(t)$ at time t follows the diffusion equation

$$\frac{\partial}{\partial t_{\mathrm{c}}}p(\vec{\mu}_0(t)|\vec{\mu}(t{+}t_{\mathrm{c}})) = -D_{\mathrm{rot}}L^2 p(\vec{\mu}_0(t)|\vec{\mu}(t{+}t_{\mathrm{c}})) \tag{10}$$

where D_{rot} is the rotational diffusion coefficient and $\vec{L}$ is the angular momentum operator divided by the Planck constant $\hbar = h/(2\pi)$.[59−61] Because the spherical harmonics $Y_{lm}(\vec{\mu})$ are a complete set of orthonormal eigenfunctions of the angular momentum operator with

$$L^2 Y_{lm}(\vec{\mu}) = l(l+1)\, Y_{lm}(\vec{\mu}) \tag{11}$$

where $l = 0, 1, 2, ...$ is the angular momentum quantum number and $m = -l, -l + 1, ..., 0, ..., l - 1, l$ the magnetic quantum number,[62] the solution of eq 10 can be expressed[59−61] as

$$p(\vec{\mu}_0(t)|\vec{\mu}(t{+}t_{\mathrm{c}})) = \sum_{l=0}^{\infty}\sum_{m=-l}^{l} g_{lm}Y_{lm}(\vec{\mu}(t{+}t_{\mathrm{c}}))\mathrm{e}^{-l(l+1)D_{\mathrm{rot}}t_{\mathrm{c}}} \tag{12}$$

The coefficients g_{lm} have to satisfy the initial condition that $\vec{\mu}_0(t)$ is the only orientation with nonzero probability density in the limit $t_{\mathrm{c}} = 0$:

$$p(\vec{\mu}_0(t)|\vec{\mu}(t)) = \sum_{l=0}^{\infty}\sum_{m=-l}^{l} g_{lm}Y_{lm}(\vec{\mu}(t)) = \delta(\vec{\mu}(t){-}\vec{\mu}_0(t)) \tag{13}$$

Recalling the closure relation of the spherical harmonics[62]

$$\sum_{l=0}^{\infty}\sum_{m=-l}^{l} Y_{lm}^{*}(\vec{\mu}_0)\, Y_{lm}(\vec{\mu}) = \delta(\vec{\mu}{-}\vec{\mu}_0) \tag{14}$$

it is straightforward to see that the relevant solution of eq 10 is

$$\begin{aligned} p(\vec{\mu}_0(t)|\vec{\mu}(t{+}t_{\mathrm{c}})) = \sum_{l=0}^{\infty}\sum_{m=-l}^{l} & Y_{lm}^{*}(\vec{\mu}_0(t))\, Y_{lm}(\vec{\mu}(t{+}t_{\mathrm{c}})) \\ & \times \mathrm{e}^{-l(l+1)D_{\mathrm{rot}}t_{\mathrm{c}}} \end{aligned} \tag{15}$$

Note that the Legendre polynomials $P_l(\vec{\mu}\cdot\vec{e}_z) = \sqrt{4\pi/(2l+1)}\, Y_{l0}(\vec{\mu})$ are essentially the subset of the spherical harmonics with $m = 0$. Making use of the addition theorem for spherical harmonics[62]

$$P_l(\vec{\mu}_{\mathrm{e}}(t)\cdot\vec{\mu}_{\mathrm{e}}(t{+}t_{\mathrm{c}})) = \frac{4\pi}{2l+1}\sum_{m=-l}^{l} Y_{lm}(\vec{\mu}_{\mathrm{e}}(t))\, Y_{lm}^{*}(\vec{\mu}_{\mathrm{e}}(t{+}t_{\mathrm{c}})) \tag{16}$$

the ensemble average in the autocorrelation function of the second Legendre polynomial (eq 4) is now readily evaluated by integrating over all orientations (solid angles):

$$\begin{aligned} C_{\mathrm{global}}(t_{\mathrm{c}}) &= \langle P_2(\vec{\mu}_{\mathrm{e}}(t)\cdot\vec{\mu}_{\mathrm{e}}(t{+}t_{\mathrm{c}}))\rangle \\ &= \iint P_2(\vec{\mu}_0(t)\cdot\vec{\mu}(t{+}t_{\mathrm{c}}))\, p(\vec{\mu}_0(t)) \\ &\quad \times p(\vec{\mu}_0(t)|\vec{\mu}(t{+}t_{\mathrm{c}}))\, \mathrm{d}^2\vec{\mu}_0\, \mathrm{d}^2\vec{\mu} \end{aligned} \tag{17}$$

In an isotropic sample the probability density of finding the molecule in orientation $\vec{\mu}_{\mathrm{e}}(t)$ at time t is $p(\vec{\mu}_0(t)) = 1/(4\pi)$ for all orientations on the unit sphere. It is obvious from the addition theorem (eq 14) that rotations preserve the order l of the spherical harmonics and it is therefore clear from the orthonormality of the spherical harmonics that only the term with $l = 2$ in the sum of exponentials in eq 15 contributes to the autocorrelation function of the second ($l = 2$) Legendre polynomial. Thus, we finally obtain the monoexponential autocorrelation function

$$\begin{aligned} C_{\text{global}}(t_c) &= \iint \frac{4\pi}{5} \sum_{m=-2}^{2} Y_{2m}(\vec{\mu}_0)\, Y^*_{2m}(\vec{\mu}) \\ &\quad \times \frac{1}{4\pi} \sum_{l=0}^{\infty} \sum_{m'=-l}^{l} Y^*_{lm'}(\vec{\mu}_0)\, Y_{lm'}(\vec{\mu}) \mathrm{e}^{-l(l+1)D_{\text{rot}}t_c}\, \mathrm{d}^2\vec{\mu}_0\, \mathrm{d}^2\vec{\mu} \\ &= \frac{1}{5} \sum_{m=-2}^{2} \sum_{l=0}^{\infty} \sum_{m'=-1}^{1} \delta_{21}\delta_{mm'}\delta_{21}\delta_{mm'} \mathrm{e}^{-l(l+1)D_{\text{rot}}t_c} \\ &= \frac{1}{5} \sum_{m=-2}^{2} \mathrm{e}^{-6D_{\text{rot}}t_c} = \mathrm{e}^{-6D_{\text{rot}}t_c} = \mathrm{e}^{-t_c/\rho_{\text{global}}} \end{aligned} \tag{18}$$

with the global rotational autocorrelation time $\rho_{\text{global}} = 1/(6D_{\text{rot}})$. If the overall rotational diffusion is not sufficiently isotropic, the rotational diffusion coefficient D_{rot} is described by a symmetric tensor and in this case the global autocorrelation function $C_{\text{global}}(t_c)$ must itself be described by a weighted sum of three (axially symmetric tensor) or five (fully asymmetric tensor) different exponentials with weighting factors that depend on the orientation of the chromophore or spin pair relative to the rotational diffusion tensor,[60,63] which can be determined if the high-resolution structure of the protein is available.

If there are internal motions on the same time scale as the global rotational diffusion ρ_{global} or faster, the second Legendre polynomial autocorrelation function will decay more rapidly than in rigid areas of the molecule, which can be described by multiexponential autocorrelation functions such as

$$\begin{aligned} C(t_c) &= C_{\text{int}}(t_c)\, C_{\text{global}}(t_c) = C_{\text{int}}(t_c)\mathrm{e}^{-t_c/\rho_{\text{global}}} \\ &= [(S_{\text{init}}{}^2 - S_{\text{fast}}{}^2)\mathrm{e}^{-t_c/\rho_{\text{fast}}} + (S_{\text{fast}}{}^2 - S^2)\mathrm{e}^{-t_c/\rho_{\text{slow}}} \\ &\quad + S^2]\mathrm{e}^{-t_c/\rho_{\text{global}}} \end{aligned} \tag{19}$$

where the autocorrelation times ρ_{fast}, ρ_{slow} are the time scales of two internal motions of a given chromophore or spin pair orientation vector and the order parameters S_{fast}, S describe the motional restriction of these two internal motions on a scale of 0 to 1.[56,64] The initial order parameter S_{init} can be used to account for any loss in autocorrelation by motions that are too fast to be resolved experimentally or captured in the MD trajectories in case that the conformations sampled during a simulation are not saved with femto- but nanosecond resolution as commonly done, otherwise $S_{\text{init}} = 1$.

2.4. Hydrodynamic Radius. If the molecule is approximately spherical in shape, the rotational diffusion is isotropic and described by a single rotational diffusion constant D_{rot} and, hence, by a single global rotational autocorrelation time ρ_{global}, which are determined by the hydrodynamic radius of the molecule, $R_{\text{h,rot}}$, according to the Stokes–Einstein–Debye relation for rotational diffusion:

$$D_{\text{rot}} = \frac{k_B T}{8\pi\eta R_{h,\text{rot}}{}^3} = \frac{1}{6\rho_{\text{global}}} \tag{20}$$

Comparison with the Stokes–Einstein relation for translational diffusion,

$$D_{\text{trans}} = \frac{k_B T}{6\pi\eta R_{\text{h,trans}}} \tag{21}$$

reveals that rotational diffusion is obviously an even more sensitive probe of molecular size than translational diffusion. For a spherical molecule $R_{\text{h,rot}}$ and $R_{\text{h,trans}}$ are identical. If the particle deviates from spherical geometry, the hydrodynamic friction increases compared to the equivalent sphere of equal volume, R_{eq}, by factors of $R_{\text{h,rot}}{}^3 = F_{\text{rot}} \times R_{\text{eq}}{}^3$ and $R_{\text{h,trans}} = F_{\text{trans}} \times R_{\text{eq}}$, where F_{rot} and F_{trans} are the Perrin shape factors for rotational and translational diffusion, respectively.[2]

2.5. NMR Observables Probing Pico- to Nanosecond Dynamics. Internal motions as well as overall rotational diffusion are directly reflected in a multiexponential decay of the fluorescence anisotropy according to eqs 3 and 19. In NMR spectroscopy, they cause stochastic fluctuations of local magnetic fields, as described in section 2.2 above. These fluctuations have two effects: (i) The longitudinal component, B_{DD}, modulates the (instantaneous) resonance frequency of each spin. In isotropic solution, this does not affect the positions (frequencies) of the resonances in the NMR spectrum because the rotational diffusion of each molecule on the nanosecond time scale quickly averages the secular (first-order perturbation theory) component of the dipole–dipole interaction in eq 5 and of the CSA to zero.[65] However, in second order these stochastic fluctuations in (instantaneous) resonance frequency result in a loss of phase coherence of the thermodynamic ensemble of spins and hence a loss of transverse magnetization, i.e., give rise to transverse relaxation. (ii) Moreover, in second-order perturbation theory, the transverse components of the fluctuating magnetic dipole fields (Figure 1C) act like electromagnetic radiation that stimulates transitions between the spin states. In turn, this leads to a redistribution of longitudinal magnetization (longitudinal relaxation), loss of phase coherence (transverse relaxation), and longitudinal cross-relaxation effects between two coupled spins such as the nuclear Overhauser effect (NOE), which are all reflected in the intensities and line widths of the NMR resonances. It can be shown that the fluctuations of the transverse components are described by the same autocorrelation function as the longitudinal component (eq 8).[66] The spectral density of the stochastic fluctuations is obtained by Fourier analysis of the autocorrelation function[55,56]

$$J(\omega) = \frac{2}{5} \int_0^{\infty} C(t_c) \cos(\omega t_c)\, \mathrm{d}t_c \tag{22}$$

which is a sum of Lorentzians in the case of the multiexponential extended Lipari–Szabo-type autocorrelation function $C(t_c)$ given by eq 19:

$$\begin{aligned} J(\omega) = \frac{2}{5} \sum_{i=-k}^{k} c_i \times \rho_i \Bigg(& \frac{S^2}{1 + (\omega\rho_i)^2} \\ & + \frac{(1 - S_{\text{fast}}{}^2)(\rho_{\text{fast}} + \rho_i)\rho_{\text{fast}}}{(\rho_{\text{fast}} + \rho_i)^2 + (\omega\rho_{\text{fast}}\rho_i)^2} \\ & + \frac{(S_{\text{fast}}{}^2 - S^2)(\rho_{\text{slow}} + \rho_i)\rho_{\text{slow}}}{(\rho_{\text{slow}} + \rho_i)^2 + (\omega\rho_{\text{slow}}\rho_i)^2} \Bigg) \end{aligned} \tag{23}$$

where $2k + 1$ is the number of autocorrelation times ρ_i that describe the rotational diffusion process (one in the isotropic case, three in the axially symmetric case, and five in the fully asymmetric case) and c_i are weighting factors that depend on the orientation of the internuclear vector relative to the rotational diffusion tensor.[64,67] In second order, it is clear that only the spectral density components $J(\omega)$ at the frequencies $\omega = 0$ (secular dephasing, transverse relaxation only), $\omega = \omega_I$ (I spin

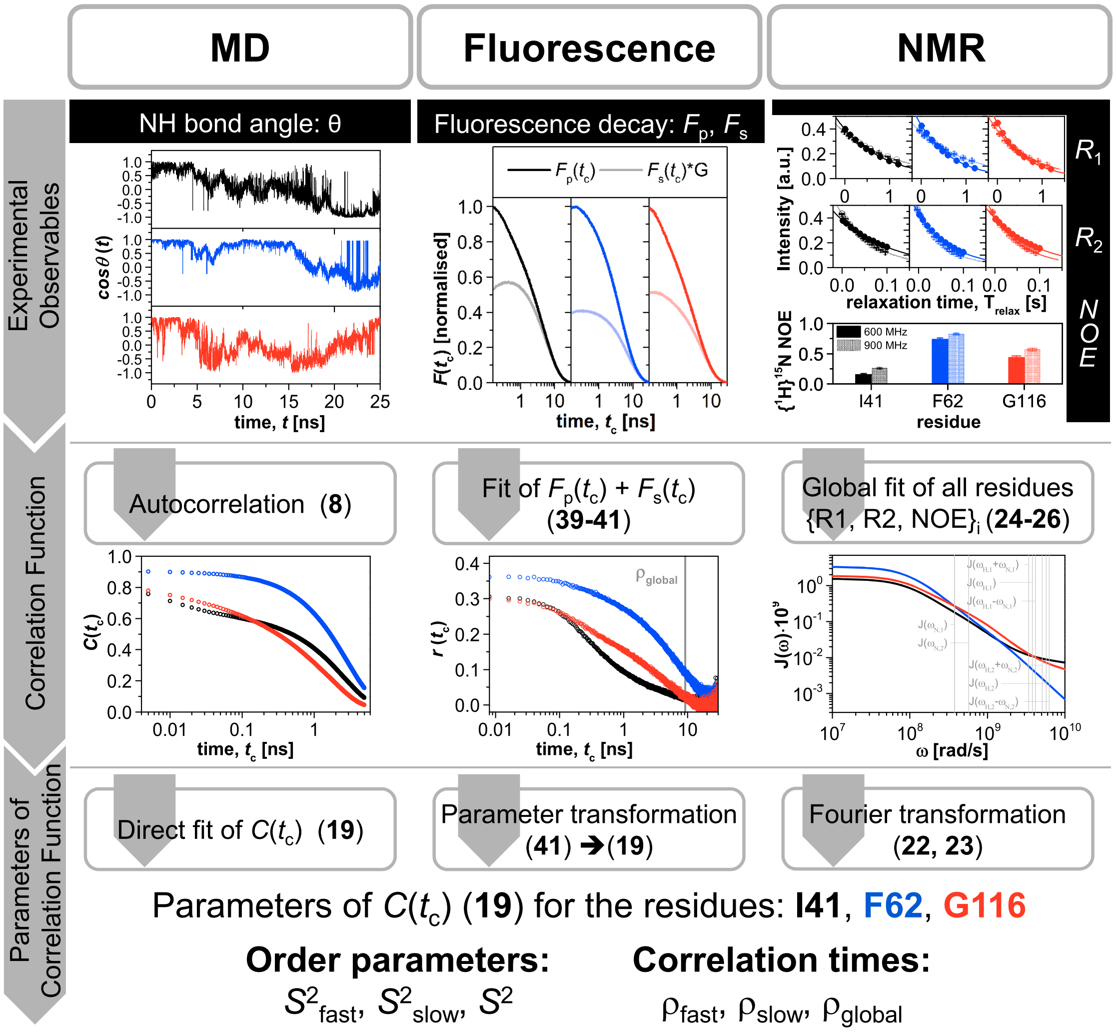

Figure 2. Workflow of the integrated analysis. Our integrated approach combines MD simulations, spectroscopic techniques based on fluorescence anisotropy and fluorescence correlation, and NMR spectroscopy. The used equations are printed in bold. The left and middle columns show for MD simulations and fluorescence spectroscopy the raw data that are monitored using these two techniques, respectively. As illustrative examples we show data for residues I41 (high flexibility, black), F62 (low flexibility, blue), and G116 (high flexibility, red), which are also discussed in detail in this paper. The raw data are processed to obtain the autocorrelation function, $C(t_c)$ for the decay of the N−H bond vector orientation as measured by the cosine of the angle $\theta(t_c)$, and the fluorescence anisotropy, $r(t_c)$, respectively (middle row). In the case of NMR spectroscopy, the raw data are given by the spectral densities measured at two different external magnetic fields with Lamor frequencies of 600 and 900 MHz, as indicated by the gray vertical lines in the top panel of the right column. From these, the spectral densities $J(\omega)$ are back-calculated via an iterative fitting procedure determining R_1, R_2, and heteronuclear NOEs (right top panel). From $J(\omega)$, $r(t_c)$, and $C(t_c)$ the order parameters and time scales for internal and global motion can then be determined via fitting of the corresponding equations.

flip), $\omega = \omega_S$ (S spin flip), $\omega = \omega_I - \omega_S$ (flip-flop transition), and $\omega = \omega_I + \omega_S$ (flip−flip transition) fulfill the necessary resonance conditions to stimulate transitions between different spin states, where ω_I and ω_S are the Larmor frequencies of spin I and spin S, respectively. Detailed calculation reveals that the longitudinal relaxation rate, R_1, transverse relaxation rate, R_2, and heteronuclear NOE of a protein backbone amide ^{15}N nucleus are given by the following linear combinations of these spectral density components:[66]

$$R_1 = \frac{1}{T_1} = d[J(\omega_H - \omega_N) + 3J(\omega_N) + 6J(\omega_H + \omega_N)] + cJ(\omega_N) \tag{24}$$

$$R_2 = \frac{1}{T_2} = \frac{d}{2}[4J(0) + J(\omega_H - \omega_N) + 3J(\omega_N) + 6J(\omega_H + \omega_N) + 6J(\omega_H)] + \frac{c}{6}[4J(0) + 3J(\omega_N)] + R_{ex} \tag{25}$$

$$\mathrm{NOE} = 1 + \left[d\frac{\gamma_H}{\gamma_N}\frac{6J(\omega_H + \omega_N) - J(\omega_H - \omega_N)}{R_1} \right] \tag{26}$$

Here, the dipolar coupling constant is defined as $d = \frac{1}{4}\left(\frac{\mu_0}{4\pi}\right)^2 \frac{(\gamma_H \gamma_N \hbar)^2}{\langle r_{NH}^6 \rangle}$, where γ_H and γ_N are the gyromagnetic ratios of the ^{1}H and ^{15}N spins and r_{NH} is the bond length. The constant $c = (\omega_N \Delta\sigma_N)^2/3$ depends on the chemical shift anisotropy $\Delta\sigma_N$ measured in ppm. R_{ex} is the contribution to transverse relaxation from chemical exchange on the micro- to millisecond time scale.

Thus, even though NMR spin relaxation is a relatively inefficient second-order process and the rates R_1 and R_2 are therefore on a much slower time scale (millisecond to seconds), they are determined by the spectral density at the distinct frequencies 0, ω_H, ω_N, $\omega_H + \omega_N$, and $\omega_H - \omega_N$ (Figure S1), which are on the order of several hundred megahertz on commercially available NMR spectrometers and hence report on the motional parameters (autocorrelation times, generalized order parameters) describing the nanosecond dynamics of the protein. As shown in Figure 2, the longitudinal relaxation rate, R_1, is obtained by monoexponential fitting of the return of longitudinal magnetization (measured as spectral intensities, I_z) to its equilibrium value (spectral intensity I_0) after inversion ("inversion recovery"),

$$\Delta I_z(T_{\mathrm{relax}}) = I_z(T_{\mathrm{relax}}) - I_0 = \Delta I_z(0)\mathrm{e}^{-R_1 T_{\mathrm{relax}}} \tag{27}$$

where T_{relax} is the recovery delay. Similarly, the transverse relaxation rate, R_2, can be obtained by monoexponential fitting of the decay of transverse magnetization (measured as spectral intensities, I_x) to its equilibrium value of zero when the chemical shift evolution is refocused with a Carr–Purcell–Meiboom–Gill (CPMG) pulse train,

$$I_x(T_{\mathrm{relax}}) = I_x(0)\mathrm{e}^{-R_2 T_{\mathrm{relax}}} \tag{28}$$

where T_{relax} is the length of the CPMG sequence. For technical reasons, it is often more convenient to determine the rotating frame relaxation rate, $R_{1\rho}$, by monoexponential fitting of the decay of (mostly transverse) magnetization aligned along a spin lock pulse (measured as spectral intensities, I_ρ) to its equilibrium value of zero,

$$I_\rho(T_{\mathrm{relax}}) = I_\rho(0)\mathrm{e}^{-R_{1\rho} T_{\mathrm{relax}}} \tag{29}$$

where T_{relax} is the duration of the spin lock (Figure 2). Because $R_{1\rho}$ is a linear combination of R_1 and R_2,[66] R_2 is readily calculated from $R_{1\rho}$ by correcting for the small contribution from R_1. The $\{^1\mathrm{H}\}$-$^{15}\mathrm{N}$ heteronuclear NOE is the ratio of the $^{15}\mathrm{N}$ longitudinal equilibrium magnetization with (spectral intensity I_{sat}) and without (spectral intensity I_0) $^1\mathrm{H}$ saturation, I_{sat}/I_0.[68] As outlined in Figure 2, the motional parameters can then be extracted as adjustable parameters in an iterative global optimization procedure by comparing the spin relaxation rates and NOEs back-calculated from the so-called "model-free" spectral density (eq 23) inserted into eqs 24–26 with the experimentally determined spin relaxation rates and NOEs for all available amide groups at all available magnetic field strengths B_0. This is usually accomplished using software packages such as relax.[69,70]

2.6. Fluorescence Spectroscopy.

Fluorescence Anisotropy. Assigning the anisotropy observables to the triexponential autocorrelation function $C(t_{\mathrm{c}}) = r(t_{\mathrm{c}})/r_0$ (see eq 3) in eq 19 allows one to describe fluorescence anisotropy decays $r(t_{\mathrm{c}})$ by a weighted sum of exponentials:

$$r(t_{\mathrm{c}}) = r_0\left(\frac{r_{\mathrm{fast}}}{r_0}\mathrm{e}^{-t_{\mathrm{c}}/\rho_{\mathrm{fast}}} + \frac{r_{\mathrm{slow}}}{r_0}\mathrm{e}^{-t_{\mathrm{c}}/\rho_{\mathrm{slow}}} + \frac{r_\infty}{r_0}\right)\mathrm{e}^{-t_{\mathrm{c}}/\rho_{\mathrm{global}}} \tag{30}$$

with rotational correlation times ρ_{fast}, ρ_{slow}, and ρ_{global} and the related amplitudes r_{fast}, r_{slow}, and r_∞ with $\Sigma r_i = r_0$, where r_0 is the fundamental anisotropy of the chromophore. Comparison of eq 30 with eq 19 yields the fluorescence order parameter $S^2 = r_\infty/r_0$.

Fluorescence Correlation Spectroscopy. The decay of the anisotropy is not the only fluorescence polarization-dependent technique that is sensitive to the global rotational diffusion of the molecule. Polarization-resolved fluorescence correlation spectroscopy (pFCS), in which fluorescence intensity fluctuations $\delta F_{\mathrm{p/s}}(t_{\mathrm{c}}) = F_{\mathrm{p/s}}(t_{\mathrm{c}}) - \langle F_{\mathrm{p/s}}(t_{\mathrm{c}})\rangle$ under constant excitation are measured, is also able to resolve molecular rotational motion.[59,61,71] It is obvious that two consecutive fluorescence events (absorption followed by emission) of the same chromophore are not independent from each other but correlated. Most importantly, the second absorption process cannot occur immediately after the first absorption process before the molecule has returned to the ground state again, so there is an initial lag phase with an exponential buildup of the photon correlation determined by the excitation rate and the fluorescence lifetime, τ_{e}, and this buildup is referred to as photon antibunching. Accordingly, FCS is primarily sensitive to dynamic processes on the time scale slower than τ_{e}, whereas the decay of the fluorescence intensity on the time scale of τ_{e} limits the sensitivity of anisotropy measurements to processes on this time scale or faster. After the initial buildup, photon correlation is slowly lost to a variety of physical processes as the chromophore begins to populate long-lived nonfluorescent states such as triplet states, reorients due to rotational diffusion, and diffuses translationally out of the active volume of the excitation beam. Under certain conditions the normalized photon correlation function can be factorized into:

$$G(t_{\mathrm{c}}) = 1 + \frac{1}{N}G_a(t_{\mathrm{c}}) \times G_b(t_{\mathrm{c}}) \times G_{\mathrm{rot}}(t_{\mathrm{c}}) \times G_{\mathrm{trans}}(t_{\mathrm{c}}) \tag{31}$$

where $G_a(t_{\mathrm{c}})$ describes the photon antibunching, $G_b(t_{\mathrm{c}})$ is the population of nonfluorescent states, $G_{\mathrm{rot}}(t_{\mathrm{c}})$ is the effect of rotational diffusion, and

$$G_{\mathrm{trans}}(t_{\mathrm{c}}) = (1 + t_{\mathrm{c}}/t_{\mathrm{trans}})^{-1}(1 + (\omega_0/z_0)^2 \times t_{\mathrm{c}}/t_{\mathrm{trans}})^{-1/2}$$

of translational diffusion, where the observation volume is approximated by a 3D-Gaussian volume with $1/e^2$ radii in the lateral (ω_0) and axial direction (z_0), t_{trans} is the diffusion time, and $1/N$ is a scaling factor to account for the effect of the total number N of fluorophore emitters independently diffusing in the observation volume.[59,61]

As noted above, the probability density of absorption depends on the orientation of $\vec{\mu}_{\mathrm{a}}$ relative to the polarization of the incident beam, $\vec{e}_{\mathrm{p}}$, and is proportional to $3(\vec{e}_{\mathrm{p}}\cdot\vec{\mu}_{\mathrm{a}})^2 = 2P_2(\vec{e}_{\mathrm{p}}\cdot\vec{\mu}_{\mathrm{a}}) + P_0(\vec{e}_{\mathrm{p}}\cdot\vec{\mu}_{\mathrm{a}})$, where $P_0 = 1$ and $P_2(x) = (3x^2 - 1)/2$ are the Legendre polynomials of order $l = 0$ and $l = 2$, respectively.[59,61] Similarly, the probability of emitting a photon with polarization $\vec{e}_{\mathrm{e}}$ is proportional to $3(\vec{e}_{\mathrm{e}}\cdot\vec{\mu}_{\mathrm{e}})^2 = 2P_2(\vec{e}_{\mathrm{e}}\cdot\vec{\mu}_{\mathrm{e}}) + P_0(\vec{e}_{\mathrm{e}}\cdot\vec{\mu}_{\mathrm{e}})$. The orientation-dependent rotational factor of the correlation function of two photons with polarizations $\vec{e}_1$ and $\vec{e}_2$ emitted at times t and $t + t_{\mathrm{c}}$, respectively, is hence given by

$$\begin{aligned} C_{\mathrm{rot}}(t_{\mathrm{c}}) = \int_{-\infty}^{t_{\mathrm{c}}} \mathrm{d}t'' \int_{-\infty}^{0} \mathrm{d}t' \, \langle 3(\vec{e}_{\mathrm{p}}\cdot\vec{\mu}_{\mathrm{a}}(t+t'))^2 \times 3(\vec{e}_1\cdot\vec{\mu}_{\mathrm{e}}(t))^2 \\ \times 3(\vec{e}_{\mathrm{p}}\cdot\vec{\mu}_{\mathrm{a}}(t+t''))^2 \times 3(\vec{e}_2\cdot\vec{\mu}_{\mathrm{e}}(t+t_{\mathrm{c}}))^2\rangle \end{aligned} \tag{32}$$

where the integration over the time points of the first $(t + t')$ and second $(t + t'')$ absorption processes accounts for the constant excitation by the incident beam in a typical FCS experiment.[59,61] Although conceptually similar, this expression is clearly more complex than the second Legendre polynomial autocorrelation function (eq 17) above because it depends on four chromophore orientations at four different time points (absorption, emission, absorption, emission) rather than two (absorption, emission). To make the problem more tractable, it is usually assumed that $\tau_{\mathrm{e}} \ll \rho_{\mathrm{global}}$ and the rotational diffusion between absorption and emission is thereby neglected; note that ρ_{global} is typically of the order of several nanoseconds for a small monomeric protein up to hundreds of nanoseconds for a large protein complex, so this

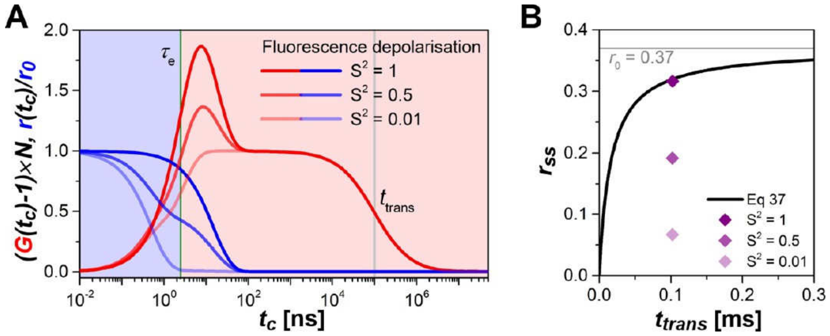

Figure 3. Sensing local flexibility and global motion by combined polarization-resolved fluorescence spectroscopy. (A) Simulations of time-resolved fluorescence anisotropy (blue lines, eq 30) and pFCS signals (red lines, eq 31) assuming protein global rotation ($\rho_{\rm global}$ = 15 ns) combined with a fast internal depolarizing process ($\rho_{\rm int}$ = 0.5 ns). For the internal protein motion, three cases are considered: complete rigidity ($S^2 = 1$), medium rigidity ($S^2 = 0.5$), and high flexibility ($S^2 = 0.01$). This imposes different sensivities to global rotation as the comparison between the three curves for $r(t_c)$ and $(G(t_c) - 1) \times N$ show. (B) Ideal case of a completely rigid fluorophore allowing us to link translational diffusion with rotational observables via the steady-state anisotropy, r_{ss} (eq 37). For $S^2 < 1$, the steady-state anisotropy calculated using eq 37 fails to accurately account for molecular rotation and therefore time-resolved analysis is required. Additional parameters used: $r_0 = 0.37$, $\tau_e = 2.4$ ns, $t_{\rm trans} = 0.1$ ms, $\omega_0 = 0.189$ μm, $R_{\rm h,app} = 24.4$ Å.

assumption is often an approximation for commonly used chromophores with lifetimes τ_e of the order of a few nanoseconds. In this limit, eq 32 simplifies to

$$C_{\rm rot}(t_c) = \langle 3(\vec{e}_p\cdot\vec{\mu}_e(t))^2 \times 3(\vec{e}_1\cdot\vec{\mu}_e(t))^2 \times 3(\vec{e}_p\cdot\vec{\mu}_e(t+t_c))^2 \times 3(\vec{e}_2\cdot\vec{\mu}_e(t+t_c))^2\rangle \qquad (33)$$

where the additional assumption has been made that the transition dipole moments for absorption, $\vec{\mu}_a$, and emission, $\vec{\mu}_e$, are approximately parallel ($\delta \approx 0$).

Using the conditional probability for diffusional reorientation (eq 15) this expression can now be calculated for any particular combination of polarizations $\vec{e}_p$, $\vec{e}_1$, and $\vec{e}_2$ in much the same way as eq 18 above. As we have seen above, the orthonormality of the spherical harmonics guarantees that only the exponential with $l = 2$ contributes to the loss in correlation of two second-order spherical harmonics at times t and $t + t_c$ as a consequence of rotational diffusion. By contrast, eq 32 describes a correlation between a product of two mixed zero-/second-order spherical harmonics of the form $(2P_2(\vec{e}_p\cdot\vec{\mu}_e) + P_0(\vec{e}_p\cdot\vec{\mu}_e)) \times (2P_2(\vec{e}_1\cdot\vec{\mu}_e) + P_0(\vec{e}_1\cdot\vec{\mu}_e))$ at time t with another such product at time $t + t_c$. In the language of quantum mechanics, we are therefore no longer dealing with a single angular momentum wave function of $l = 2$ at each time point but with products of two angular momentum wave functions, and products of two angular momentum wave functions describe the sum of two angular momenta.[62] In the present case these two angular momenta can add up to a total of $l = 0$, $l = 2$, or $l = 4$, and the rotational factor is therefore biexponential:

$$\begin{aligned} C_{\rm rot}(t_c) &= \sum_{l=0,2,4} B_l(\vec{e}_p,\vec{e}_1,\vec{e}_2)\,{\rm e}^{-l(l+1)D_{\rm rot}t_c} \\ &= B_0(\vec{e}_p,\vec{e}_1,\vec{e}_2) + B_2(\vec{e}_p,\vec{e}_1,\vec{e}_2)\,{\rm e}^{-6D_{\rm rot}t_c} \\ &\quad + B_4(\vec{e}_p,\vec{e}_1,\vec{e}_2)\,{\rm e}^{-20D_{\rm rot}t_c} \\ &= B_0(\vec{e}_p,\vec{e}_1,\vec{e}_2) + B_2(\vec{e}_p,\vec{e}_1,\vec{e}_2)\,{\rm e}^{-t_c/\rho_{\rm global}} \\ &\quad + B_4(\vec{e}_p,\vec{e}_1,\vec{e}_2)\,{\rm e}^{-t_c/(0.3\rho_{\rm global})} \end{aligned} \qquad (34)$$

with coefficients $B_l(\vec{e}_p,\vec{e}_1,\vec{e}_2)$ that are related to the Clebsch–Gordan coefficients and have been calculated and tabulated for the most common experimental geometries[59,61] or, after normalization to the equilibrium value $C_{\rm rot}(\infty) = B_0(\vec{e}_p,\vec{e}_1,\vec{e}_2)$,

$$\begin{aligned} G_{\rm rot}(t_c) &= \frac{C_{\rm rot}(t_c)}{B_0(\vec{e}_p,\vec{e}_1,\vec{e}_2)} = 1 + \frac{B_2(\vec{e}_p,\vec{e}_1,\vec{e}_2)}{B_0(\vec{e}_p,\vec{e}_1,\vec{e}_2)}{\rm e}^{-t_c/\rho_{\rm global}} \\ &\quad + \frac{B_4(\vec{e}_p,\vec{e}_1,\vec{e}_2)}{B_0(\vec{e}_p,\vec{e}_1,\vec{e}_2)}{\rm e}^{-t_c/(0.3\rho_{\rm global})} \\ &= 1 + b_{\rm rot}\left(\frac{1}{1+C}{\rm e}^{-t_c/\rho_{\rm global}} + \frac{C}{1+C}{\rm e}^{-t_c/(0.3\rho_{\rm global})}\right) \end{aligned} \qquad (35)$$

where $b_{\rm rot} = (B_2(\vec{e}_p,\vec{e}_1,\vec{e}_2) + B_4(\vec{e}_p,\vec{e}_1,\vec{e}_2))/B_0(\vec{e}_p,\vec{e}_1,\vec{e}_2)$ is the amplitude of the correlation due to rotational diffusion and $C = B_4(\vec{e}_p,\vec{e}_1,\vec{e}_2)/B_2(\vec{e}_p,\vec{e}_1,\vec{e}_2)$. In the case of excitation with a laser beam along $\vec{e}_z$ with polarization $\vec{e}_p = \vec{e}_x$ and cross-correlation of two emitted photons with polarization $\vec{e}_1 = \vec{e}_x = \vec{e}_p$ (parallel) and $\vec{e}_2 = \vec{e}_y = \vec{e}_s$ (perpendicular), e.g., which is the experimental geometry used in the present work, the relevant coefficients are $B_0(\vec{e}_p,\vec{e}_1,\vec{e}_2) = 1323$, $B_2(\vec{e}_p,\vec{e}_1,\vec{e}_2) = 540$, and $B_4(\vec{e}_p,\vec{e}_1,\vec{e}_2) = -280$,[61] and hence $b_{\rm rot} = (540 - 280)/1323 = 0.197$ and $C = -280/540 = -0.519$. In summary, auto- and cross-correlation functions from pFCS measurements are also sensitive to rotational diffusion, albeit in a somewhat more complex mathematical form than the autocorrelation functions probed by fluorescence anisotropy and NMR relaxation spectroscopy, respectively.

2.7. Comparing Fluorescence Correlation and Anisotropy.

While time-resolved fluorescence anisotropy experiments by time-correlated single-photon counting (TCSPC) on the ensemble[18] and single-molecule level[72] are well suited to resolve rotational correlation times similar to or shorter than the excited-state lifetime of the fluorophore, τ_e, polarization-resolved fluorescence correlation spectroscopy (pFCS) is especially useful to map depolarization motions on time scales longer than τ_e (Figure 3A). To gain sufficient contrast in polarization-resolved correlation curves for long correlation times, pFCS requires that the fluorophore be attached rather rigidly to the protein so that its motion is restricted and internal and global protein motions are sensed. To illustrate the effects resulting from internal protein motions combined with global rotation on the time-resolved fluorescence anisotropy and pFCS, three examples of varying flexibility (high, medium, and low S^2 values) are modeled in Figure 3A.

Comparison of the translational diffusion and steady-state anisotropy $r_{ss} = \int_0^\infty F(t_c)\, r(t_c)\, {\rm d}t_c / \int_0^\infty F(t_c)\, {\rm d}t_c$, where $F(t_c)$ is the time-resolved fluorescence intensity decay and $r(t_c)$ is the fluorescence anisotropy decay (eq 30), enables an estimation of the relative contributions of internal and global motions to depolarization. An expression for r_{ss} as a function of the diffusion time is obtained by combining the Perrin equation for a spherical molecule,[18,73,74]

$$\begin{aligned} r_{ss} &= \left(\int_0^\infty F_0 r_0 \mathrm{e}^{(-t_c/\tau_e - t_c/\rho_{global})}\, \mathrm{d}t_c \right) \Big/ \left(\int_0^\infty F_0 \mathrm{e}^{(-t_c/\tau_e)}\, \mathrm{d}t_c \right) \\ &= r_0/(1 + \tau_e/\rho_{global}) \end{aligned} \tag{36}$$

with eqs 20 and 21:

$$r_{ss}(t_{trans}) = r_0 \Big/ \left(1 + \frac{\tau_e 9 {\omega_0}^2}{t_{trans} 8 {R_{h,app}}^2} \right) \tag{37}$$

where a rigid, spherical molecule in the confocal observation volume with a lateral $1/e^2$ radius (ω_0) has been assumed and $R_{h,app} = R_{h,trans} = R_{h,rot}$. Significant internal motions would be indicated by a deviation of $r(t_{trans})$ from eq 37 when plotted using known molecular and experimental parameters. This can be seen in Figure 3B for three different cases of internal flexibility modeled here by a two-component expansion of the Perrin equation:

$$r_{ss} = r_0 \Big/ \left(\frac{1 - S^2}{(1 + \tau_e/\rho_{int})} + \frac{S^2}{(1 + \tau_e/\rho_{global})} \right) \tag{38}$$

2.8. Integrated Approach to Studying the Dynamics of GABARAP. The common theoretical framework for sensing protein motions is the foundation of our current work, where we make use of it by employing NMR and fluorescence spectroscopy together with MD simulations in an integrated approach as summarized in the workflow in Figure 2. We employ this approach to elucidate the picosecond to nanosecond dynamics of the multifunctional autophagy-related protein GABARAP. The 117-residue GABA$_A$ receptor-associated protein (GABARAP) from *Homo sapiens* is a versatile key regulator in autophagy. GABARAP was initially identified as an interaction partner of GABA$_A$ receptors.[75] Further studies revealed that GABARAP interacts with the cytoskeleton through tubulin binding[76] and is implicated in receptor trafficking to the plasma membrane.[77] GABARAP belongs to the ubiquitin-like modifiers and its tertiary structure comprises the C-terminal ubiquitin-like subdomain (ULD) preceded by an N-terminal helical subdomain (NHD) consisting of helices α_1 and α_2, an arrangement that exposes two hydrophobic ligand binding pockets on the molecular surface.[78] It is a cytosolic protein ubiquitously expressed in most tissues and primarily localized to the Golgi apparatus, the endoplasmatic reticulum, and transport vesicles.[79] In addition to its soluble cytosolic forms, GABARAP can also be membrane-anchored via covalent coupling of a phospholipid moiety to G116 by a ubiquitin-like conjugation system.[78] In order for this to occur, the C-terminal residue L117 of GABARAP must first be cleaved off by the ATG4 family of cysteine proteases to yield the 116-residue form GABARAP-I, which can subsequently be conjugated to yield the lipidated form GABARAP-II. Lipidation can also be reversed by the ATG4 family of proteases. In the past decade, a plethora of interaction partners have been identified that reveal the essential role of GABARAP especially in vesicle transport and fusion events in autophagy and apoptosis.[78,80,81] In order to accomplish this multifunctionality as a well-ordered protein with well-defined secondary and tertiary structure elements, it needs to possess high inherent flexibility and cannot be described by a static tertiary structure. In fact, conformational heterogeneity on a wide range of time scales appears to be a hallmark of the GABARAP/MAP1LC3/Atg8 family and is conserved from yeast to mammals.[16,78,82] A detailed understanding of the functional mechanisms on the submolecular level therefore requires a comprehensive analysis of the conformational dynamics of GABARAP on all relevant time scales (from picoseconds to minutes) and in different environments (soluble in the cytosol and anchored to membranes), alone and in interaction with other GABARAP molecules (self-association) and other factors of the autophagic machinery. Here, we characterize the most fundamental level of protein dynamics, the picosecond to nanosecond dynamics and hydrodynamics of soluble GABARAP and GABARAP-I by the integrated NMR, fluorescence, and MD approach outlined in Figure 2.

3. METHODS

3.1. Mutagenesis of the Plasmid Encoding GABARAP. Cysteine variants of GABARAP were obtained using the QuikChange site directed mutagenesis kit according to the protocol provided by Agilent. Primers for the mutagenesis were designed with PrimerX (www.bioinformatics.org/primerx) in order to obtain the following mutations: GABARAP V4C, GABARAP E7C, GABARAP K13C, GABARAP I41C, GABARAP F62C, GABARAP-I G116C.

3.2. Expression, Purification, and Labeling. GABARAP wild-type and cysteine variants were expressed from a pET11a vector in *Escherichia coli* BL21(DE3)-T1^R. Expression and purification was performed according to the protocol reported by Coyle et al.[83] with minor modifications. Briefly, cells were grown at 37 °C in LB (Lysogeny-Broth) medium, or in M9 minimal medium containing $^{15}NH_4Cl$ as the sole nitrogen source for the production of uniformly ^{15}N-enriched ([U-^{15}N]) samples for NMR spectroscopy. Protein expression was induced by 1 mM IPTG (isopropyl β-D-thiogalactopyranoside) at OD_{600} = 0.8−1.0. The expression was carried out at 20 °C for 15 h. Cells were harvested and resuspended in lysis buffer containing 1 mM EDTA, 10 mg/mL DNase, complete protease inhibitor cocktail (Roche), 50 mM KCl, and 25 mM sodium phosphate at pH 6.5. The cells were sonicated for protein solubilization and insoluble cell debris was removed by centrifugation. For purification the lysate was loaded onto a 20 mL HiLoad 16/10 SP Sepharose column (GE Healthcare) and proteins were eluted with a linear gradient ranging from 0.05 to 0.60 M KCl. Fractions containing GABARAP were pooled and further purified by gel filtration using a HiLoad 16/600 Superdex 75 pg column (GE Healthcare). Prior to fluorescent dye labeling, proteins were incubated in labeling buffer (25 mM Tris, 300 mM NaCl, 0.5 mM phenylmethane sulfonyl fluoride (PMSF), 0.5 mM ethylene glycol bis(2-aminoethyl ether)-*N*,*N*,*N*′,*N*′-tetraacetate (EGTA), 0.5 mM ascorbic acid, pH 7.5) containing 10 mM dithiothreitol (DTT) at room temperature for 20 min. DTT was removed by desalting on Sephadex G-25 (NAP-5 prepacked columns, GE Healthcare). Proteins were labeled in labeling buffer with an excess of BODIPY FL (BFL) iodoacetamide (ThermoFisher Scientific) for 2 h at room temperature. Unreacted dye was removed by desalting on NAP-5 prepacked columns.

3.3. NMR Data Acquisition and Analysis. NMR samples contained 0.5−1.0 mM [U-^{15}N] GABARAP or 0.7 mM [U-^{15}N] GABARAP-I G116C in the NMR buffer consisting of 25 mM sodium phosphate, 100 mM KCl, 100 mM NaCl, 0.1 mM

EDTA, 0.02% NaN_3 in H_2O/D_2O (9:1). NMR experiments were performed on spectrometers equipped with cryogenically cooled triple or quadruple resonance probes with z axis pulsed field gradient capabilities operating at proton Larmor frequencies of 600 and 900 MHz. The sample temperature was calibrated using methanol-d_4 (99.8%).[84] At least 615 (96) complex data points were acquired with a spectral width of 16 ppm (29 ppm) in the ^1H (^{15}N) dimension. NMR data were processed using NMRPipe.[85]

3.4. NMR Relaxation Experiments. ^{15}N spin relaxation data at temperatures of 5.0, 15.0, 25.0, and 35.0 °C were collected on a sample of 1.0 mM [U-^{15}N] GABARAP at 600 MHz and in the case of 25.0 °C also at 900 MHz. In addition, we collected ^{15}N spin relaxation data on a sample of 0.7 mM [U-^{15}N] GABARAP-I G116C at 25.0 °C and 600 MHz. Longitudinal relaxation rates R_1 were determined from ^{15}N inversion recovery experiments[86] with 10 different recovery delays (three in duplicate for error estimation) between 10 and 1200 ms using recycle delays of 2.0−2.5 s. Transverse relaxation rates R_2 were calculated from R_1 and rotating-frame relaxation rates $R_{1\rho}$ determined from ^{15}N spin-lock experiments[87] with 11 different spin-lock periods (three of them in duplicate for error estimation) between 2 and 100 ms at a field strength of 2.0 kHz using a recycle delay of 3.0 s. All data sets were acquired in an interleaved manner to reduce the effects of any sample or instrument instabilities over the duration of the experiment. R_1 and $R_{1\rho}$ were determined by three-way composition of the pseudo-three-dimensional NMR spectra using MUNIN.[88,89] {^1H}-^{15}N heteronuclear NOE values were calculated as the ratio of the peak intensities, extracted with NMRViewJ 8.0.3,[90] in two interleaved spectra recorded with and without proton saturation for the final 6 s of the recycle delay of 15 s,[86] with uncertainties estimated from the background noise of the spectra. Residues with large internal motions on the sub-nanosecond time scale as indicated by {^1H}-^{15}N values below 0.65 or involved in chemical exchange processes as indicated by R_2/R_1 ratios that deviate by more than 10% from the mean were considered to possess significantly increased internal mobility.[91] These mobile residues were excluded from the calculation of the rotational diffusion tensor on the basis of the crystal structure of GABARAP (PDB 1GNU,[92] hydrogen atoms added with the NIH version 1.2.1[93] of X-PLOR 3.851[94]) using Tensor 2.0[95] with the default parameters. Full "model-free" analysis of the ^{15}N relaxation data at 600 and 900 MHz recorded at 25.0 °C was performed by using the protocol of d'Auvergne et al. as implemented in relax version 4.0.0 (Table S1).[67,69,70,96,97] Because of the large number of experimental data points the statistical uncertainties on the extracted model parameters such as ρ_{global} are minute; systematic uncertainties were estimated by repeating the fits with ^{15}N transverse relaxation rates R_2 that are systematically lower or higher than the experimentally determined values by 2%, a typical systematic error described for ^{15}N relaxation experiments in the literature.[87,98]

3.5. NMR Translational Diffusion Experiments. The diffusion coefficient of 0.5 mM [U-^{15}N] GABARAP in the NMR buffer supplemented with 0.1% to 0.5% (v/v) dioxane as a reference was measured using 1D ^1H pulse gradient stimulated echo longitudinal encode-decode (PG-SLED) translational diffusion experiments[99] with individual rectangular-shaped or bipolar[100] sine-shaped encode/decode gradients and suppression of the H_2O resonance by WATERGATE[101] or weak presaturation at 600 MHz, 25.0 °C. The methyl group region in the 1D ^1H spectra was integrated, and the resulting intensities as a function of gradient strength were fit by a Gaussian decay.[102] As described in more detail in Supporting Information section 1, the decay constants from these fits were converted into diffusion coefficients[102] on the basis of the absolute strength of the pulsed field gradients, which had been calibrated from a diffusion experiment on D_2O using the known diffusion coefficient 1.9×10^{-5} cm^2/s at 25.0 °C.[99] The resulting diffusion coefficients $D_{\text{trans}}^{(\text{NMR})}$ were in turn converted into hydrodynamic radii $R_{\text{h,trans}}^{(\text{NMR})}$ on the basis of the Stokes−Einstein equation for translational diffusion (eq 21) assuming a viscosity of $\eta = 0.911$ mPa s interpolated for 10% D_2O at 25.0 °C.[103] Alternatively, the hydrodynamic radii were calculated relative to 0.1% or 0.5% (v/v) internal dioxane by assuming a hydrodynamic radius of 2.12 Å.[104] The diffusion coefficient and hydrodynamic radii are reported as mean ± standard deviation over two independent measurements.

3.6. Samples for Fluorescence Spectroscopy. Fluorescence measurements were performed with approximately 0.5 μM GABARAP (total protein concentrations including both labeled and unlabeled molecules) and up to 1.3 mM GABARAP for crowding experiments, in 25 mM sodium phosphate, 100 mM KCl, 100 mM NaCl, pH 6.9. Due to the different sensitivity of the methods, the fluorescent portion of the molecules was adjusted to approximately 50 nM for the fluorescence anisotropy measurements, whereas the confocal experiments (FCS) were performed at concentrations that were at least 10 times lower.

3.7. Fluorescence Anisotropy Decay $r(t_c)$. Note that in time-domain fluorescence spectroscopy the time recorded in time correlated single photon counting is usually referred to as t. However, as outlined in this work, it is actually a correlation time t_c, so that we keep this nomenclature for consistency. As the fluorescence decay starts usually at time $t = 0$ (defined by the excitation pulse), this value is omitted for convenience and the time-resolved fluorescence decay is written as $F(t+t_c) = F(t_c)$.

Polarization-resolved ensemble fluorescence decays were recorded using a FluoTime300 fluorescence lifetime spectrometer (PicoQuant, Berlin, Germany) equipped with a pulsed super continuum laser SuperK Extreme (NKT Photonics, Denmark) as a light source running at 19.51 MHz and a wavelength of 485 nm in a temperature-stabilized cell at 20.0 ± 0.1 °C. Typically, a total amount of 1.5×10^6 photons in 8 ps bins were collected per sample for both p- and s-polarization, $F_p(t_c)$ and $F_s(t_c)$, respectively. The fluorescence and anisotropy decays were recovered by global fitting of the sum and difference curves according to

$$F_{\text{sum}}(t_c) = F_p(t_c) + 2GF_s(t_c) = F(t_c) \tag{39a}$$

$$F_{\text{diff}}(t_c) = F_p(t_c) - GF_s(t_c) = F(t_c)\, r(t_c) \tag{39b}$$

where G is the detection efficiency ratio between the parallel and perpendicular channel. The procedure is described by Sindbert et al.[36] Due to distinct local environments sensed by the flexibly coupled dye, the fluorescence decays $F(t_c)$ were described by a triexponential decay with species fractions x_i and fluorescence lifetimes τ_i:

$$F(t_c) = F_0\left(\sum_{i=1}^{3} x_i e^{-t_c/\tau_i}\right) \qquad \sum_{i=1}^{3} x_i = 1 \tag{40}$$

Fluorescence anisotropy decays $r(t_c)$ were described by a weighted sum of exponentials and the parameters obtained were converted into the product of triple-exponential decays with rotational correlation times ρ_{fast}, ρ_{slow}, and ρ_{global}, and the related amplitudes r_{fast}, r_{slow}, and r_∞ with $\Sigma r_i = r_0$:

$$r(t_c) = \sum_{i=1}^{3} r_i \mathrm{e}^{-t_c/\rho_i} = r_0\left(\frac{r_{\text{fast}}}{r_0}\mathrm{e}^{-t_c/\rho_{\text{fast}}} + \frac{r_{\text{slow}}}{r_0}\mathrm{e}^{-t_c/\rho_{\text{slow}}} + \frac{r_\infty}{r_0}\right)\mathrm{e}^{-t_c/\rho_{\text{global}}} \tag{41}$$

where $r_0 = 0.37$ is the fundamental anisotropy of BFL.[105] For reliable calculation of order parameters, ρ_{global} was fitted globally for all six GABARAP variants and the fluorescence order parameter was calculated as $S^2 = r_\infty/r_0$. With $C(t_c) = r(t_c)/r_0$ (see eq 3), eq 41 becomes equivalent to eq 19.

3.8. pFCS. Polarization-resolved full fluorescence correlation spectroscopy was performed for GABARAP F62C-BFL and I41C-BFL variants with a confocal laser scanning microscope (FV1000, Olympus) equipped with a single photon counting device with picosecond time-resolution (detectors, PD5CTC, Micro Photon Devices, Bolzano, Italy; counting electronics, HydraHarp400, PicoQuant, Berlin, Germany) at 26 ± 1 °C. The sample was excited using the parked beam at 488 nm and the fluorescence F was collected in s- and p-polarized channels, $F_s(t)$ and $F_p(t)$, respectively. Full cross-correlation curves, $G_{s,p}(t_c)$ and $G_{p,s}(t_c)$, were obtained according to Felekyan et al.[106]

$$G_{s,p}(t_c) = 1 + \frac{\langle \delta F_s(t)\ \delta F_p(t+t_c)\rangle}{\langle F_s(t)\rangle\langle F_p(t)\rangle} \quad \text{and}$$

$$G_{p,s}(t_c) = 1 + \frac{\langle \delta F_p(t)\ \delta F_s(t+t_c)\rangle}{\langle F_s(t)\rangle\langle F_p(t)\rangle} \tag{42}$$

with the fluorescence fluctuations $\delta F(t) = F(t) - \langle F(t)\rangle$. The registered photon events were analyzed by employing a custom designed software package for multiparameter fluorescence spectroscopy, full correlation and multiparameter fluorescence imaging.[106] The applied factorized fitting function (eq 31) models translational diffusion in a 3D-Gaussian volume element $G_{\text{trans}}(t_c)$, up to three temporary dark states $G_b(t_c)$, rotational diffusion of a spherical rotator $G_{\text{rot}}(t_c)$, and photon antibunching $G_a(t_c)$:

$$G(t_c) = 1 + \frac{1}{N}G_{\text{trans}}(t_c) \times G_{\text{rot}}(t_c) \times G_b(t_c) \times G_a(t_c)$$

with

$$\begin{aligned}
G_{\text{trans}}(t_c) &= \left(1 + \frac{t_c}{t_{\text{trans}}}\right)^{-1}\left(1 + \left(\frac{\omega_0}{z_0}\right)^2 \times \frac{t_c}{t_{\text{trans}}}\right)^{-1/2}\\
G_{\text{rot}}(t_c) &= 1 + b_{\text{rot}}\left(\frac{1}{1+C}\mathrm{e}^{-t_c/\rho_{\text{global}}} + \frac{C}{1+C}\mathrm{e}^{-t_c/\left(S\rho_{\text{global}}\right)}\right)\\
G_b(t_c) &= 1 - b_1 + b_1\mathrm{e}^{-t_c/t_{b1}} - b_2 + b_2\mathrm{e}^{-t_c/t_{b2}} - b_3 + b_3\mathrm{e}^{-t_c/t_{b3}}\\
G_a(t_c) &= 1 - a\mathrm{e}^{-t_c/t_a}
\end{aligned} \tag{43}$$

Here, the observation volume is approximated by a 3D-Gaussian volume with $1/e^2$ radii in the lateral (ω_0) and axial direction (z_0), t_{trans} is the diffusion time, $b_{1,2,3}$ and t_{b_1,b_2,b_3} are amplitudes and times of the bunching terms, a and t_a are the amplitude and time of the antibunching term, S and C characterize the rotation model, b_{rot} and ρ_{global} are the amplitude and correlation time associated with rotational motion. As described above, factorization of the model function (eq 31) is based on the assumption of well-separated time scales for antibunching ($t_a \approx \tau_e$) and rotational correlation (ρ_{global}). With $t_a \approx 5$ ns and $\rho_{\text{global}} \approx$ 7−10 ns this condition is not sufficiently met in our case. Thus, parameters for an ideal spherical rotator ($S = 0.3$, $C = -0.519$)[61] were not used. Instead, to compensate for distortions by coupling between antibunching and rotational terms due to overlapping time scales, the two parameters $S = 0.65$, $C = -0.97$ were determined in a series of simulations. In addition to the shape of the correlation function, its apparent relaxation time is also affected by this coupling. By comparing simulated rotational correlation times with results obtained by fitting the model function to the simulations, we generated calibration data to derive correct rotational correlation times from the fit to the measured data (see Figure S2B).

3.9. Prediction of the Global Rotational Diffusion from the Molecular Shape. Using the HYDROPRO software[107] the global rotational correlation time was calculated as $\rho_{\text{global}} = 8.91 \pm 0.11$ ns at 20.0 °C (7.78 ± 0.10 ns at 25.0 °C). To this end, several PDB structures were used (PDB IDs: 1GNU,[92] 1KOT,[108] 1KLV,[109] 1KM7,[110] and 3D32[109]), the temperature set to 20.0 °C (25.0 °C), the viscosity to $\eta = 1.002$ mPa·s ($\eta = 0.890$ mPa·s), and harmonic means of relaxation times were averaged.

3.10. Molecular Dynamics Simulations. To gain a more detailed structural understanding of the nature of GABARAP dynamics we performed multiple MD simulations on the nanosecond and sub-microsecond time scale using Gromacs version 4.6.5.[111] The initial coordinates were taken from the PDB structure with ID 1GNU as this structure seems to have well-defined salt bridges and hydrogen bonds. However, the C-terminal region folds back toward the N-terminus in the crystal structure 1GNU, thereby forming a conspicuous salt bridge between the terminal carboxyl group and the terminal amino group. A stable salt bridge between the terminal groups is at variance with the NMR structure (PDB ID 1KOT) and dynamics (see below) of GABARAP, suggesting that the salt bridge between the termini featured in the 1GNU crystal structure is not stable in solution. To alleviate any conformational sampling issues that might arise from starting from a potentially artifactual local energy minimum, we decided to remove this salt bridge by simulating GABARAP-I instead, which lacks the C-terminal residue L117. The Amber99SB-ILDN[112] force field and the TIP3P[113] water model were used. The protein was centered in a cubic box with a minimum solute-to-wall distance of 1 nm. Water was added to the system as well as sodium and chloride ions to neutralize the system and to achieve a salt concentration of approximately 150 mM. The mass of all protons was increased to 4 u in order to remove the fastest degrees of freedom. After energy minimization and equilibration at a temperature of 27 °C and pressure of 1 bar, multiple MD simulations were started in the *NVT* ensemble with the temperature kept at 27 °C via a Nosé−Hoover thermostat.[114] Each simulation started from the same conformation with initial velocities randomly generated from a Maxwell distribution at 27 °C. The equations of motions were integrated with a time step of 2 fs and snapshots saved every 5 ps. Electrostatic interactions were calculated with the particle mesh Ewald algorithm[115] using a Fourier grid spacing of 0.12 nm and a cutoff of 0.9 nm for the short-range interactions. The same cutoff was used for the calculation of the van der Waals interactions. All bond lengths were constrained with the LINCS algorithm.[116] In total, 40 short MD simulations of 75−79 ns in length and 15 long simulations of 565−580 ns in length were run, amounting to a total of 11.7 μs of collected fast GABARAP dynamics.

DOI: 10.1021/acs.jpcb.8b08903
J. Phys. Chem. B 2019, 123, 1453−1480

3.11. Calculation of S^2 Order Parameters from MD Simulations.

To compute S^2 order parameters, the MD trajectories were divided into 1100 subtrajectories of 10 ns length each. This is more than 3 times longer than the rotational correlation time that GABARAP experiences in the MD simulations. Nevertheless, we tested that the usage of longer subtrajectories of 20 ns length did not affect the results. N−H bond vector autocorrelation functions were computed according to eq 8, where $\vec{\mu}_{IS}(t) = \vec{\mu}_{NH}(t)$ is the normalized bond vector at time t. We calculated the S^2 order parameters using both total and internal correlation functions. Internal correlation functions $C_{int}(t_c)$, which only capture internal N−H bond vector motions, were computed from trajectories that had been superimposed on the starting structure of each subtrajectory by minimizing the C_α root-mean-square deviation (RMSD), thereby removing overall rotational motion of the protein. S^2 order parameters were then computed for each subtrajectory as[56,117]

$$S^2 = \lim_{t_c \to \infty} C_{int}(t_c) \approx C_{int}(5\text{ ns}) \qquad (44)$$

and were subsequently averaged over all subtrajectories. Total correlation functions $C(t_c)$ were evaluated from the raw trajectories including protein rotations (see eq 9). They were first averaged over all subtrajectories and then fitted to multiexponential decays as given in eq 19. However, $C(t_c)$ was not fitted for all bond vectors using three decays. Instead, the number of exponential decays, ranging from one to three, was chosen for each bond vector individually in order to avoid overfitting of the data. The best-fit model was selected on the basis of the Akaike information criterion (AIC)[118] (see Supporting Information section 2 for more information).

For the calculation of the order parameters for side chains from the MD trajectories, the correlation functions of the side-chain bond vectors between heavy atoms were fitted to multiexponential decays following the same approach as for the N−H bond vectors above. Except for alanine, the C_α−C_β bond was omitted from the computation as it is directly correlated to the backbone dihedral angle rotations. Fast-rotating groups like the carboxyl groups of aspartate and glutamate were excluded. Moreover, bonds in aromatic rings, which can change their orientation as a result of overall ring rotation, but which are not representative of the overall side-chain conformation, were also not considered. The C_γ−C_δ bonds in phenylalanine and tyrosine are a good example for such bonds. The resulting S^2 values were averaged over all the bonds considered per side chain to obtain the corresponding side-chain order parameter.

For the calculation of S^2 order parameters from the MD trajectories we developed the Python software MOPS^2 (Molecular Order Parameters S^2), which is available free of charge under the following URL: https://github.com/schilli/MOPS. MOPS^2 allows one to calculate internal and global correlation functions and to determine the S^2 order parameters from the internal correlation functions according to eq 44, by fitting the global correlation functions using the Lipari−Szabo model presented in eq 19 with the possibility to invoke this method together with the AIC, or by using the method presented by Palmer.[24] The latter method was not applied in the current work. More information on MOPS^2 is given in the Supporting Information (section 3).

4. RESULTS

Using an integrated NMR, fluorescence, and MD approach we obtained results reporting on the protein mechanics and hydrodynamics of GABARAP. The global diffusion of a protein is mainly described by the overall rotational correlation time ρ_{global} in the approximation of a spherical molecule, whereas the internal motion is described by the order parameter S^2 and the internal correlation times ρ_{slow} and ρ_{fast}. ^{15}N NMR spin relaxation, time-resolved fluorescence anisotropy or fluorescence correlation spectroscopy (FCS), and MD simulations all report on these fast-motional parameters. The order parameters S^2 account for the restriction of the motion of the N−H bond vectors in the case of ^{15}N NMR spin relaxation data and of the dye attached to a side chain via a linker in the case of the fluorescence-based methods, while from MD simulations S^2 values are obtained for both N−H bonds and side chains.

4.1. NMR Spectroscopy.

^{15}N Relaxation Analysis. Backbone ^{15}N spin relaxation rates R_1 and R_2 and the {^{1}H}-^{15}N heteronuclear NOE values of 1.0 mM GABARAP at 600 and 900 MHz measured at 25.0 °C are shown in Figure 4. The ^{15}N spin relaxation rates are consistent at both field strengths. The overall average of the {^{1}H}-^{15}N heteronuclear NOE values of 0.80 ± 0.06 at 900 MHz and 0.70 ± 0.06 at 600 MHz reveals a stable tertiary fold. However, the C-terminal region from S113 onward shows continuously decreasing values reaching 0.403 ± 0.003 at 900 MHz and 0.19 ± 0.01 at 600 MHz, suggesting that the backbone of the C-terminal region is largely disordered. Similarly low {^{1}H}-^{15}N NOE values are observed for only one

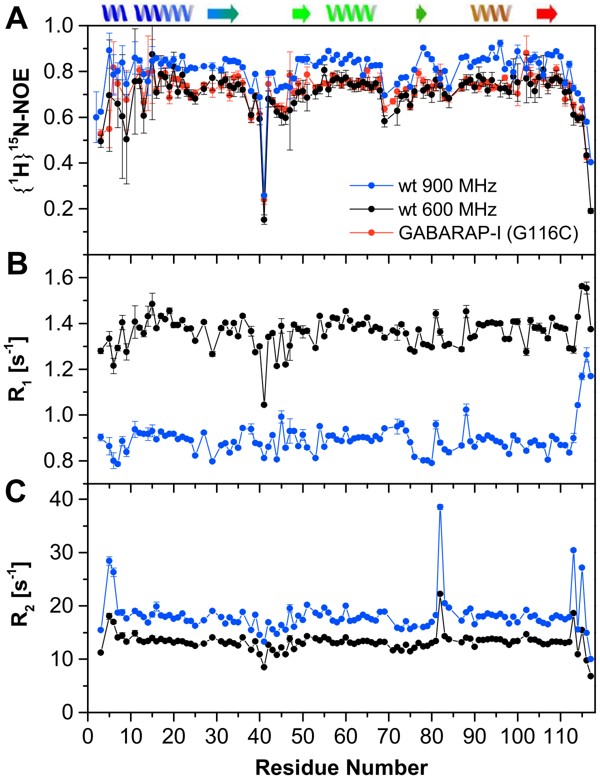

Figure 4. Backbone amide ^{15}N relaxation data of GABARAP as a function of residue number. (A) {^{1}H}-^{15}N heteronuclear NOE values of GABARAP and GABARAP-I G116C (red), (B) longitudinal relaxation rates R_1, and (C) transverse relaxation rates R_2, at 600 MHz (black) and 900 MHz (blue). Regular secondary structure elements are depicted on top of panel (A).

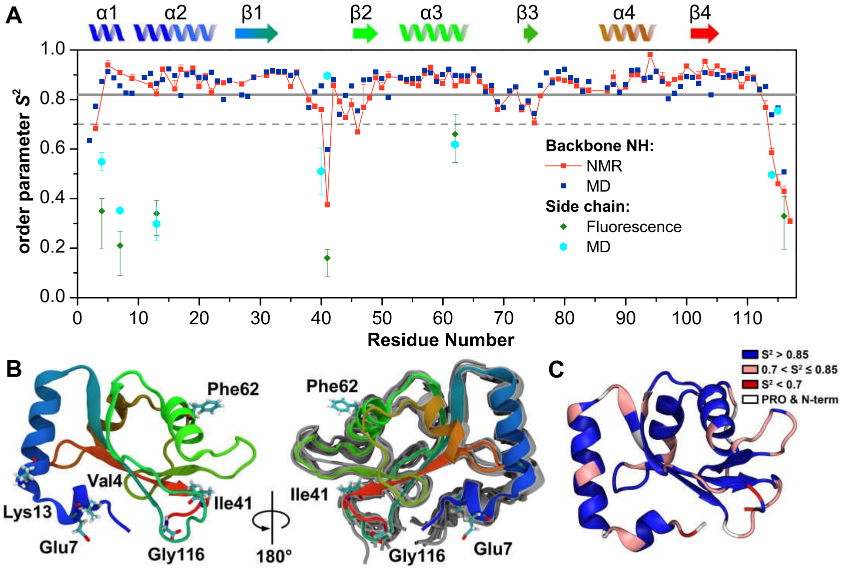

Figure 5. Backbone and side-chain flexibility of GABARAP. (A) Comparison of backbone amide bond vector generalized order parameters S^2 determined from ^{15}N NMR spin relaxation (red squares) and the backbone amide bond vector order parameters S^2 from MD simulations (blue squares), and comparison of the average side chain order parameters (cyan hexagons) from MD simulations and order parameters S^2 for BFL attached to cysteine side chains from fluorescence spectroscopy (green diamonds). The regular secondary structure elements are indicated above the panel. Error bars denote standard error. (B) Structural representation of GABARAP with the coloring changing from blue for the N-terminus via green to red for the C-terminus. The side chains of residues discussed in detail in this work are shown as sticks. In the right figure, several snapshots (in gray) from the MD trajectories are presented, revealing flexible regions. (C) GABARAP is colored on the basis of the backbone S^2 using four discrete categories as indicated by the legend.

additional residue, I41 in a loop region in spatial proximity to the C-terminal region. {^{1}H}-^{15}N NOE values below 0.65 indicative of increased backbone mobility[91] are further observed for the N-terminal region and the loop between helix α_3 and strand β_3. In addition to low {^{1}H}-^{15}N NOE values, the disordered C-terminal region also displays significantly elevated longitudinal ^{15}N relaxation rates, R_1. The C-terminal residue, L117, and I41 in the loop nearby also show the slowest transverse ^{15}N relaxation rates, R_2. Several residues in the N- and C-terminal regions as well as N82 in the loop between strand β_3 and helix α_4 exhibit conspicuously elevated ^{15}N R_2 rates at 25.0 °C due to large contributions from chemical exchange on the millisecond time scale to the ^{15}N line width. Unfortunately, the extensive chemical exchange line broadening has a negative influence on the signal-to-noise ratio of the affected NMR resonances and hence on the experimental uncertainties of the spin relaxation data in the N-terminal region. Importantly, the {^{1}H}-^{15}N NOE values of GABARAP and GABARAP-I G116C are virtually identical within error, indicating that the dynamics of the backbone on the pico- to nanosecond time scale is fully conserved upon cleavage of L117 by the ATG4 family of proteases.

Model-Free Analysis. Detailed analysis of the ^{15}N relaxation data based on the Lipari−Szabo-type "model-free" approach (eq 23) reveals that the rotational diffusion tensor is not completely isotropic but is best described by an ellipsoid model with principal components of $D_{xx} = 1.60 \times 10^7$ rad/s, $D_{yy} = 1.68 \times 10^7$ rad/s, $D_{zz} = 1.93 \times 10^7$ rad/s at 25.0 °C (Table S1), corresponding to five rotational autocorrelation times of ρ_{-2} = 10.19 ns, ρ_{-1} = 10.00 ns, ρ_0 = 9.76 ns, ρ_{+1} = 9.08 ns, and ρ_{+2} = 9.07 ns. The orientation (principal axes) of the rotational diffusion tensor agrees closely with the overall shape of the protein as represented by the tensor of inertia of the crystal structure of GABARAP (PDB 1GNU) (data not shown). In the spherical approximation this rotational diffusion tensor reduces to an isotropic rotational diffusion constant $D_{\text{rot}} = (D_{xx} + D_{yy} + D_{zz})/3 = 1.74 \times 10^7$ rad/s, corresponding to a global rotational correlation time $\rho_{\text{global}} = 1/(6D_{\text{rot}})$ = 9.60 ns. Assuming a viscosity of η = 0.911 mPa·s interpolated for 10% D_2O at 25.0 °C,[103] this corresponds to a hydrodynamic radius (eq 20) of $R_{\text{h,rot}}^{(\text{NMR})}$ = 21.8 Å, indicating predominantly monomeric GABARAP molecules. Besides the global diffusion properties, model-free analysis provides the generalized order parameters, S^2, which reports on the local backbone mobility (Figure 5A, red squares). The average order parameter of $\langle S^2 \rangle = 0.84 \pm 0.01$ indicates high motional restriction of the orientation of most amide bond vectors, particularly in the regular secondary structure elements. In contrast, residues at the N-terminus, at the C-terminus, and in the two loops between strands β_1 and β_2 and between helix α_3 and strand β_3 exhibit enhanced flexibility as revealed by low-order parameters. Most notably, I41 in the loop close to the C-terminal region shows a very low S^2 value of 0.37, which is in the same range as the order parameters of the C-terminal residues G116 and L117.

NMR Translational Diffusion. The hydrodynamic radius of GABARAP was additionally determined by translational diffusion experiments (see section 3.5 and Supporting Information section 1) at a lower protein concentration of 0.5 mM. Analysis of the resulting diffusion coefficient $D_{\text{trans}}^{(\text{NMR})}$ = $(1.16 \pm 0.02) \times 10^{-10}$ m^2/s based on the Stokes−Einstein relation (eq 21) requires knowledge of the solvent viscosity, which is estimated to be η = 0.911 mPa s for a mixture of 90% H_2O and 10% D_2O.[103] In this case the hydrodynamic radius is calculated as $R_{\text{h,trans}}^{(\text{NMR})}$ = 20.7 Å ± 0.2 Å, corresponding to ρ_{global} = 8.2 ± 0.3 ns under these conditions.

4.2. Fluorescence Spectroscopy: Fluorescence Anisotropy and pFCS.

We apply two complementary fluorescence techniques[119,120] to map depolarization dynamics of proteins

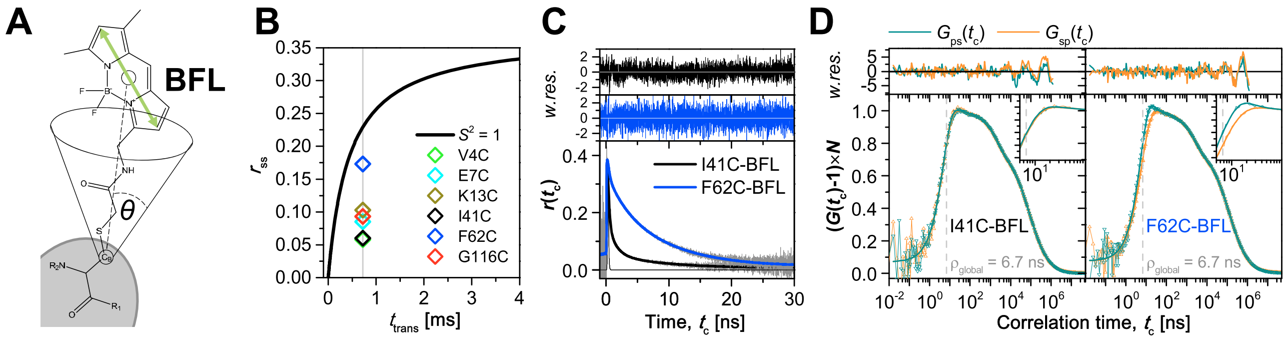

Figure 6. Fluorescence anisotropy decay and polarization-resolved FCS studies of cysteine variants of GABARAP labeled with BFL. (A) BODIPY FL (structure shown with the transition dipole moment marked by a green arrow) coupled to the side chain of cysteine. The diffusion cone is indicated with the angle θ that is related to order parameter S^2. (B) Relation between translational (x-axis) and rotational (y-axis) diffusion parameters probed with fluorescence assuming a diffusing rigid sphere, rigid attachment of the fluorophore $S^2 = 1$, and the following parameters: fluorescence lifetime τ_e = 5.35 ns, focal volume radius $\omega_0 = 0.5$ μm, and fundamental anisotropy $r_0 = 0.37$ (gray line, eq 37). The condition of $S^2 = 1$ is not achieved, and hence, the deviations of steady-state anisotropy r_{ss} from the ideal line (black) occur for all measured GABARAP variants. Note that the deviations depend on the rigidity of the fluorophore attachment (S^2) (Table 1). (C) Time-resolved anisotropy $r(t_c)$ of the variants I41C-BFL and F62C-BFL. The variant F62C is characterized by a slower anisotropy decay and larger amplitude of the global rotational diffusion term than I41C (Table S2B). As parameters were retrieved by global fitting to sum and difference curves (eq 39), the time-resolved anisotropy and weighted residuals are displayed for visualization purpose only. Analysis of ρ_{global} enables overcoming limits of the steady-state anisotropy regarding the flexibility of fluorophore attachment. (D) Cross-correlation curves $G(t_c)$ from pFCS were fit by a rotation model (ρ_{global} is marked by the dashed gray line). Note the difference in contrast between $G_{sp}(t_c)$ and $G_{ps}(t_c)$ of variants F62C-BFL and I41C-BFL (see insets for magnification) caused by the significantly higher internal mobility of the dye in the case of I41C-BFL. Top panels in (C) and (D) show the weighted residuals of the fit.

Table 1. Species-Averaged Fluorescence Lifetime $\langle\tau\rangle_x$ and Fluorescence Anisotropy Decay Parameters According to Eqs 19 and 38−41[a]

residue	$\langle\tau\rangle_x$ [ns]	r_{ss}	S^2_{fast}	ρ_{fast} [ns]	S^2_{slow}	ρ_{slow} [ns]	S^2	ρ_{global} [ns]
V4C	5.20	0.058	1	0.21	0.63	2.58	0.35	9.0
E7C	5.53	0.085	1	0.32	0.60	3.31	0.21	9.0
K13C	5.34	0.103	1	0.23	0.66	1.95	0.34	9.0
I41C	5.17	0.060	1	0.22	0.47	1.37	0.16	9.0
F62C	5.69	0.173	1	0.25	0.86	4.05	0.66	9.0
G116C	3.77	0.093	1	0.31	0.69	4.12	0.33	9.0

[a] All fit parameters of the detailed time-resolved fluorescence decay analysis are compiled in Table S2. The decays are plotted in Figure S3B.

from picoseconds to milliseconds in order to unravel their global correlation time and internal dynamics. To this end, we attached the dye BFL as an extrinsic fluorophore to individual cysteine side chains for five GABARAP variants with mutations at the residues V4C, E7C, K13C, I41C, or F62C of full-length GABARAP and G116C of GABARAP-I. Time-resolved fluorescence anisotropy, as being sensitive to rotational correlation times similar to or shorter than the excited-state lifetime of the fluorophore, τ_e, can distinguish fast internal motions from motions slower than τ_e (see Figures 2A and 3A). For describing the motion of a dye with a short linker in a restricted environment, the wobbling-in-cone model has been shown to be the most informative for interpreting order parameters[28,29,36] (Figure 6A). This assumption appears to be appropriate, because the transition dipole direction of the BFL chromophore is parallel to the molecular long axis[121] and the attachment of the linker to the fluorophore is asymmetric. For estimating the relative contributions of internal and global motions to depolarization, we determine the deviation of measured steady-state anisotropy from theoretical steady-state anisotropy $r_{ss}(t_{trans})$ (see eq 37 and Figure 6B).

Fluorescence Lifetime τ and Anisotropy r. The measurements of the fluorescence lifetime indicated that our labeling strategy was successful and the dye is only weakly perturbed by the coupling. Although we observed multiexponential fluorescence decays of the tethered BFL for all positions (see Tables 1 and S2C), which required three exponential components (eq 40), in most GABARAP variants the fluorescence decay of BFL has only small fractions of shorter fluorescence lifetimes resulting from quenching. This leads to long species-averaged fluorescence lifetimes $\langle\tau\rangle_x$ ranging between 5.2 and 5.7 ns and a high fraction of unquenched dye species $x_1 > 87\%$, while the lifetime of the free dye is $\tau \approx 5.9$ ns. The variant GABARAP-I G116C with BFL at the flexible C-terminus has exceptional properties with only 65% of unquenched species and $\langle\tau\rangle_x = 3.8$ ns (see Table S2C).

The order parameters of the six variants determined from the analysis of $r(t_c)$ using eqs 39−41 and transformation according to eqs 3 and 19 are compiled in Table 1 (decays see Figure S3B, fit parameters see Table S2) and plotted in Figure 5A (green diamonds). The anisotropy decays exhibit two local relaxation processes with ρ_{fast} ranging from 0.21 to 0.32 ns for the different variants and ρ_{slow} ranging from 1.4 to 4.1 ns, with a global rotational correlation time ρ_{global} = 9.0 ns fitted jointly for six variants. The most significant differences are observed between the anisotropy decay curves $r(t_c)$ of the dye attached to positions I41C and F62C (Figure 6C), showing a much faster decay for I41C. The S^2 values at residues V4C, E7C, K13C, I41C, and F62C of GABARAP and G116C of GABARAP-I show various extents of rigidity, with F62C-BFL being the most rigid residue (S^2 = 0.66) and I41C-BFL being the most flexible (S^2 = 0.16). Order parameter and global rotation are correlated in our model, so that the statistical error of the fitting procedure is high. Moreover, for positions with lower order parameter, the global rotation can be determined less precisely. To reduce the uncertainty of the parameters, it is convenient for molecules with a nearly spherical shape to approximate rotation by a single average global rotational correlation time which is computed in the joint fit for all six variants. Note that determination of slow global correlation times by fluorescence anisotropy decay analysis is extremely sensitive to instrumental factors such as the G-factor in eq 38 and 39. Therefore, the G-factor was calibrated by repeated measurements while the setup and sample were not disturbed during the measurement procedure. In repeated measurements of the variant F62C with the largest S^2 value, the global correlation time was determined to be $\rho_{global} = 9.2 \pm 0.4$ ns at 20 °C, i.e., 8.0 ± 0.4 ns converted for 25 °C.

pFCS. We studied the most distinct GABARAP variants labeled at the positions I41C and F62C by analyzing the two polarization-resolved full cross-correlation curves $G_{sp}(t_c)$ and $G_{ps}(t_c)$ (eqs 42 and 43, Figure 6D). The flexibility of the I41C side chain results in virtually complete loss of polarization contrast, so that the difference between the cross-correlation curves $G_{sp}(t_c)$ and $G_{ps}(t_c)$ and the corresponding correlation amplitudes b_{rot} (eq 43) becomes very small in Figure 6D, whereas the two curves for F62C are clearly distinct in the time range of 10 ns, which is a hallmark for fast rotational motions (Table S3). These findings agree fully with the time-resolved anisotropy measurements. A detailed curve analysis including simulations for calibration of the cross-correlation effects between the antibunching and rotational diffusion terms (see section 3.8 and Figure S2A,B)) revealed $\rho_{global} = 6.7^{+2.3}_{-1.3}$ ns at 26 °C for the F62C variant ($\rho_{global} = 6.9^{+2.4}_{-1.3}$ ns converted for 25 °C).

FCS Translational Diffusion. In addition, we measured also fluorescence correlation curves for determining the translational diffusion coefficient of labeled GABARAP from the FCS diffusion term (see Supporting Information section 4). We measured correlation curves at a range of low irradiances (Figure S4) to exclude saturation effects for determining an average translational diffusion time $\langle t_{trans} \rangle = 0.720 \pm 0.013$ ms, which corresponds to a translational diffusion coefficient of $D_{trans} = (1.18 \pm 0.09) \times 10^{-10}$ m²/s at 25 °C.

4.3. MD Simulations.

Backbone S^2 Order Parameters. The N−H bond vector order parameters, S^2, computed from multiexponential fits to the total correlation function $C(t_c)$ derived from the MD simulations are generally in very good agreement with those derived from NMR spectroscopy (Figure 5A). Larger deviations are mainly present at the termini and in other flexible regions. The S^2 values obtained from the internal correlation functions as $C_{int}(5\,\text{ns})$ (eq 44) are not shown because they are virtually indistinguishable from the S^2 values from the multiexponential fits to $C(t_c)$, with a root-mean-square deviation of 0.014 and a Pearson correlation coefficient of 0.99. Rigid N−H bonds are often but not always overfitted when more than the global exponential decay is used, while more complex models with one or two additional internal decay times fit the flexible N−H bonds best (Figure 7A, Figure S5A−C). The most rigid part of GABARAP can be found in the core of the protein, formed by the β-sheet and parts of α_4, where most of the N−H bonds can be fitted by a global exponential decay only (Figure S5D). Many of the residues located in the various loops, however, require three decay times due to their inherent flexibility. In three of the four helices there are also residues that had to be fit by three decay times even though the corresponding backbone S^2 values are larger than 0.8, such as residues E17 and K24 in helix α_2. Panels B−D of Figure 7 show histograms of the predicted correlation times. The fastest (i.e., initial) decay times for the N−H bond vector reorientation are shorter than the interval at which the structures sampled during the MD simulations were saved (5 ps). They are a result of fast internal motions like bond angle bending, which lead to fast changes of the N−H bond vector orientation represented in our fits by the order parameter ${S_{init}}^2$. The average value of the predicted global rotational correlation times, ρ_{global}, is 2.84 ns with a standard deviation of 0.20 ns and a standard error of 0.02 ns. The values for ρ_{global} cluster narrowly around this average value for the residues fitted with only a global decay, while the range of ρ_{global} for the residues fitted with internal decay times is larger, ranging from about 2 ns up to 3.4 ns (Figure 7B). The simulated global rotational correlation times have to be scaled by a factor of 2.80 ± 0.04 because the viscosity of the TIP3P water model used in our MD simulations is lower than that of real water.[122] Therefore, the predicted global rotational correlation time is $\rho_{global} = 7.95 \pm 0.56$ ns at 27 °C (8.32 ± 0.59 ns at 25 °C). In Figure S6A the calculated ρ_{global} values are color mapped onto the protein structure. Since the rotational diffusion tensor of GABARAP as determined by model-free analysis of the ^{15}N NMR relaxation data is not completely isotropic (see above), ρ_{global} is expected to be larger (slower) or smaller (faster) than the isotropic value depending on whether the corresponding N−H bond vector is aligned parallel or perpendicular, respectively, to the fastest principal axis (D_{zz}) of the rotational diffusion tensor. The strong correlation with the rotational autocorrelation times predicted from the experimentally determined rotational diffusion tensor (Figure 8C) demonstrates that the variance in ρ_{global} extracted from the MD trajectories primarily reflects the anisotropy of rotational diffusion. The single conspicuous outlier in the distribution of ρ_{global} from MD simulations (Figure 7B) is G116 with 1.96 ns, for which the internal motions appear to be sufficiently slow to be entangled with the global rotational motion (i.e., the factorization of eq 9 is

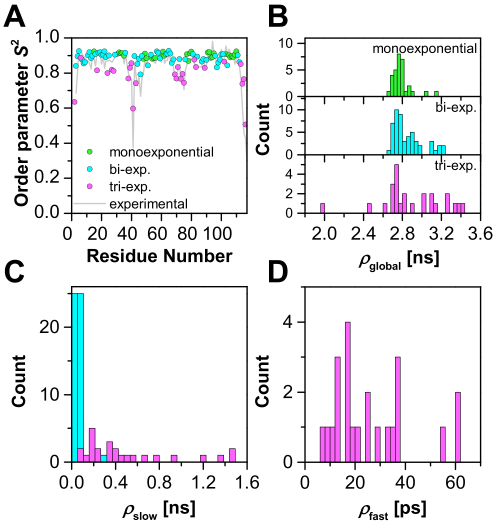

Figure 7. Flexibility analysis by MD simulations. Order parameter S^2 (A) and correlation times (B)−(D) extracted from MD trajectories by fitting the global correlation functions to one (green), two (blue), or three (magenta) exponential decays. The most complex model that did not overfit the bond vector correlation function was selected for each amino acid. This accounts for one global rotational correlation time ρ_{global} and maximum two internal correlation times ρ_{slow} and ρ_{fast}, the distributions of which are shown in panels (B)−(D).

DOI: 10.1021/acs.jpcb.8b08903
J. Phys. Chem. B 2019, 123, 1453−1480

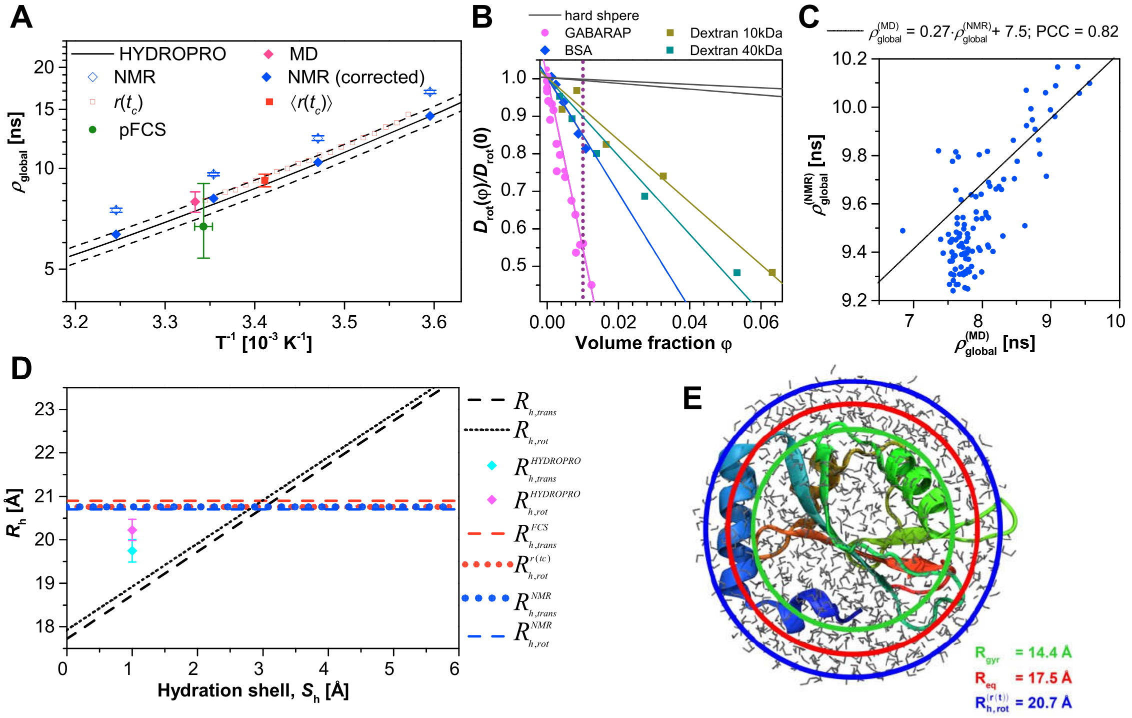

Figure 8. Hydrodynamics of GABARAP. (A) Temperature dependence of ρ_{global} obtained by NMR (corrected by 18% factor), fluorescence spectroscopy, and MD shows good agreement with structure-based prediction tools (HYDROPRO) across various temperatures. (B) Molecular relation between relative rotational diffusion ($D_{rot}(\varphi)/D_{rot}(0) = \rho_{global}(0)/\rho_{global}(\varphi)$) and concentration (volume fraction, φ) and type of cosolute as obtained from fluorescence anisotropy decays. The difference in interaction strength is visualized as the slope of the solid lines ($h_{GABARAP}$ 41.2 ± 1.6, h_{BSA} 13.9 ± 1.0, $h_{Dextran10}$ 7.5 ± 0.5, $h_{Dextran40}$ 9.4 ± 0.6). A large deviation from the theoretical relation for hard spheres (black line; h = 0.41 to 0.7) is clearly visible. (C) The strong correlation between the distribution of residue-specific ρ_{global} calculated from MD trajectories (abscissa) and back-calculated from the fully anisotropic rotational diffusion tensor from NMR relaxation (ordinate) with a Pearson correlation coefficient (PCC) of 0.82 reveals that NMR spectroscopy and MD simulations are both sensitive to the anisotropy of the rotational diffusion of GABARAP. Tyr115 and Gly116 have been omitted from this analysis because their conformation in the PDB structure 1GNU used as a basis for the NMR analysis appears to be a crystallization artifact, as indicated by MD simulations. (D) Hydrodynamic radii $R_{h,rot}$ (dotted black line) and $R_{h,trans}$ (dashed black line) calculated for the prolate ellipsoid of revolution with semiaxes of 23.0 and 15.2 Å (equivalent sphere: R_{eq} = 17.5 Å), which has approximately the same tensor of inertia as the crystal structure of GABARAP (PDB 1GNU) after addition of hydrogens, as a function of the thickness of the hydration shell, S_h. $R_{h,rot}{}^3 = F_{rot} \times R_{eq}{}^3$ and $R_{h,trans} = F_{trans} \times R_{eq}$ with the shape factors $F_{rot}(S_h)$ and $F_{trans}(S_h)$ and $R_{eq} = \sqrt[3]{(15.2\text{Å} + S_h)^2 \times (23.0\text{Å} + S_h)}$ (details see Supporting Information section 7). Diamonds represent the hydrodynamic radii predicted by HYDROPRO; horizontal lines, the experimentally determined hydrodynamic radii. (E) Solvated GABARAP is shown (water molecules in gray). The green circle indicates the radius of gyration, R_{gyr}, while the red circle represents the radius R_{eq} of the equivalent sphere of equal volume. The hydrodynamic radius obtained from time-resolved fluorescence anisotropy, $R^{(r(t))}_{h,rot}$ is shown as a blue circle.

not valid in this case) and hence complicate the interpretation of the multiexponential fit of its N−H bond vector correlation function. For the internal correlation times, we observe the same trend as for ρ_{global}: ρ_{slow} has a larger variance for the residues fitted with two internal decays compared to those fitted with a single internal decay (Figure 7C). For the latter, the ρ_{slow} values are almost all below 120 ps, while for the former the ρ_{slow} values are quite evenly distributed between 120 ps and 1.5 ns. The correlation times ρ_{fast} are rather small with values between 7 and 110 ps (Figure 7D).

Side-Chain S^2 Order Parameters. The order parameters for the side chains were calculated from MD simulations in the same way as for the N−H bond vectors. In Table 2 and Figure 5A the results are given for those residues for which S^2 values were also determined using fluorescence, while in Figure S7 the MD results for all side chains can be seen. The MD-derived S^2 values were averaged over the individual side-chain bonds. The numbers in Table S4 indicate that the S^2 values for the individual bonds per side chain are generally close to each other so that their average is representative for that side chain. Exceptions are the long side chains of solvent-exposed and charged residues like K13 and R40. Here, some bonds are rather flexible while others do not reorient much. Table 2 further shows that, unlike for the N−H bond vectors, in most cases three exponential decays are required for fitting the total correlation function $C(t_c)$ given in eq 19, which reflects the generally higher flexibility of the side chains compared to that of the protein backbone. The average and standard deviation of the S^2 values for the side chains is 0.69 ± 0.21 while the same values for the backbone amide groups are 0.86 ± 0.07. However, while for most residues the side chains are more flexible than the backbone (see Figure S7), there are cases like I41 for which it is the other way around. In general, the flexibilities of the N−H bond vectors and the side chains are not correlated as the low Pearson correlation coefficient of 0.206 between the S^2 values for the backbone and side chains reveals.

The MD side-chain order parameters match the fluorescence-derived S^2 values remarkably well, with the exception of values for I41 (Figure 5A), whose side chain is almost completely rigid in the MD simulation (S^2 = 0.90), while the fluorescence

DOI: 10.1021/acs.jpcb.8b08903
J. Phys. Chem. B 2019, 123, 1453−1480

Table 2. MD Decay Parameters for the Backbone N−H Bond (bb) and Side-Chain Bonds (sc) of Residues Shown in Figure 7 According to Eq 19[a]

residue	bb/sc	no. of decays	S^2_{fast}	ρ_{fast} [ns]	S^2_{slow}	ρ_{slow} [ns]	S^2	ρ_{global} [ns]
V4	bb	2			0.89	0.10	0.87	3.1
	sc	3	0.89	0.063	0.86	0.75	0.55	2.6
E7	bb	2			0.88	0.09	0.86	3.2
	sc	3	0.88	0.045	0.73	0.47	0.35	2.2
K13	bb	2			0.88	0.47	0.87	2.8
	sc	3	0.82	0.102	0.61	0.90	0.30	3.4
R40	bb	3	0.90	0.012	0.88	0.11	0.86	2.7
	sc	3	0.89	0.054	0.74	0.72	0.51	2.3
I41	bb	3	0.81	0.013	0.65	0.17	0.60	2.6
	sc	[b]	0.93	0.016	0.92	0.15	0.90	3.0
F62	bb	1					0.90	2.8
	sc	3	0.89	0.028	0.81	0.42	0.62	2.6
V114	bb	3	0.82	0.017	0.78	0.21	0.74	2.7
	sc	2			0.85	0.53	0.50	2.0
Y115	bb	3	0.87	0.016	0.82	0.19	0.76	2.4
	sc	3	0.93	0.027	0.87	0.36	0.76	2.5

[a] For the side chains, average values are presented. The parameters for the individual side-chain bonds are given in Table S4. Decay times ρ_{global} need to be scaled by 2.8 for comparison with experimental data to correct for viscosity effects of the TIP3P water model. [b] For one of the CB-CG bonds, the correlation function was fitted with only two decays, while three decays resulted from the fitting procedure of the other CB-CG bond.

chromophore attached to this residue is almost completely flexible (S^2 = 0.16). The MD trajectories show that the side chain of I41 is deeply buried inside a hydrophobic pocket pointing toward the protein core, which reduces the solvent accessible surface area (SASA) of I41 by 89% compared to that of an isolated isoleucine. The stable hydrophobic packing in this position prevents any motions of larger amplitude. The backbone N−H bond of I41, however, shows very-low-order parameters in MD (S^2 = 0.60) and NMR (S^2 = 0.59) because it fluctuates between two stable conformations by rotations about the R40 Ψ and I41 Φ backbone dihedral angles (Figure 9A), facilitated by the fact that this NH group is not involved in hydrogen bonding. All other backbone dihedral angles of residues 39−42 are restricted to a single stable conformation (Figure 9B). These restrictions are due to interactions of the side chain of K35 with the backbone oxygen of I41 as well as hydrogen bonds between the side chain of D111 and both the NH group of R40 and its side chain. The most obvious explanation for the discrepancy between MD and fluorescence order parameters for the I41 side chain is that the mutation of I41 to cysteine with the bulky chromophore BFL attached to it disrupts the hydrophobic packing as present in the wild-type protein, thereby causing the chromophore to become exposed to the solvent and highly mobile. For comparison, the nearest neighbor R40 is more solvent-exposed with a relative SASA of 52% and therefore more mobile, leading to a simulated side-chain S^2 value of 0.51 (Figure 5A). Figure S8 confirms that the S^2 values of the side chains are inversely correlated to their SASA. Large side-chain S^2 values exceeding 0.8 are preferentially found in the core of the protein, whereas values below 0.4 occur mostly for solvent-exposed side chains on the protein surface. In Figure S8D the side-chain S^2 values are plotted versus (1 − SASA), where SASA is given for the side chains relative to their solvent accessibility in the isolated amino acids. The correlation between S^2 and (1 − SASA) is confirmed by a Pearson correlation coefficient of 0.71. Another noteworthy residue is F62 in helix α_3, for which we find a medium solvent accessibility of 51% but with the side chain being oriented toward the solvent (Figure 5B) and an intermediate side-chain mobility of S^2 = 0.62. Together with the highly rigid backbone in this helix, this was our motivation to probe the side-chain flexibility in this position experimentally with a fluorescence chromophore. The almost perfect agreement between simulation and experiment confirmed that our fluorescence approach is able to measure variations in side-chain flexibility as long as their hydrophobic packing is not disrupted by the introduction of the chromophore.

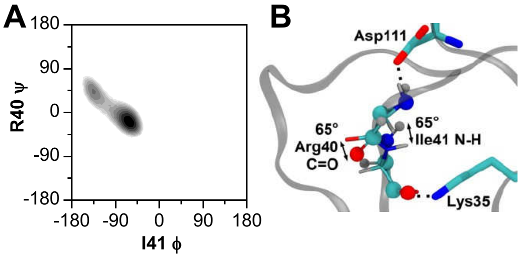

Figure 9. Backbone conformation of I41 and R40. (A) The Ramachandran plots (logarithmic scale) for Φ of I41 and Ψ of R40 reveals that the peptide bond plane between residues 40 and 41 fluctuates between two discrete conformations (with different stabilities, i.e., populations), which are shown in (B). The protein is shown as gray band and the backbone atoms of R40 and I41 and the side-chain atoms of K35 and D111 are shown in Licorice and colored by element (carbon, cyan; hydrogen, white; oxygen, red; nitrogen, blue) while the other stable state of the R40-I41 backbone is shown in CPK representation.

Interpretation of the Internal Decay Times. The MD data allow extracting the origin of the motions leading to ρ_{fast} and ρ_{slow} for all N−H bond vectors and side chains. Here, we limit this analysis to two representative examples. One of them is the aforementioned fluctuation of the backbone of R40/I41 between two stable states of the peptide plane (Figure 9). An analysis of the lifetimes of these two states reveals that the fast correlation time ρ_{fast} = 13 ps results from the fast interconversion between these two (R40 Ψ, I41 Φ) states. The slow correlation time, which is an order of magnitude larger than ρ_{fast} (ρ_{slow} = 173 ps), arises from the motion of the loop to which I41 belongs. A similar situation is, for example, evident for the N−H bond vector motion of A75, which was fitted with the two internal decay times ρ_{slow} = 651 ps and ρ_{fast} = 36 ps. Again, the slow and fast correlation times result from the flexibility of this loop region and internal backbone motions, respectively. Here, it is mainly the torsion angle A75 Φ, which fluctuates between −140° and −80°. However, since the carbonyl oxygen of D74 forms one or more H-bonds to the side chain of R65 80% of the time, this motion is somewhat slower than the backbone motion in I41. Comparison of the correlation times to those obtained from fluorescence (Table 1) and NMR (Table 3) reveals similarities but also differences between them, which will be discussed in section 5.3.

5. DISCUSSION

5.1. Common Theoretical Framework and Practical Considerations.

In section 2 we have provided a common theoretical framework and analysis for the overall rotational diffusion and internal protein dynamics as determined by NMR

Table 3. NMR Decay Parameters for Selected Residues

residue	S^2_{fast}	ρ_{fast} [ns]	S^2_{slow}	ρ_{slow} [ns]	S^2	τ_e [ns]
E7					0.91	0.03
K13	0.91		0.90	0.85	0.82	
R40	0.88		0.87	0.62	0.76	
I41	0.52	0.04	0.72	2.22	0.37	
F62	0.91		0.94	1.18	0.86	
V114	0.78	0.03	0.75	2.50	0.59	
Y115	0.74	0.03	0.62	3.14	0.46	
G116	0.75	0.05	0.58	1.90	0.43	

relaxation, fluorescence spectroscopy, and MD simulations. In practice, however, the sample conditions and the procedures to extract quantitative motional parameters differ significantly. NMR spectroscopy provides high-resolution three-dimensional structures and insight into global macromolecular diffusion and local intramolecular motions from spin probes abundantly distributed over the entire protein (typically, on a per-residue basis) but requires highly pure and sufficiently stable samples with sample concentrations close to the millimolar range. In contrast, fluorescence spectroscopy is sensitive enough to be performed over at least 10 orders of magnitude in concentration (pico- to millimolar) but usually requires protein modification by attachment of a fluorescent probe if no intrinsic fluorophore is in the region of interest. Attachment of a small uncharged dye with a short linker such as BFL to a cysteine side chain occurring naturally or introduced via site-directed mutagenesis allows quantification of overall and internal dynamics by analyzing the fluorescence anisotropy decay from time-correlated single photon counting (TCSPC) experiments or the correlation curves from pFCS. As explained above, fluorescence anisotropy decay is limited by the lifetime of the dye and hence particularly useful for the investigation of fast dynamics ranging from sub-nanoseconds to several nanoseconds, whereas pFCS is sensitive to slower motions beyond the upper limit of time-resolved anisotropy.[123,124] Since the fluorescent dye is attached to a cysteine side chain, it reports on side-chain flexibility instead of the backbone amide bond vector reorientation most commonly probed by NMR relaxation experiments. Backbone and side-chain dynamics can differ significantly[125] and are thus complementary to each other. An atomistic visualization and interpretation of the motional parameters measured by NMR and fluorescence spectroscopy can be obtained from MD simulations, thereby revealing the nature and functional relevance of the experimentally detected protein motions.

5.2. Benchmarking of Overall Rotational Diffusion and Hydrodynamics.

Our benchmark study produced remarkably similar results for the overall rotational correlation times ρ_{global} (Table 4, Figure 8A) and the S^2 order parameters describing the amplitude of internal motions (Figure 5A) obtained with the three approaches under study, demonstrating the reliability of each of these methods. Nonetheless, we also observed several instructive differences for one of the three approaches, which could readily be explained using the other two methods, thus providing us with valuable insight and guidelines for future studies.

The backbone dynamics of GABARAP on the picosecond to nanosecond time scale is dominated by rigid-body overall rotational diffusion. The rotational correlation times calculated from $r(t_c)$ and from MD simulations and predicted by HYDROPRO are identical within experimental error (Table 4, Figure 8A), with an average value of $\rho_{\mathrm{global}} = 8.0 \pm 0.3$ ns in 100% H_2O at 25 °C. The global rotational correlation time of $\rho_{\mathrm{global}} = 9.4 \pm 0.2$ ns determined from ^{15}N NMR relaxation spectroscopy is 19% larger. This appears to be a very typical case because a literature survey of 17 proteins studied by both fluorescence and NMR spectroscopy showed that NMR relaxation resulted in approximately 18% larger rotational autocorrelation times than fluorescence anisotropy decay on average,[128] which was attributed to the higher sample concentrations typically used in NMR spectroscopy to obtain a higher signal-to-noise ratio. The authors of this study pointed out that three different mechanisms contribute to any concentration dependence of rotational diffusion in a nonideal (i.e., not infinitely dilute) sample, namely, (i) general viscosity effects (also referred to as crowding or microviscosity), (ii) heterogeneous self-association mediated by nonspecific interactions, and (iii) specific self-association (dimerization, trimerization, etc.) mediated by specific interactions.

Viscosity Effects, Crowding, and Self-Association. Viscosity effects due to differences in solvent composition or temperature were corrected via the Stokes–Einstein–Debye equation (eq 20) using tabulated values.[103] To test for the presence of crowding effects, we measured the global rotational correlation time of GABARAP-F62C-BFL by TCSPC in the presence of

Table 4. Summary of Global Rotational Correlation Times, ρ_{global} [ns][a]

	temperature [°C]							
method	5	15	20	25	26	27	30	35
$r(t_c)$ [ns][b]			9.2 ± 0.4	**8.0 ± 0.4**				
FCS [ns][c]				$\mathbf{6.9^{+2.4}_{-1.3}}$	$6.7^{+2.3}_{-1.3}$			
NMR [ns][d]	16.9 ± 0.2	12.3 ± 0.2		9.6 ± 0.1				7.5 ± 0.1
NMR [ns][e]	**16.4 ± 0.2**	**12.0 ± 0.2**		**9.4 ± 0.2**				**7.3 ± 0.1**
NMR [ns][f]				**8.0**				
MD [ns][g]				**8.3 ± 0.6**		8.0 ± 0.6		
HYDROPRO [ns][h]	14.2 ± 0.5	10.3 ± 0.6	8.9 ± 0.5	7.8 ± 0.4	7.6 ± 0.4	7.4 ± 0.4	6.9 ± 0.4	6.1 ± 0.4

[a]Bold indicates values extrapolated with the Stokes–Einstein–Debye law. The viscosity of the buffer was approximated by using data for water at different temperatures,[126] scaled for the effect of dissolved salt ($\eta = 0.9000$ mPa·s for 248 mM NaCl:KCl (ratio 1:1) aqueous solutions at 25 °C[127] [b]GABARAP F62C-BFL approximately 50 nM and 0.5 μM unlabeled GABARAP. The error was determined by repeated measurements. [c]The correction is outlined in Figure S2A. [d]Fit to an ellipsoid diffusion model based on model-free analysis[69,70] (the parameters are compiled in Table S1). [e]Values extrapolated assuming NMR buffer with 100% H_2O. [f]Values extrapolated to low concentration (18% correction after Damberg et al.[128]). [g]Mean and standard error from data in Figure 4B, scaled by a factor of 2.80 ± 0.04 to account for too low TIP3P-water viscosity (from Mao et al.,[122] interpolated to 300 K). [h]Average value obtained by HYDROPRO for the PDB IDs 1GNU, 3D32, 1KLV, 1KOT (including 5% error as declared by the authors;[107] for individual values see Table S5, here scaled for viscosity of the buffer by a factor 0.90/0.89).

three crowding agents of different molecular size, Dextran10 (10 kDa), Dextran40 (40 kDa), and bovine serum albumin (BSA, 66 kDa). Following the methodology described by Roosen-Runge et al. (see Supporting Information section 5)[129] we plot the relative rotational diffusion coefficient $D_{\mathrm{rot}}(\varphi)/D_{\mathrm{rot}}(0)$ versus the volume fraction φ occupied by the crowding agent. The interaction strength is visualized as the negative slope h of the solid lines (eq S5.1) in Figure 8B: $h_{\mathrm{Dextran10}} = 7.5 \pm 0.5$, $h_{\mathrm{Dextran40}} = 9.4 \pm 0.6$, $h_{\mathrm{BSA}} = 13.9 \pm 1.0$. The theoretical relation for hard spheres (Figure 8B, black line) using specific size ratios of the distinct crowding agents and the solute gives a considerably smaller interaction strength with $h = 0.41-0.70$.[130] This indicates that BSA and dextrans act as strong crowding agents and the effects depend on their molecular size. We then performed a titration with unlabeled GABARAP (14 kDa) up to the concentration range of the NMR measurements. The fact that the decrease of the rotational diffusion coefficient of GABARAP with increasing volume fraction is even stronger ($h_{\mathrm{GABARAP}} = 41.2 \pm 1.6$) than for BSA and dextrans suggests that the elevated rotational autocorrelation times observed at high concentrations probe not only molecular crowding but also self-association of GABARAP molecules. Our experimental data do not readily discriminate between heterogeneous self-association and specific self-association mediated by specific interactions. A simple dimerization model already describes the concentration dependence of ρ_{global} reasonably well, and we estimate the dissociation constant to be in the low-millimolar range (Supporting Information section 6, Figure S9). Self-association of GABARAP has been reported in the literature before and implicated in binding to tubulin and promoting its oligomerization into microtubules as well as $\mathrm{GABA_A}$ receptor clustering.[83,131,132] More recent studies have shown that, upon membrane-anchoring, the proteins from the GABARAP/MAP1LC3/Atg8 family oligomerize together with other autophagy-related proteins, thereby mediating membrane tethering and hemifusion to form the autophagosomal membrane compartments required for protein degradation by (macro)autophagy.[133,134] Note that while the millimolar bulk dissociation constant of soluble GABARAP is too weak to be physiologically relevant, anchoring of lipidated GABARAP-II molecules to developing autophagosomal membranes can easily result in local concentrations sufficient for effective tethering to other GABARAP-decorated membranes or to the microtubule cytoskeleton for vesicular trafficking. The insight gained from the integrated NMR, fluorescence, and MD study presented here thus constitutes an important stepping stone for a detailed investigation of the structural mechanism and functional role of the self-association of GABARAP-II anchored to suitable membrane mimetics such as nanodiscs[135] or in cells.

On the basis of the fluorescence anisotropy experiments, one would expect an increase of ρ_{global} by more than 70% at 1.0 mM GABARAP (Figure 8B and Figure S9), yet ρ_{global} from ^{15}N NMR relaxation is elevated by only 19%. This difference can be explained by the fact that the sensitivity of fluorescence anisotropy experiments does not depend on molecular size, whereas the faster transverse relaxation rates of stable oligomers are associated with substantially lower signals in the NMR spectra compared to the monomer. Thus, the experimentally determined relaxation rates are expected to predominantly reflect the monomeric form even in the presence of a moderate fraction of oligomers. Indeed, the moderate overestimation of ρ_{global} by 19% for GABARAP appears to be a very typical case in the literature,[128] so we used the average literature value of 18% to correct ρ_{global} from NMR relaxation experiments for the influence of the high sample concentration in Table 4. Unless an accurate value for ρ_{global} from NMR relaxation spectroscopy is an absolute requirement, our work thus suggests that in practice it will often be more efficient not to spend many weeks of often prohibitively expensive NMR measurement time on dilute samples or concentration series, especially if sample stability is an issue, but instead to record the NMR experiments on samples with high signal/noise ratio to obtain experimental values for the anisotropy of the rotational diffusion and internal motions and to complement the NMR experiments with fluorescence experiments and MD simulations to investigate concentration-dependent effects on ρ_{global}.

Shape Anisotropy. Whereas the determination of rotational diffusion parameters by fluorescence spectroscopy with a single chromophore is limited by the assumption of isotropic rotational diffusion, NMR relaxation spectroscopy and MD simulations probe a large number of bond vectors in the molecule simultaneously and depending on its orientation relative to the rotational diffusion tensor each bond vector will experience a slightly different rotational autocorrelation time if the rotational diffusion tensor is anisotropic (Figure 8C). The molecular shape of GABARAP deviates significantly from spherical geometry (Figure 8E). Accordingly, model-free analysis of the ^{15}N NMR relaxation rates revealed a fully anisotropic rotational diffusion tensor, and this anisotropy is also observed in the MD trajectories (Figure 8C). In terms of magnitude, MD simulations appear to be even more sensitive to the anisotropy than ^{15}N NMR relaxation because the variance in ρ_{global} is larger (Figure 8C), which appears to be a property of the TIP3P water model.[136] After addition of hydrogen atoms, the crystal structure of GABARAP (PDB 1GNU) has approximately the same tensor of inertia as a prolate ellipsoid of revolution with semiaxes of 23.0 and 15.2 Å and an equivalent sphere of $R_{\mathrm{eq}} = \sqrt[3]{(15.2)^2 \cdot 23.0} = 17.5$ (Å). Assuming a hydration layer of $S_{\mathrm{h}} = 2.8$ Å, which reflects the van der Waals radius of an oxygen atom, we obtain an estimate for the equivalent sphere of hydrated GABARAP of $R_{\mathrm{eq}} = \sqrt[3]{(18.0)^2 \cdot 25.8} = 20.3$ (Å) and for the axial ratio of $P = 25.8$ Å/18.0 Å $= 1.433$ (Supporting Information section 7). Although this deviation from spherical geometry is significant and causes the rotational diffusion to be anisotropic, the effect of the corresponding shape factors[2] for such an ellipsoid of revolution of $F_{\mathrm{rot}} = 1.05$ and $F_{\mathrm{trans}} = 1.01$ on the isotropic rotational diffusion coefficient, $D_{\mathrm{rot}} = 1/(6\,\rho_{\mathrm{global}})$, and on the translational diffusion coefficient, D_{trans}, respectively, is actually smaller than typical experimental uncertainties. Moreover, $R_{\mathrm{h,rot}} = \sqrt[3]{F_{\mathrm{rot}}} \times R_{\mathrm{eq}} = 1.02 \times R_{\mathrm{eq}}$ is less than 1% larger than $R_{\mathrm{h,trans}} = F_{\mathrm{trans}} \times R_{\mathrm{eq}} = 1.01 \times R_{\mathrm{eq}}$. In other words, the spherical approximation for D_{rot} and D_{trans} is generally justified for proteins with a moderate deviation from spherical geometry such as GABARAP.

Hydrodynamic Radii and Hydration Layer. We extended our benchmark study by measuring also translational diffusion by NMR and fluorescence spectroscopy to compare the results with our benchmark value of $\rho_{\mathrm{global}} = 8.0 \pm 0.3$ ns for rotational diffusion. The spherical approximation allows us to compare rotational and translational diffusion coefficients obtained from different methods by converting D_{rot} and D_{trans} into hydrodynamic radii using eqs 20 and 21, respectively. The experimentally determined hydrodynamic radii are compiled in Table 5 and Figure 8D, together with the predictions from

Table 5. Summary of Hydrodynamic Radii R_h [Å] Calculated Using Eqs 20 and 21

	$R_{h,trans}^{(NMR)}$	$R_{h,rot}^{(NMR)\ a}$	$R_{h,trans}^{(FCS)}$	$R_{h,rot}^{(r(t))}$	$R_{h,rot}^{(r(t))}$	$R_{h,trans}^{(HydroPRO)\ b}$	$R_{h,rot}^{(HydroPRO)\ b}$
R_h [Å]	20.7 ± 0.2	20.7	20.9 ± 1.5	20.7 ± 0.3	20.9 ± 0.5	19.8 ± 0.3	20.2 ± 0.3

[a] Based on corrected ρ_{global} = 8.0 ns. [b] Obtained by HYDROPRO for the PDB IDs 1GNU, 3D32, 1KLV, 1KOT.

HYDROPRO. The hydrodynamic radii for rotation, $R_{h,rot} = 20.8 \pm 0.3$ Å, and translation, $R_{h,trans} = 20.7 \pm 0.2$ Å, averaged over the different experimental techniques are in agreement with each other. The fact that the hydrodynamic radius of $R_{h,trans}^{(NMR)} = 20.7 \pm 0.2$ Å obtained from NMR translational diffusion experiments on 0.5 mM GABARAP also agrees with the results from fluorescence spectroscopy and MD simulations supports the notion that the elevated rotational correlation time determined from ^{15}N relaxation experiments is indeed caused by the 2-fold higher sample concentration of 1.0 mM GABARAP. In order to determine the effective hydration layer, we compared these experimental values, which cluster between 20.7 and 20.9 Å, to the tertiary structure of GABARAP. Since the fluctuation of the molecular shape of GABARAP-I along the MD trajectory is negligible (radius of gyration $R_{gyr} = 14.3 \pm 0.1$ Å), we based this comparison on the static tertiary structure as represented by the crystal structure (PDB 1GNU), which in turn was approximated by the prolate ellipsoid of revolution with semiaxes of 23.0 and 15.2 Å and an equivalent (dry) sphere of R_{eq} = 17.5 Å (see above) plus a hydration layer S_h of variable thickness. Calculation of $R_{h,rot}$ and $R_{h,trans}$ for this ellipsoid of revolution (Supporting Information section 7) reveals that the experimentally determined hydrodynamic radii correspond to a hydration shell of about 3 Å (Figure 8D), which is similar to the van der Waals radius of a single oxygen atom (2.8 Å). They are slightly larger than $R_{h,rot}$ and $R_{h,trans}$ predicted from HYDROPRO, which approximates the molecular surface by a shell model with an implicit hydration shell of about 1.1 Å.[107] It has been suggested in the literature that the effect of the hydration layer may be at least partly due to dielectric friction, which depends on the charge distribution of the protein.[137] In fact, such complex electrostatic effects might also play a role in the concentration dependence of GABARAP hydrodynamics discussed above. The different radii, i.e., R_{gyr}, R_{eq}, and R_h are visualized in Figure 8E relative to the hydrated GABARAP molecule.

It is instructive to compare the value for $R_{h,rot}$ obtained in this integrative benchmark study with a convenient rule of thumb to calculate the minimum hydrodynamic radius for a protein by assuming a spherical shape, $R_{eq} = \sqrt[3]{(\nu_{prot} + h_{hyd}\nu_{H_2O})3M/(4\pi N_A)}$ (eqs 10 and 11 in Cantor & Schimmel[2]), which considers two contributions. First, the spherical volume of dry GABARAP, V_{dry}, is computed from the average specific volume of a protein (ν_{prot} = 0.73 mL/g), the molecular weight M = 13 920 g/mol, and the Avogadro constant, N_A.[18,73] The estimation works quite well: V_{dry} = 16.87 Å^3 corresponding to a dry radius of R_{eq} = 15.9 Å, which is ≈9% too small. A very similar value for V_{dry} is also obtained by the web tool "ProteinVolume 1.3",[138] which computes V_{dry} from the van der Waals volume and the solvent-excluded volume of the actual X-ray structure. The second contribution is an additional volume of hydration, V_{hyd}, which is calculated from the specific volume of water (ν_{H_2O} = 1.0 mL/g) weighted with a hydration factor h_{hyd} ranging between 0.23 and 0.80 g of water per gram of protein. Taking also the shape anisotropy into account ($R_{h,rot} = \sqrt[3]{F_{rot}} \times R_{eq} = 1.02 \times R_{eq}$), our benchmark study shows that h_{hyd} should be 0.81 ± 0.07 (626 ± 54 water molecules per GABARAP molecule) to match the hydrodynamic radius of GABARAP, $R_{h,rot}$ = 20.8 Å ± 0.3 Å. This calculation demonstrates that the hydrodynamic properties of proteins like GABARAP in water are governed by three factors: the total volume (van der Waals volume and solvent-excluded volume),[138] the shape (especially anisotropy) of the molecular surface, and the hydration shell, reflecting the fact that soluble proteins are usually not densely packed (i.e., the solvent-excluded volume is not zero) but more or less expanded with interfacial water molecules.[139] This is nicely visible in Figure 8E, which shows that even within the spheres defined by R_{gyr} and R_{eq} many water molecules are present. On average, there are 288 interfacial water molecules within R_{eq}, while the extra hydration layer leading to $R_{h,rot}$ adds another ≈413 water molecules. In agreement with other experimental[140] and theoretical[141] studies, we find that the total number of interfacial water molecules is approximately 12% higher than that estimated above on the basis of bulk water properties. Because the rotational correlation time ρ_{global} is approximately proportional to the total effective volume ($\sim R_h^3$) and the effective hydration layer contributes about 50% to the total effective volume of a protein like GABARAP, the effective relative hydration, h_{hyd}, can be estimated quite accurately if the molecular shape is known. These results support the findings of Bellissent-Funel et al.[8] that the interactions between soluble proteins and surrounding water molecules are an essential determinant for the structure, stability, flexibility,[142] and dynamics of proteins.

5.3. Internal Dynamics.

Correlation of Backbone and Side-Chain Order Parameters. The backbone order parameters S^2 from NMR spectroscopy and MD simulations primarily reveal internal motions in loop regions and at the termini, whereas the regular secondary structure elements of GABARAP show high rigidity (Figure 5). The fluorescence determined order parameters, which are sensitive to side-chain dynamics, are generally lower compared to the backbone amide order parameters obtained from ^{15}N NMR spin relaxation, especially in the N-terminal helical subdomain. This is confirmed by MD simulated side-chain order parameters S^2, which are also generally lower than the corresponding backbone S^2 (Figure S7). Interestingly, backbone and side-chain order parameters are generally not correlated. While we observe highly correlated backbone and side-chain dynamics for the C-terminus, the N-terminal region shows low backbone mobility but high side-chain mobility (Figures 2 and S7).

The trends of the average side-chain S^2 from MD and chromophore S^2 from fluorescence (Figure 5) agree remarkably well, with the notable exception of I41. While the NMR- and MD-derived backbone order parameters of I41 located in the loop region connecting strands β_1 and β_2 of GABARAP are the lowest outside of the terminal regions, which suggests very high flexibility of this loop region, the MD trajectories revealed that the low S^2 of I41 value mainly results from a flip of the the R40—I41 peptide plane between two distinct states (Figure 9). Fluorescence spectroscopy reports a high flexibility of the I41C-BFL side chain, whereas the side chain of I41 is rigidly embedded inside a hydrophobic pocket of GABARAP in the MD trajectories. In this particular case, dye attachment to

DOI: 10.1021/acs.jpcb.8b08903

cysteine at position 41 appears to sterically disrupt the native hydrophobic side-chain packing. Because cysteine also has little affinity for hydrophobic interactions, the order parameter probed by the fluorescence chromophore at position 41 is dominated by backbone motions.

Comparison of Internal Correlation Times. Although the order parameters obtained from NMR, fluorescence, and MD are highly consistent with each other, the fitted internal correlation times ρ_{fast} and ρ_{slow}, while covering similar time scales in the range of tens or hundreds of picoseconds and low nanoseconds, respectively, probe slightly different molecular processes. Comparison of the side-chain values for ρ_{slow} and ρ_{fast} obtained by fluorescence (Table 1) and MD (Table 2) reveals that the ratios $\rho_{\mathrm{slow}}^{(r(t))}/\rho_{\mathrm{slow}}^{(\mathrm{MD})}$ and $\rho_{\mathrm{fast}}^{(r(t))}/\rho_{\mathrm{fast}}^{(\mathrm{MD})}$ are quite similar for the same side chain, ranging from ≈2 for K13 to ≈9 for F62 and ≈13 for I41. The agreement between the correlation times from MD and fluorescence is generally better for the flexible N-terminal side chains than for the more rigid side chains of I41 and F62, for which MD predicts motions of smaller amplitude than probed by fluorescence spectroscopy for the dyes attached to these residues. Both MD and NMR predict correlation times ρ_{fast} below 100 ps for the fast backbone motions of the residues listed in Tables 2 and 3 and thus produce very similar results here. However, the same does not apply for ρ_{slow} with the ratio $\rho_{\mathrm{slow}}^{(\mathrm{NMR})}/\rho_{\mathrm{slow}}^{(\mathrm{MD})}$ ranging from ≈2 for K13 to ≈17 for Y115. And unlike to the side chains, we are not able to identify a dependency of that ratio on the S^2 order parameter. For instance, for Y115 this ratio is 16.5 while it drops to 4.3 for G116 even though their S^2 values are quite similar. It should be noted that in the case of NMR spectroscopy the global rotational correlation time, ρ_{global}, is extracted from a global analysis of the relaxation rates for all residues together, whereas the residue-specific internal correlation times, ρ_{fast} and ρ_{slow}, can generally be obtained from the fit only with somewhat lower precision. MD simulations, however, rely on protein force fields that are known to have difficulties to correctly reproduce the time scales of molecular processes as they were not parametrized for this purpose.[143] Fluorescence spectroscopy probes internal correlation times of a dye attached to cysteine side chains, not a native side chain. Substitution by cysteine may also disrupt the native side-chain packing and perturb the backbone, which is sensed by ρ_{slow}, which explains why the correlation times from fluorescence and MD agree better for solvent-exposed, flexible side chains than for the less flexible ones.

Selection of Labeling Sites for Fluorescent Dyes. In section 4.2 we concluded that the dye motion can be approximated by the wobbling-in-cone model, which has several practical implications for fluorescence spectroscopic applications. Our integrated order analysis allowed us to interpret fluorescence anisotropy measurements with respect to protein backbone and side-chain flexibility for monitoring the rigidity of its secondary and tertiary structure. Because the average side-chain S^2 order parameters from MD agree very well with the chromophore S^2 order parameters from fluorescence (Figure 5), they are a very helpful tool for selecting informative amino-acid residues for fluorescence labeling while minimizing disturbances by the amino-acid mutation and the label. In particular, our study demonstrates that MD side-chain order parameters color-coded onto the tertiary structure (Figure S8A−C) and/or correlated with the solvent-accessible surface area (Figure S8D) provide a straightforward way to identify the select few side chains such as F62 that are both surface-exposed (SASA > 50%) and thus unlikely to cause any disruption of the native packing upon dye attachment as well as sufficiently rigid ($S^2 > 0.6$) to efficiently sample global rotational diffusion of the protein, and hence constitute prime labeling candidates for sensitive and accurate measurement of ρ_{global} by fluorescence spectroscopy.

In a second application, this methodology has the potential for being also very useful for a accurate interpretation of Förster resonance energy transfer (FRET) measurements, which can only report on distances between dyes. Therefore, integrative structural modeling combining molecular simulations with FRET data is essential for achieving FRET-based atomistic structural models. Thus, the choice of an appropriate dye model to describe its spatial population density is essential for the accurate analysis of high-precision FRET measurements.[40,144−146] In this context, the presented characterization of the dye labeling sites via order parameters represents a rational tool for choosing an appropriate dye model.

Biological Relevance. The C-terminus is highly mobile on the picosecond to nanosecond time scale, indicated by low backbone and side-chain order parameters, which is contrary to the presence of a salt bridge between M1 and L117 connecting the N- and the C-terminus in the GABARAP structure 1GNU. Therefore, this salt bridge is most likely transiently formed allowing an open and closed state of the N- and C-terminus, which was also observed in the GABARAP homologue GATE-16.[16] This assumption is supported by our MD simulations of GABARAP-I, which revealed that the salt bridge between the terminal charges NH_3^+ and COO^- at M1 and G116, respectively, can form and break.

The C-terminal flexibility is conserved among GABARAP homologues and likely to be a prerequisite for enzyme processing required for lipidation and subsequent membrane anchoring.[78] GABARAP and its homologues are C-terminally processed by proteases of the Atg4 family cleaving L117 in order to expose the C-terminal G116. The heteronuclear NOE values of GABARAP-I G116C reveal similar results compared to the wild-type GABARAP concluding that the mobility of the C-terminus on the pico- to nanosecond time scale remains unaffected by Atg4B cleavage of L117. This is contrary to Atg8, the yeast homologue of GABARAP, which reveals higher rigidity upon exposure of the C-terminal glycine.[82] GABARAP and Atg8 share a strong structural similarity except of the N-terminus, which is unstructured in Atg8. Thus, the C-terminal dynamics might be affected by the N-terminus as they tend to interact with each other via a salt bridge. However, the propensity for this salt bridge may be reduced in Atg8 due to the positive charge of the C-terminal arginine residue and increases after cleavage of this residue, rigidifying the C-terminus.

Contrary to the correlated backbone (NMR) and side-chain (fluorescence) dynamics observed for the C-terminus, anti-correlated behavior is revealed in the N-terminal region showing low backbone flexibility but high side-chain flexibility. The N-terminal side-chain motion is likely to be relevant for ligand binding, since GABARAP is known to interact with tubulin and microtubules via its N-terminus.[76] Moreover, the N-terminal dynamics may also play a role for self-association of GABARAP, because crystallization under high-salt conditions resulted in an alternate conformation in which the N-terminal region is associated with the hydrophobic binding pockets of a neighboring molecule.[83]

5.4. Protein Mechanics: Detection of Potential Sites for Hinge Motions.

Structural plasticity and conformational transitions are essential for a multifunctional protein like GABARAP to interact with a multitude of different binding partners.[147] Hinge motions of relatively rigid subdomains about flexible joints[148] can result in large relative rotations, for example, by 154° in calmodulin.[149] Such hinges often involve only a small number of flexible residues because even a single backbone torsion angle can potentially provide the required rotational freedom. Therefore, we inspected our set of S^2 backbone and side-chain order parameters from MD simulations whether they can be used to characterize protein mechanics and identify potential hinges. For that we computed the average and standard deviation for the backbone amide groups $\langle S_{\mathrm{NH}}^2 \rangle = 0.87 \pm 0.05$, excluding the highly mobile residues K2, I41, and G116. For the identification of mobile segments, we found the backbone order parameter minus one standard deviation (i.e., $\langle S_{\mathrm{NH}}^2 \rangle < 0.82$) as a suitable threshold criterion, revealing four mobile segments in GABARAP around residues K24, D27, R28, V51, E97, and F104 (Figure S7), all of which contribute to the interface between helix α_2 in the NHD and the central β-sheet in the ULD (Figure 5C). The backbone dihedral angle mobility of the short loop before residues D27 and R28, which connects helix α_2 and strand β_1 and acts as a hinge for the hydrophobic ligand binding pocket between the NHD and the ULD, is also detected in dihedral angle principal component analysis applied to the MD trajectories (Figure S10). Although the NHD is connected to the ULD via several long-range interactions, most of the side chains surrounding the hinge itself show only intermediate rigidity (Figure S8B). Plasticity of the hinge between the NHD and ULD is functionally important for GABARAP to be able to accommodate a variety of different ligands in this hydrophobic binding pocket.[133] P26 in this hinge was also found to be an important determinant of the conformational mobility of the NHD in yeast Atg8.[150] Moreover, additional NHD motions (helix α_1) were suggested to occur for tubulin binding.[83]

Unfortunately, the NMR-derived backbone order parameters in the hinge region of the residues 27 and 28 are inconclusive because no relaxation data are available for R28 due to resonance overlap. However, preliminary single-molecule FRET measurements between the NHD and ULD suggest that this hinge acts indeed as a pivot for a large-scale conformational change on the microsecond time scale (to be published). We therefore propose such a detailed MD-based order parameter analysis as a more general tool to identify short, up to three residue-long loops that might be primed to act as hinges for functionally relevant conformational changes, even if these changes are too slow to be sampled during the length of the MD trajectory. In addition, one can use this experimental information to improve sampling of the motions in the potential hinge region by employing an enhanced MD simulation technique.[151]

6. CONCLUSION AND OUTLOOK

In this work we presented an integrated approach using NMR, fluorescence, and MD to study protein dynamics on the pico- to nanosecond time scale. The combination of these three methodologies proved to be tremendously beneficial, because each methodology entails unique strengths and shortcomings: NMR spectroscopy provides insight at atomic resolution on a per residue basis yet requiring highly concentrated and pure protein samples, whereas fluorescence spectroscopy involves residual mutations and dye attachments but will be the method of choice to study protein dynamics and interactions in complex systems, crowded environments, or the cell. While NMR and fluorescence spectroscopy provide information on the amplitude of the dynamics, MD simulations provide movies of protein motions at atomic resolution, enabling insight into protein mechanics and a critical evaluation of experimental data. However, current MD simulations of proteins in explicit solvent are generally limited to a few microseconds, restricting the processes that can be studied by MD to this time scale. Yet the complementarity and synergy of these three techniques allow a remarkably detailed analysis of the mechanics and hydrodynamics of proteins as demonstrated in this work for GABARAP. To this end, we developed a strategy to compare the different methods by means of the global correlation time and fast local protein dynamics. In particular, our work revealed that MD is a relevant tool to determine which solvent accessible amino acids serve best as probes for fluorescence anisotropy experiments. Thereby, the number of cysteine variants can be minimized and possible errors due to mutation are reduced. Additionally, we showed that pFCS is a well-suited technique in order to complement the results obtained by time-resolved anisotropy due to its sensitivity for slower processes.

Intriguingly, the quantification of the picosecond to nanosecond conformational dynamics already revealed several implications for self-association of GABARAP and its internal mechanics on slower time scales. Moreover, the common theoretical framework presented here as well as the cross-validation of the three techniques employed lay the foundation for studying the dynamics of GABARAP in more complex environments and on longer time scales. This will be possible by applying the here established approach integrating NMR, fluorescence spectroscopy, and MD simulations to study protein dynamics on multiple time scales ranging from nano- to milliseconds. Using enhanced simulation techniques in combination with high-performance computing, the exploration of protein dynamics on the sub-millisecond time scale is in principle possible. Moreover, it is attractive to combine these techniques with imaging to study molecular systems in more complex environments such as cells. For example, fluorescence anisotropy imaging microscopy (FAIM) has been used as a powerful tool to study molecular proximity and interactions in complex systems, such as hydrogels[152] and cells[12,153,154] by analyzing rotational diffusion with ultimate single-molecule sensitivity.[72] Confocal multiparameter fluorescence image spectroscopy allows one to simultaneously study rotational and translational diffusion so that molecular confinement can also be resolved.[152] Our aim is to extend our studies of the dynamics of GABARAP from *in vitro* to live cells in order to elucidate its contribution to the autophagic machinery. For all three methods pioneering work has demonstrated that they are also applicable in cells,[22,155−157] extending molecular biology to cell biology, or mimicking cellular conditions in the case of MD simulations.[158]

■ ASSOCIATED CONTENT

Ⓢ Supporting Information

The Supporting Information is available free of charge on the ACS Publications website at DOI: 10.1021/acs.jpcb.8b08903.

> Figures showing NMR results of spectral density functions and relaxation data, fitting and rotational diffusion model calibration for pFCS, sum and difference fitting of fluorescence anisotropy decays, power series of translational diffusion from FCS, NH-bond S^2 order parameter histograms, rotational correlation times, detection of molecular hinges, side-chain S^2 values, fit of GABARAP dimerization model to global rotation, and the

flexibility of backbone φ/ψ angles; tables of rotational diffusion tensors, fluorescence anisotropy decay model parameters, FCS model parameters, and MD decay parameters; and details of the fitting procedure of the NMR translational diffusion experiments, fitting of $C(t_c)$ from MD data, MOPS^2 software, translational diffusion measurements, crowding parameter calculation, oligomerization model, and prolate ellipsoid of revolution hydrodynamic model (PDF)

AUTHOR INFORMATION

Corresponding Authors

*E-mail: b.strodel@fz-juelich.de.
*E-mail: cseidel@hhu.de.
*E-mail: p.neudecker@fz-juelich.de.

ORCID

Dieter Willbold: 0000-0002-0065-7366
Birgit Strodel: 0000-0002-8734-7765
Claus A. M. Seidel: 0000-0002-5171-149X

Author Contributions

[#]Contributed equally.

Notes

The authors declare no competing financial interest.

Biographies

Christina Möckel studied physics at the University of Duisburg-Essen (Germany) and deepened her research on magnetic nanomaterials at the Lawrence Berkeley National Laboratory (USA). Afterward, she completed her Ph.D. at the Institute of Structural Biochemistry (ICS-6) at the Research Center Jülich (Germany). As part of this work, she investigated the dynamics of the autophagy-related protein GABARAP using state-of-the art NMR spectroscopy. She is currently working in the field of innovation management in materials science.

Jakub Kubiak received his M.Sc. from the University of Wroclaw (Poland) where he investigated thermodynamics of lipid interactions. He received his Ph.D. in Biophysics from the Institute of Physics and Chemistry, University of Southern Denmark, for research on complex bilayers at the MEMPHYS-Center for Biomembrane Physics. Currently, Jakub is postdoctoral fellow in Claus Seidel's group at Heinrich Heine University in Düsseldorf (Germany). He is interested in studying dynamical aspects of biomolecules using fluorescence spectroscopy.

Oliver Schillinger received his M.Sc. degree in Simulation Science at RWTH Aachen University (Germany). He completed his Ph.D. in the group of Prof. Dr. Birgit Strodel, where he studied protein structure and dynamics using MD simulations. He currently works as a Data Scientist in the energy sector, where he works on optimizing electricity distribution grids.

Ralf Kühnemuth studied chemistry in Hannover (Germany) and received his diploma and Ph.D. working in the field of surface science. In 1993 he joined the lab of Prof. John C. Polanyi in Toronto (Canada) as postdoctoral fellow to do research in surface-aligned photochemistry and in 1997 continued studying reactions at surfaces at the Fritz-Haber-Institute in Berlin (Germany). Since 1999 he has been a member of Claus Seidel's group, currently at Heinrich Heine University in Düsseldorf (Germany). His main research interests are development and application of fluorescence techniques for high resolution spectroscopy and imaging.

Dennis Della Corte earned his Ph.D. working on computational enzyme design at Research Center Jülich (Germany) with Prof. Gunnar Schröder in 2015. Following a three-year intermezzo as global project manager at Bayer AG, he recently rejoined academia. Dennis currently serves as assistant professor in the physics department at Brigham Young University (Provo, Utah, USA) and leads a research group focused on computational protein design.

Gunnar F. Schröder received his diploma in physics from the University of Göttingen (Germany). He received his Ph.D. from the Max-Plack-Institute for Biophysical Chemistry in Göttingen in 2004. He was a postdoctoral researcher at Stanford University (California, USA). Since 2009 he has led the Computational Structural Biology Group at Research Center Jülich (Germany), and since 2011 he has been a junior Professor at Heinrich Heine University Düsseldorf.

Dieter Willbold studied biochemistry in Tübingen (Germany), Bayreuth (Germany), and Boulder (Colorado, USA). He completed his Ph.D. in 1994 at the University of Bayreuth. After some more years in Bayreuth and a couple of research visits, e.g., at the Sackler School of Medicine of Tel-Aviv University, he headed a junior research group at the Institute for Molecular Biotechnology in Jena. In 2001 Willbold became an associate Professor at the Heinrich Heine University in Düsseldorf. Since 2004, he has been full professor at the Institute of Physical Biology in Düsseldorf and director of the Institute of Complex Systems at Research Center Jülich. His main interests are protein interactions with physiological and artificial ligands, high resolution structural biology, neurodegeneration, neuropathic pain, and autophagy.

Birgit Strodel studied chemistry at the Heinrich Heine University Düsseldorf and North Carolina at Chapel Hill (USA) and received her PhD in Theoretical Chemistry from the University of Frankfurt/Main (Germany) in 2005. She then joined the group of Prof. David J. Wales at Cambridge University (UK) as a postdoctoral research associate. Since 2009 she heads the Computational Biochemistry Group at the Jülich Research Centre and was appointed Professor at Heinrich Heine University Düsseldorf in 2011. Her research interests primarily involve the thermodynamics and kinetics of protein aggregation.

Claus A. M. Seidel studied chemistry at the Universities of Stuttgart and Heidelberg (Germany). He received his PhD in physical chemistry at the Heidelberg University in the group of Prof. Dr. Jürgen Wolfrum. Next, he was a PostDoc at a Sandoz research institute in Vienna (Austria). He was the head of a junior research team focused on single-molecule fluorescence spectroscopy at the Max Planck Institute for Biophysical Chemistry in Göttingen (Germany). Currently he is full professor in physical chemistry at the University Düsseldorf (Germany). His primary research interests are multimodal fluorescence spectroscopy and imaging and molecular biophysical chemistry.

Philipp Neudecker studied physics at the University of Bayreuth (Germany) and the State University of New York at Albany (USA), graduating in Bayreuth in 2003 with a doctoral thesis in NMR structural biology of allergens supervised by Paul Rösch. In 2004 he moved to the University of Toronto (Canada) as a postdoctoral fellow in the group of Lewis Kay to develop NMR relaxation dispersion methods and their application to protein folding, misfolding & aggregation. Since 2011 he is a research group leader at the Institute of Physical Biology at Heinrich Heine University Düsseldorf (Germany), where he continues to investigate the structure, dynamics, and function of proteins by NMR spectroscopy in concert with other biochemical and biophysical techniques.

ACKNOWLEDGMENTS

We thank Judith Fabig who did the QuikChange site directed mutagenesis of GABARAP variant I41C. The authors acknowledge access to the Jülich-Düsseldorf Biomolecular NMR Center. C.M. and O.S. thank the graduate school iGRASP$_{\text{seed}}$ and C.M.

also the NRW Research School BioStruct for funding. This work was funded by the Deutsche Forschungsgemeinschaft (DFG, German Research Foundation)—Projektnummer 267205415-SFB 1208 (projects A07, A08, B02, and B03). G.F.S. and B.S. gratefully acknowledge the computing time granted by the JARA-HPC Vergabegremium and VSR commission on the supercomputer JURECA at Forschungszentrum Jülich.

■ ABBREVIATIONS

NMR, nuclear magnetic resonance; NOE, nuclear Overhauser effect; TCSPC, time-correlated single photon counting; pFCS, polarization-resolved fluorescence correlation spectroscopy; MD, molecular dynamics

■ REFERENCES

(1) Palmer, A. G., III NMR characterization of the dynamics of biomacromolecules. *Chem. Rev.* **2004**, *104*, 3623−3640.

(2) Cantor, C. R.; Schimmel, P. R. *Biophysical Chemistry: Part II: Techniques for the study of biological structure and function*; W. H. Freeman and Company: San Francisco, 1980.

(3) Henzler-Wildman, K.; Kern, D. Dynamic personalities of proteins. *Nature* **2007**, *450*, 964−972.

(4) Schuler, B.; Hofmann, H. Single-molecule spectroscopy of protein folding dynamics-expanding scope and timescales. *Curr. Opin. Struct. Biol.* **2013**, *23*, 36−47.

(5) Yang, D.; Kay, L. E. Contributions to conformational entropy arising from bond vector fluctuations measured from NMR-derived order parameters: Application to protein folding. *J. Mol. Biol.* **1996**, *263*, 369−382.

(6) Tzeng, S.-R.; Kalodimos, C. G. Protein activity regulation by conformational entropy. *Nature* **2012**, *488*, 236−240.

(7) Sharp, K. A.; O'Brien, E.; Kasinath, V.; Wand, A. J. On the relationship between NMR-derived amide order parameters and protein backbone entropy changes. *Proteins: Struct., Funct., Genet.* **2015**, *83*, 922−930.

(8) Bellissent-Funel, M. C.; Hassanali, A.; Havenith, M.; Henchman, R.; Pohl, P.; Sterpone, F.; van der Spoel, D.; Xu, Y.; Garcia, A. E. Water determines the structure and dynamics of proteins. *Chem. Rev.* **2016**, *116*, 7673−7697.

(9) Neudecker, P.; Nerkamp, J.; Eisenmann, A.; Nourse, A.; Lauber, T.; Schweimer, K.; Lehmann, K.; Schwarzinger, S.; Ferreira, F.; Rösch, P. Solution structure, dynamics, and hydrodynamics of the calcium-bound cross-reactive birch pollen allergen Bet v 4 reveal a canonical monomeric two EF-hand assembly with a regulatory function. *J. Mol. Biol.* **2004**, *336*, 1141−1157.

(10) Kravets, E.; Degrandi, D.; Weidtkamp-Peters, S.; Ries, B.; Konermann, C.; Felekyan, S.; Dargazanli, J. M.; Praefcke, G. J. K.; Seidel, C. A. M.; Schmitt, L.; et al. The GTPase Activity of Murine Guanylate-binding Protein 2 (mGBP2) Controls the Intracellular Localization and Recruitment to the Parasitophorous Vacuole of Toxoplasma gondii. *J. Biol. Chem.* **2012**, *287*, 27452−27466.

(11) Stahl, Y.; Grabowski, S.; Bleckmann, A.; Kuhnemuth, R.; Weidtkamp-Peters, S.; Pinto, K. G.; Kirschner, G. K.; Schmid, J. B.; Wink, R. H.; Hulsewede, A.; et al. Moderation of Arabidopsis root stemness by CLAVATA1 and ARABIDOPSIS CRINKLY4 receptor kinase complexes. *Curr. Biol.* **2013**, *23*, 362−371.

(12) Kravets, E.; Degrandi, D.; Ma, Q. J.; Peulen, T. O.; Klumpers, V.; Felekyan, S.; Kühnemuth, R.; Weidtkamp-Peters, S.; Seidel, C. A. M.; Pfeffer, K. Guanylate binding proteins directly attack Toxoplasma gondii via supramolecular complexes. *eLife* **2016**, *5*, No. e11479.

(13) Peng, T.; Zintsmaster, J. S.; Namanja, A. T.; Peng, J. W. Sequence-specific dynamics modulate recognition specificity in WW domains. *Nat. Struct. Mol. Biol.* **2007**, *14*, 325−331.

(14) Petrović, D.; Frank, D.; Kamerlin, S. C. L.; Hoffmann, K.; Strodel, B. Shuffling active site substate populations affects catalytic activity: the case of glucose oxidase. *ACS Catal.* **2017**, *7*, 6188−6197.

(15) Bozoky, Z.; Krzeminski, M.; Muhandiram, R.; Birtley, J. R.; Al-Zahrani, A.; Thomas, P. J.; Frizzell, R. A.; Ford, R. C.; Forman-Kay, J. D. Regulatory R region of the CFTR chloride channel is a dynamic integrator of phospho-dependent intra- and intermolecular interactions. *Proc. Natl. Acad. Sci. U. S. A.* **2013**, *110*, E4427−E4436.

(16) Ma, P.; Schillinger, O.; Schwarten, M.; Lecher, J.; Hartmann, R.; Stoldt, M.; Mohrlüder, J.; Olubiyi, O.; Strodel, B.; Willbold, D.; et al. Conformational polymorphism in autophagy-related protein GATE-16. *Biochemistry* **2015**, *54*, 5469−5479.

(17) Langosch, D.; Scharnagl, C.; Steiner, H.; Lemberg, M. K. Understanding intramembrane proteolysis: from protein dynamics to reaction kinetics. *Trends Biochem. Sci.* **2015**, *40*, 318−327.

(18) Lakowicz, J. R. *Principles of Fluorescence Spectroscopy*; third ed.; Springer: New York, 2006.

(19) Bucci, E.; Steiner, R. F. Anisotropy decay of fluorescence as an experimental approach to protein dynamics. *Biophys. Chem.* **1988**, *30*, 199−224.

(20) Clore, G. M.; Driscoll, P. C.; Wingfield, P. T.; Gronenborn, A. M. Analysis of the backbone dynamics of Interleukin-1b using two-dimensional inverse detected heteronuclear ^{15}N-^{1}H NMR-spectroscopy. *Biochemistry* **1990**, *29*, 7387−7401.

(21) Karplus, M.; Kuriyan, J. Molecular dynamics and protein function. *Proc. Natl. Acad. Sci. U. S. A.* **2005**, *102*, 6679−6685.

(22) Dror, R. O.; Dirks, R. M.; Grossman, J. P.; Xu, H. F.; Shaw, D. E. Biomolecular simulation: a computational microscope for molecular biology. *Annu. Rev. Biophys.* **2012**, *41*, 429−452.

(23) Shaw, D. E.; Dror, R. O.; Salmon, J. K.; Grossman, J. P.; Mackenzie, K. M.; Bank, J. A.; Young, C.; Deneroff, M. M.; Batson, B.; Bowers, K. J.; et al. Millisecond-scale molecular dynamics simulations on Anton. *Proceedings of the Conference on High Performance Computing Networking, Storage and Analysis (SC '09)*; ACM: Portland, Oregon, 2009.

(24) Trbovic, N.; Kim, B.; Friesner, R. A.; Palmer, A. G., III. Structural analysis of protein dynamics by MD simulations and NMR spin-relaxation. *Proteins: Struct., Funct., Genet.* **2008**, *71*, 684−694.

(25) Schröder, G. F.; Alexiev, U.; Grubmüller, H. Simulation of fluorescence anisotropy experiments: probing protein dynamics. *Biophys. J.* **2005**, *89*, 3757−3770.

(26) Harvey, S. C. Transport properties of particles with segmental flexibility. I. Hydrodynamic resistance and diffusion-coefficients of a freely hinged particle. *Biopolymers* **1979**, *18*, 1081−1104.

(27) Harvey, S. C.; Cheung, H. C. Transport-properties of particles with segmental flexibility. II. Decay of fluorescence polarization anisotropy from hinged macromolecules. *Biopolymers* **1980**, *19*, 913−930.

(28) Kinosita, K., Jr.; Kawato, S.; Ikegami, A. A theory of fluorescence polarization decay in membranes. *Biophys. J.* **1977**, *20*, 289−305.

(29) Kinosita, K.; Ikegami, A.; Kawato, S. On the wobbling-in-cone analysis of fluorescence anisotropy decay. *Biophys. J.* **1982**, *37*, 461−464.

(30) Szabo, A. Theory of fluorescence depolarization in macromolecules and membranes. *J. Chem. Phys.* **1984**, *81*, 150−167.

(31) Scott, D. R.; Vardeman, C. F.; Corcelli, S. A.; Baker, B. M. Limitations of time-resolved fluorescence suggested by molecular simulations: Assessing the dynamics of T cell receptor binding loops. *Biophys. J.* **2012**, *103*, 2532−2540.

(32) Cross, A. J.; Fleming, G. R. Analysis of time-resolved fluorescence anisotropy decays. *Biophys. J.* **1984**, *46*, 45−56.

(33) Axelsen, P. H.; Prendergast, F. G. Molecular-dynamics of Tryptophan in ribonuclease-T1. II. Correlations with fluorescence. *Biophys. J.* **1989**, *56*, 43−66.

(34) Axelsen, P. H.; Gratton, E.; Prendergast, F. G. Experimentally verifying molecular-dynamics simulations through fluorescence anisotropy measurements. *Biochemistry* **1991**, *30*, 1173−1179.

(35) Babcock, J. J.; Brancaleon, L. The effect of local dynamics of Atto 390-labeled lysozyme on fluorescence anisotropy modeling. *Biopolymers* **2015**, *103*, 285−295.

(36) Sindbert, S.; Kalinin, S.; Hien, N.; Kienzler, A.; Clima, L.; Bannwarth, W.; Appel, B.; Muller, S.; Seidel, C. A. M. Accurate distance

determination of nucleic acids via Förster resonance energy transfer: implications of dye linker length and rigidity. *J. Am. Chem. Soc.* **2011**, *133*, 2463−2480.

(37) Best, R. B.; Hofmann, H.; Nettels, D.; Schuler, B. Quantitative interpretation of FRET experiments via molecular simulation: force field and validation. *Biophys. J.* **2015**, *108*, 2721−2731.

(38) Schuler, B.; Lipman, E. A.; Steinbach, P. J.; Kumke, M.; Eaton, W. A. Polyproline and the "spectroscopic ruler" revisited with single-molecule fluorescence. *Proc. Natl. Acad. Sci. U. S. A.* **2005**, *102*, 2754−2759.

(39) Corry, B.; Hurst, A. C.; Pal, P.; Nomura, T.; Rigby, P.; Martinac, B. An improved open-channel structure of MscL determined from FRET confocal microscopy and simulation. *J. Gen. Physiol.* **2010**, *136*, 483−494.

(40) Kalinin, S.; Peulen, T.; Sindbert, S.; Rothwell, P. J.; Berger, S.; Restle, T.; Goody, R. S.; Gohlke, H.; Seidel, C. A. M. A toolkit and benchmark study for FRET-restrained high-precision structural modeling. *Nat. Methods* **2012**, *9*, 1218−1227.

(41) Bocchinfuso, G.; Bobone, S.; Mazzuca, C.; Palleschi, A.; Stella, L. Fluorescence spectroscopy and molecular dynamics simulations in studies on the mechanism of membrane destabilization by antimicrobial peptides. *Cell. Mol. Life Sci.* **2011**, *68*, 2281−2301.

(42) Gendron, P. O.; Avaltroni, F.; Wilkinson, K. J. Diffusion coefficients of several rhodamine derivatives as determined by pulsed field gradient-nuclear magnetic resonance and fluorescence correlation spectroscopy. *J. Fluoresc.* **2008**, *18*, 1093−1101.

(43) Guo, J. C.; Han, K. S.; Mahurin, S. M.; Baker, G. A.; Hillesheim, P. C.; Dai, S.; Hagaman, E. W.; Shaw, R. W. Rotational and translational dynamics of Rhodamine 6G in a pyrrolidinium ionic liquid: A combined time-resolved fluorescence anisotropy decay and NMR study. *J. Phys. Chem. B* **2012**, *116*, 7883−7890.

(44) Majhi, D.; Pabbathi, A.; Sarkar, M. Probing the aggregation behavior of neat imidazolium-based Alkyl Sulfate (Alkyl = Ethyl, Butyl, Hexyl, and Octyl) ionic liquids through time resolved fluorescence anisotropy and NMR and fluorescence correlation spectroscopy study. *J. Phys. Chem. B* **2016**, *120*, 193−205.

(45) Palmer, A. G., III; Hochstrasser, R. A.; Millar, D. P.; Rance, M.; Wright, P. E. Characterization of amino-acid side-chain dynamics in a Zinc-finger peptide using C-13 NMR-spectroscopy and time-resolved fluorescence spectroscopy. *J. Am. Chem. Soc.* **1993**, *115*, 6333−6345.

(46) Fisette, O.; Lagüe, P.; Gagné, S.; Morin, S. Synergistic applications of MD and NMR for the study of biological systems. *J. Biomed. Biotechnol.* **2012**, *2012*, 154208.

(47) Markwick, P. R. L.; Malliavin, T.; Nilges, M. Structural biology by NMR: structure, dynamics, and interactions. *PLoS Comput. Biol.* **2008**, *4*, No. e1000168.

(48) Mocci, F.; Laaksonen, A. In *Nuclear Magnetic Resonance*; The Royal Society of Chemistry: London, 2015; Vol. *44*, pp 592−616.

(49) Ángyán, A. F.; Gáspári, Z. Ensemble-based interpretations of NMR structural data to describe protein internal dynamics. *Molecules* **2013**, *18*, 10548−10567.

(50) Prompers, J. J.; Brüschweiler, R. General framework for studying the dynamics of folded and nonfolded proteins by NMR relaxation spectroscopy and MD simulation. *J. Am. Chem. Soc.* **2002**, *124*, 4522−4534.

(51) Gu, Y.; Li, D.-W.; Brüschweiler, R. NMR order parameter determination from long molecular dynamics trajectories for objective comparison with experiment. *J. Chem. Theory Comput.* **2014**, *10*, 2599−2607.

(52) Calligari, P.; Abergel, D. Multiple scale dynamics in proteins probed at multiple time scales through fluctuations of NMR chemical shifts. *J. Phys. Chem. B* **2014**, *118*, 3823−3831.

(53) Robustelli, P.; Trbovic, N.; Friesner, R. A.; Palmer, A. G., III. Conformational dynamics of the partially disordered yeast transcription factor GCN4. *J. Chem. Theory Comput.* **2013**, *9*, 5190−5200.

(54) Palmer, A. G., III. Enzyme dynamics from NMR spectroscopy. *Acc. Chem. Res.* **2015**, *48*, 457−465.

(55) Lipari, G.; Szabo, A. Effect of librational motion on fluorescence depolarization and nuclear magnetic resonance relaxation in macromolecules and membranes. *Biophys. J.* **1980**, *30*, 489−506.

(56) Lipari, G.; Szabo, A. Model-free approach to the interpretation of nuclear magnetic resonance relaxation in macromolecules. 1. Theory and range of validity. *J. Am. Chem. Soc.* **1982**, *104*, 4546−4559.

(57) Sisamakis, E.; Valeri, A.; Kalinin, S.; Rothwell, P. J.; Seidel, C. A. M. Accurate single-molecule FRET studies using Multiparameter Fluorescence Detection. *Methods Enzymol.* **2010**, *475*, 455−514.

(58) Smith, T. A.; Ghiggino, K. P. A review of the analysis of complex time-resolved fluorescence anisotropy data. *Methods Appl. Fluoresc.* **2015**, *3*, No. 022001.

(59) Aragon, S.; Pecora, R. Fluorescence correlation spectroscopy and Brownian rotational diffusion. *Biopolymers* **1975**, *14*, 119−137.

(60) Werbelow, L. G.; Grant, D. M. Intramolecular Dipolar Relaxation in Multispin Systems. *Adv. Magn. Opt. Reson.* **1977**, *9*, 189−299.

(61) Kask, P.; Piksarv, P.; Pooga, M.; Mets, U.; Lippmaa, E. Separation of the rotational contribution in fluorescence correlation experiments. *Biophys. J.* **1989**, *55*, 213−220.

(62) Merzbacher, E. *Quantum mechanics*; Wiley: New York, 1998.

(63) Woessner, D. E. Nuclear spin relaxation in ellipsoids undergoing rotational Brownian motion. *J. Chem. Phys.* **1962**, *37*, 647−654.

(64) Clore, G. M.; Szabo, A.; Bax, A.; Kay, L. E.; Driscoll, P. C.; Gronenborn, A. M. Deviations from the simple two-parameter model-free approach to the interpretation of nitrogen-15 nuclear magnetic relaxation of proteins. *J. Am. Chem. Soc.* **1990**, *112*, 4989−4991.

(65) Levitt, M. H. *Spin dynamics: basics of nuclear magnetic resonance*; John Wiley & Sons: New York, NY, USA, 2008.

(66) Cavanagh, J.; Fairbrother, W. J.; Palmer, A. G., III; Rance, M.; Skelton, N. J. *Protein NMR Spectroscopy*, 2nd ed.; Elsevier Academic Press: Burlington, 2007.

(67) d'Auvergne, E. J.; Gooley, P. R. Model-free model elimination: a new step in the model-free dynamic analysis of NMR relaxation data. *J. Biomol. NMR* **2006**, *35*, 117−135.

(68) Kay, L. E.; Torchia, D. A.; Bax, A. Backbone dynamics of proteins as studied by nitrogen-15 inverse detected heteronuclear NMR spectroscopy: application to staphylococcal nuclease. *Biochemistry* **1989**, *28*, 8972−8979.

(69) d'Auvergne, E. J.; Gooley, P. R. Optimisation of NMR dynamic models I. Minimisation algorithms and their performance within the model-free and Brownian rotational diffusion spaces. *J. Biomol. NMR* **2008**, *40*, 107−119.

(70) d'Auvergne, E. J.; Gooley, P. R. Optimisation of NMR dynamic models II. A new methodology for the dual optimization of the model-free parameters and the Brownian rotational diffusion tensor. *J. Biomol. NMR* **2008**, *40*, 121−133.

(71) Ehrenberg, M.; Rigler, R. Rotational Brownian motion and fluorescence intensify fluctuations. *Chem. Phys.* **1974**, *4*, 390−401.

(72) Schaffer, J.; Volkmer, A.; Eggeling, C.; Subramaniam, V.; Striker, G.; Seidel, C. A. M. Identification of single molecules in aqueous solution by time-resolved fluorescence anisotropy. *J. Phys. Chem. A* **1999**, *103*, 331−336.

(73) Yguerabide, J.; Epstein, H. F.; Stryer, L. Segmental flexibility in an antibody molecule. *J. Mol. Biol.* **1970**, *51*, 573−590.

(74) Perrin, F. Polarisation de la lumière de fluorescence. Vie moyenne des molécules dans l'etat excité. *J. Phys. Radium* **1926**, *7*, 390−401.

(75) Wang, H.; Bedford, F. K.; Brandon, N. J.; Moss, S. J.; Olsen, R. W. GABA(A)-receptor-associated protein links GABA(A) receptors and the cytoskeleton. *Nature* **1999**, *397*, 69−72.

(76) Wang, H.; Olsen, R. W. Binding of the GABA(A) receptor-associated protein (GABARAP) to microtubules and microfilaments suggests involvement of the cytoskeleton in GABARAPGABA(A) receptor interaction. *J. Neurochem.* **2000**, *75*, 644−655.

(77) Leil, T. A.; Chen, Z.-W.; Chang, C.-S. S.; Olsen, R. W. GABAA receptor-associated protein traffics GABAA receptors to the plasma membrane in neurons. *J. Neurosci.* **2004**, *24*, 11429−11438.

(78) Mohrlüder, J.; Schwarten, M.; Willbold, D. Structure and potential function of γ-aminobutyrate type A receptor-associated protein. *FEBS J.* **2009**, *276*, 4989−5005.

(79) Kittler, J. T.; Rostaing, P.; Schiavo, G.; Fritschy, J.-M.; Olsen, R.; Triller, A.; Moss, S. J. The subcellular distribution of GABARAP and its ability to interact with NSF suggest a role for this protein in the intracellular transport of GABA(A) receptors. *Mol. Cell. Neurosci.* **2001**, *18*, 13−25.

(80) Ma, P.; Schwarten, M.; Schneider, L.; Boeske, A.; Henke, N.; Lisak, D.; Weber, S.; Mohrlüder, J.; Stoldt, M.; Strodel, B.; et al. Interaction of Bcl-2 with the autophagy-related GABAA receptor-associated protein (GABARAP): biophysical characterization and functional implications. *J. Biol. Chem.* **2013**, *288*, 37204−37215.

(81) Schwarten, M.; Mohrlüder, J.; Ma, P.; Stoldt, M.; Thielmann, Y.; Stangler, T.; Hersch, N.; Hoffmann, B.; Merkel, R.; Willbold, D. Nix directly binds to GABARAP: A possible crosstalk between apoptosis and autophagy. *Autophagy* **2009**, *5*, 690−698.

(82) Schwarten, M.; Stoldt, M.; Mohrlüder, J.; Willbold, D. Solution structure of Atg8 reveals conformational polymorphism of the N-terminal domain. *Biochem. Biophys. Res. Commun.* **2010**, *395*, 426−431.

(83) Coyle, J. E.; Qamar, S.; Rajashankar, K. R.; Nikolov, D. B. Structure of GABARAP in two conformations: Implications for GABA(A) receptor localization and tubulin binding. *Neuron* **2002**, *33*, 63−74.

(84) Findeisen, M.; Brand, T.; Berger, S. A 1H-NMR thermometer suitable for cryoprobes. *Magn. Reson. Chem.* **2007**, *45*, 175−178.

(85) Delaglio, F.; Grzesiek, S.; Vuister, G. W.; Zhu, G.; Pfeifer, J.; Bax, A. NMRPipe: A multidimensional spectral processing system based on UNIX pipes. *J. Biomol. NMR* **1995**, *6*, 277−293.

(86) Farrow, N. A.; Muhandiram, R.; Singer, A. U.; Pascal, S. M.; Kay, C. M.; Gish, G.; Shoelson, S. E.; Pawson, T.; Forman-Kay, J. D.; Kay, L. E. Backbone dynamics of a free and phosphopeptide-complexed Src homology 2 domain studied by 15N NMR relaxation. *Biochemistry* **1994**, *33*, 5984−6003.

(87) Korzhnev, D. M.; Skrynnikov, N. R.; Millet, O.; Torchia, D. A.; Kay, L. E. An NMR experiment for the accurate measurement of heteronuclear spin-lock relaxation rates. *J. Am. Chem. Soc.* **2002**, *124*, 10743−10753.

(88) Orekhov, V. Y.; Ibraghimov, I. V.; Billeter, M. MUNIN: a new approach to multi-dimensional NMR spectra interpretation. *J. Biomol. NMR* **2001**, *20*, 49−60.

(89) Korzhnev, D. M.; Ibraghimov, I. V.; M, M. B.; Orekhov, V. Y. MUNIN: application of three-way decomposition to the analysis of heteronuclear NMR relaxation data. *J. Biomol. NMR* **2001**, *21*, 263−268.

(90) Johnson, B. A.; Blevins, R. A. NMRView: A computer program for the visualization and analysis of NMR data. *J. Biomol. NMR* **1994**, *4*, 603−614.

(91) Pawley, N. H.; Wang, C.; Koide, S.; Nicholson, L. K. An improved method for distinguishing between anisotropic tumbling and chemical exchange in analysis of ^{15}N relaxation parameters. *J. Biomol. NMR* **2001**, *20*, 149−165.

(92) Knight, D.; Harris, R.; McAlister, M. S.; Phelan, J. P.; Geddes, S.; Moss, S. J.; Driscoll, P. C.; Keep, N. H. The X-ray crystal structure and putative ligand-derived peptide binding properties of gamma-aminobutyric acid receptor type A receptor-associated protein. *J. Biol. Chem.* **2002**, *277*, 5556−5561.

(93) Schwieters, C. D.; Kuszewski, J. D.; Tjandra, N.; Clore, G. M. The XPLOR-NIH NMR molecular structure determination package. *J. Magn. Reson.* **2003**, *160*, 65−73.

(94) Brünger, A. T. *X-PLOR, version 3.1. A system for X-ray crystallography and NMR*; Yale University Press: New Haven, CT, 1992.

(95) Dosset, P.; Hus, J.-C.; Blackledge, M.; Marion, D. Efficient analysis of macromolecular rotational diffusion from heteronuclear relaxation data. *J. Biomol. NMR* **2000**, *16*, 23−28.

(96) d'Auvergne, E. J.; Gooley, P. R. The use of model selection in the model-free analysis of protein dynamics. *J. Biomol. NMR* **2003**, *25*, 25−39.

(97) d'Auvergne, E. J.; Gooley, P. R. Set theory formulation of the model-free problem and the diffusion seeded model-free paradigm. *Mol. BioSyst.* **2007**, *3*, 483−393.

(98) Lakomek, N.-A.; Ying, J.; Bax, A. Measurement of ^{15}N relaxation rates in perdeuterated proteins by TROSY-based methods. *J. Biomol. NMR* **2012**, *53*, 209−221.

(99) Altieri, A. S.; Hinton, D. P.; Byrd, R. A. Association of biomolecular systems via pulsed field gradient NMR self-diffusion measurements. *J. Am. Chem. Soc.* **1995**, *117*, 7566−7567.

(100) Wu, D. H.; Chen, A. D.; Johnson, C. S. An improved diffusion-ordered spectroscopy experiment incorporating bipolar-gradient pulses. *J. Magn. Reson., Ser. A* **1995**, *115*, 260−264.

(101) Piotto, M.; Saudek, V.; Sklenár, V. Gradient-tailored excitation for single-quantum NMR spectroscopy of aqueous solutions. *J. Biomol. NMR* **1992**, *2*, 661−665.

(102) Stejskal, E. O.; Tanner, J. E. Spin diffusion measurements: spin echoes in the presence of a time-dependent field gradient. *J. Chem. Phys.* **1965**, *42*, 288−292.

(103) Cho, C. H.; Urquidi, J.; Singh, S.; Robinson, G. W. Thermal offset viscosities of liquid H_2O, D_2O, and T_2O. *J. Phys. Chem. B* **1999**, *103*, 1991−1994.

(104) Wilkins, D. K.; Grimshaw, S. B.; Receveur, V.; Dobson, C. M.; Jones, J. A.; Smith, L. J. Hydrodynamic radii of native and denatured proteins measured by pulse field gradient NMR techniques. *Biochemistry* **1999**, *38*, 16424−16431.

(105) Karolin, J.; Johansson, L. B. A.; Strandberg, L.; Ny, T. Fluorescence and absorption spectroscopic properties of Dipyrrometheneboron Difluoride (BODIPY) derivatives in liquids, lipid membranes, and proteins. *J. Am. Chem. Soc.* **1994**, *116*, 7801−7806.

(106) Felekyan, S.; Kuhnemuth, R.; Kudryavtsev, V.; Sandhagen, C.; Becker, W.; Seidel, C. A. M. Full correlation from picoseconds to seconds by time-resolved and time-correlated single photon detection. *Rev. Sci. Instrum.* **2005**, *76*, No. 083104.

(107) Ortega, A.; Amorós, D.; García de la Torre, J. Prediction of hydrodynamic and other solution properties of rigid proteins from atomic- and residue-level models. *Biophys. J.* **2011**, *101*, 892−898.

(108) Stangler, T.; Mayr, L. M.; Willbold, D. Solution structure of human GABA(A) receptor-associated protein GABARAP: implications for biolgoical funcrion and its regulation. *J. Biol. Chem.* **2002**, *277*, 13363−13366.

(109) Weiergräber, O. H.; Stangler, T.; Thielmann, Y.; Mohrlüder, J.; Wiesehan, K.; Willbold, D. Ligand binding mode of GABAA receptor-associated protein. *J. Mol. Biol.* **2008**, *381*, 1320−1331.

(110) Kouno, T.; Miura, K.; Kanematsu, T.; Shirakawa, M.; Hirata, M.; Kawano, K. 1H, 13C and 15N resonance assignments of GABARAP, GABAA receptor associated protein. *J. Biomol. NMR* **2002**, *22*, 97−98.

(111) Pronk, S.; et al. GROMACS 4.5: a high-throughput and highly parallel open source molecular simulation toolkit. *Bioinformatics* **2013**, *29*, 845−854.

(112) Lindorff-Larsen, K.; Piana, S.; Palmo, K.; Maragakis, P.; Klepeis, J. L.; Dror, R. O.; Shaw, D. E. Improved side-chain torsion potentials for the Amber ff99SB protein force field. *Proteins: Struct., Funct., Genet.* **2010**, *78*, 1950−1958.

(113) Jorgensen, W. L.; Chandrasekhar, J.; Madura, J. D.; Impey, R. W.; Klein, M. L. Comparison of simple potential functions for simulating liquid water. *J. Chem. Phys.* **1983**, *79*, 926−935.

(114) Hoover, W. G. Canonical dynamics: equilibrium phase-space distributions. *Phys. Rev. A: At., Mol., Opt. Phys.* **1985**, *31*, 1695−1697.

(115) Darden, T.; Perera, L.; Li, L.; Pedersen, L. New tricks for modelers from the crystallography toolkit: the particle mesh Ewald algorithm and its use in nucleic acid simulations. *Structure* **1999**, *7*, R55.

(116) Hess, B. P-LINCS: A parallel linear constraint solver for molecular simulation. *J. Chem. Theory Comput.* **2008**, *4*, 116−122.

(117) Maragakis, P.; Lindorff-Larsen, K.; Eastwood, M. P.; Dror, R. O.; Klepeis, J. L.; Arkin, I. T.; Jensen, M. Ø.; Xu, H.; Trbovic, N.; Friesner, R. A. Microsecond molecular dynamics simulation shows effect of slow loop dynamics on backbone amide order parameters of proteins. *J. Phys. Chem. B* **2008**, *112*, 6155−6158.

(118) Burnham, K. P.; Anderson, D. R. Multimodel inference understanding AIC and BIC in model selection. *Sociol. Methods Res.* **2004**, *33*, 261−304.

(119) Kühnemuth, R.; Seidel, C. A. M. Principles of Single Molecule Multiparameter Fluorescence Spectroscopy. *Single Mol.* **2001**, *2*, 251−254.

(120) Borst, J. W.; Laptenok, S. P.; Westphal, A. H.; Kühnemuth, R.; Hornen, H.; Visser, N. V.; Kalinin, S.; Aker, J.; van Hoek, A.; Seidel, C. A. M.; et al. Structural changes of yellow cameleon domains observed by quantitative FRET analysis and polarized fluorescence correlation spectroscopy. *Biophys. J.* **2008**, *95*, 5399−5411.

(121) Bergström, F.; Mikhalyov, I.; Hagglof, P.; Wortmann, R.; Ny, T.; Johansson, L. B. A. Dimers of dipyrrometheneboron difluoride (BODIPY) with light spectroscopic applications in chemistry and biology. *J. Am. Chem. Soc.* **2002**, *124*, 196−204.

(122) Mao, Y.; Zhang, Y. Thermal conductivity, shear viscosity and specific heat of rigid water models. *Chem. Phys. Lett.* **2012**, *542*, 37−41.

(123) Shi, J. X.; Tai, K.; McCammon, J. A.; Taylor, P.; Johnson, D. A. Nanosecond dynamics of the mouse acetylcholinesterase Cys(69)-Cys(96) omega loop. *J. Biol. Chem.* **2003**, *278*, 30905−30911.

(124) Alexiev, U.; Rimke, I.; Pohlmann, T. Elucidation of the nature of the conformational changes of the EF-interhelical loop in bacteriorhodopsin and of the helix VIII on the cytoplasmic surface of bovine rhodopsin: A time-resolved fluorescence depolarization study. *J. Mol. Biol.* **2003**, *328*, 705−719.

(125) Lee, A. L.; Kinnear, S. A.; Wand, A. J. Redistribution and loss of side chain entropy upon formation of a calmodulin-peptide complex. *Nat. Struct. Biol.* **2000**, *7*, 72−77.

(126) Huber, M. L.; Perkins, R. A.; Laesecke, A.; Friend, D. G.; Sengers, J. V.; Assael, M. J.; Metaxa, I. N.; Vogel, E.; Mares, R.; Miyagawa, K. New International Formulation for the Viscosity of H2O. *J. Phys. Chem. Ref. Data* **2009**, *38*, 101−125.

(127) Zhang. Viscosity and Density of Water + Sodium Chloride + Potassium Chloride Solutions at 298.15 K. *J. Chem. Eng. Data* **1996**, *41*, 516−520.

(128) Damberg, P.; Jarvet, J.; Allard, P.; Mets, U.; Rigler, R.; Graslund, A. ^{13}C-^{1}H NMR relaxation and fluorescence anisotropy decay study of tyrosine dynamics in motilin. *Biophys. J.* **2002**, *83*, 2812−2825.

(129) Roosen-Runge, F.; Hennig, M.; Zhang, F.; Jacobs, R. M.; Sztucki, M.; Schober, H.; Seydel, T.; Schreiber, F. Protein self-diffusion in crowded solutions. *Proc. Natl. Acad. Sci. U. S. A.* **2011**, *108*, 11815−11820.

(130) Bernado, P.; Garcia de la Torre, J.; Pons, M. Macromolecular crowding in biological systems: hydrodynamics and NMR methods. *J. Mol. Recognit.* **2004**, *17*, 397−407.

(131) Nymann-Andersen, J.; Wang, H.; Olsen, R. W. Biochemical identification of the binding domain in the GABA(A) receptor-associated protein (GABARAP) mediating dimer formation. *Neuropharmacology* **2002**, *43*, 476−481.

(132) Pacheco, V.; Ma, P.; Thielmann, Y.; Hartmann, R.; Weiergräber, O. H.; Mohrlüder, J.; Willbold, D. Assessment of GABARAP self-association by its diffusion properties. *J. Biomol. NMR* **2010**, *48*, 49−58.

(133) Weiergräber, O. H.; Mohrlüder, J.; Willbold, D. In *Autophagy - A Double-Edged Sword - Cell Survival or Death?*; Bailly, Y., Ed.; INTECH Open Access Publisher: Rijeka, 2013; Vol. 2, pp 13−45.

(134) Kaufmann, A.; Beier, V.; Franquelim, H. G.; Wollert, T. Molecular mechanism of autophagic membrane-scaffold assembly and disassembly. *Cell* **2014**, *156*, 469−481.

(135) Ma, P.; Mohrlüder, J.; Schwarten, M.; Stoldt, M.; Singh, S. K.; Hartmann, R.; Pacheco, V.; Willbold, D. Preparation of a functional GABARAP−lipid conjugate in nanodiscs and its investigation by solution NMR spectroscopy. *ChemBioChem* **2010**, *11*, 1967−1970.

(136) Wong, V.; Case, D. A. Evaluating rotational diffusion from protein MD simulations. *J. Phys. Chem. B* **2008**, *112*, 6013−6024.

(137) Mukherjee, A.; Bagchi, B. Solvent frictional forces in the rotational diffusion of proteins in water. *Curr. Sci.* **2006**, *91*, 1208−1216.

(138) Chen, C. R.; Makhatadze, G. I. ProteinVolume: calculating molecular van der Waals and void volumes in proteins. *BMC Bioinf.* **2015**, *16*, 101.

(139) Jungwirth, P. Biological water or rather water in biology? *J. Phys. Chem. Lett.* **2015**, *6*, 2449−2451.

(140) Svergun, D. I.; Richard, S.; Koch, M. H. J.; Sayers, Z.; Kuprin, S.; Zaccai, G. Protein hydration in solution: Experimental observation by x-ray and neutron scattering. *Proc. Natl. Acad. Sci. U. S. A.* **1998**, *95*, 2267−2272.

(141) Merzel, F.; Smith, J. C. Is the first hydration shell of lysozyme of higher density than bulk water? *Proc. Natl. Acad. Sci. U. S. A.* **2002**, *99*, 5378−5383.

(142) Kurkal-Siebert, V.; Daniel, R. M.; Finney, J. L.; Tehei, M.; Dunn, R. V.; Smith, J. C. Enzyme hydration, activity and flexibility: A neutron scattering approach. *J. Non-Cryst. Solids* **2006**, *352*, 4387−4393.

(143) Vitalini, F.; Mey, A. S. J. S.; Noé, F.; Keller, B. G. Dynamic properties of force fields. *J. Chem. Phys.* **2015**, *142*, No. 084101.

(144) Dimura, M.; Peulen, T. O.; Hanke, C. A.; Prakash, A.; Gohlke, H.; Seidel, C. A. M. Quantitative FRET studies and integrative modeling unravel the structure and dynamics of biomolecular systems. *Curr. Opin. Struct. Biol.* **2016**, *40*, 163−185.

(145) Muschielok, A.; Andrecka, J.; Jawhari, A.; Bruckner, F.; Cramer, P.; Michaelis, J. A nano-positioning system for macromolecular structural analysis. *Nat. Methods* **2008**, *5*, 965−971.

(146) Beckers, M.; Drechsler, F.; Eilert, T.; Nagy, J.; Michaelis, J. Quantitative structural information from single-molecule FRET. *Faraday Discuss.* **2015**, *184*, 117−129.

(147) Adcock, S. A.; McCammon, J. A. Molecular dynamics: Survey of methods for simulating the activity of proteins. *Chem. Rev.* **2006**, *106*, 1589−1615.

(148) Wriggers, W.; Schulten, K. Protein domain movements: Detection of rigid domains and visualization of hinges in comparisons of atomic coordinates. *Proteins: Struct., Funct., Genet.* **1997**, *29*, 1−14.

(149) Hayward, S. Structural principles governing domain motions in proteins. *Proteins: Struct., Funct., Genet.* **1999**, *36*, 425−435.

(150) Kumeta, H.; Watanabe, M.; Nakatogawa, H.; Yamaguchi, M.; Ogura, K.; Adachi, W.; Fujioka, Y.; Noda, N. N.; Ohsumi, Y.; Inagaki, F. The NMR structure of the autophagy-related protein Atg8. *J. Biomol. NMR* **2010**, *47*, 237−241.

(151) Miao, Y. L.; McCammon, J. A. Unconstrained enhanced sampling for free energy calculations of biomolecules: a review. *Mol. Simul.* **2016**, *42*, 1046−1055.

(152) Weidtkamp-Peters, S.; Felekyan, S.; Bleckmann, A.; Simon, R.; Becker, W.; Kühnemuth, R.; Seidel, C. A. M. Multiparameter fluorescence image spectroscopy to study molecular interactions. *Photochem. Photobiol. Sci.* **2009**, *8*, 470−480.

(153) Lidke, D. S.; Nagy, P.; Barisas, B. G.; Heintzmann, R.; Post, J. N.; Lidke, K. A.; Clayton, A. H. A.; Arndt-Jovin, D. J.; Jovin, T. M. Imaging molecular interactions in cells by dynamic and static fluorescence anisotropy (rFLIM and emFRET). *Biochem. Soc. Trans.* **2003**, *31*, 1020−1027.

(154) Soleimaninejad, H.; Chen, M. Z.; Lou, X. D.; Smith, T. A.; Hong, Y. N. Measuring macromolecular crowding in cells through fluorescence anisotropy imaging with an AIE fluorogene. *Chem. Commun.* **2017**, *53*, 2874−2877.

(155) Freedberg, D. I.; Selenko, P. Live cell NMR. *Annu. Rev. Biophys.* **2014**, *43*, 171−192.

(156) Sakon, J. J.; Weninger, K. R. Detecting the conformation of individual proteins in live cells. *Nat. Methods* **2010**, *7*, 203−U256.

(157) König, I.; Zarrine-Afsar, A.; Aznauryan, M.; Soranno, A.; Wunderlich, B.; Dingfelder, F.; Stüber, J. C.; Plückthun, A.; Nettels, D.; Schuler, B. Single-molecule spectroscopy of protein conformational dynamics in live eukaryotic cells. *Nat. Methods* **2015**, *12*, 773−U129.

(158) Yu, I.; Mori, T.; Ando, T.; Harada, R.; Jung, J.; Sugita, Y.; Feig, M. Biomolecular interactions modulate macromolecular structure and dynamics in atomistic model of a bacterial cytoplasm. *eLife* **2016**, *5*, No. e19274.

DOI: 10.1021/acs.jpcb.8b08903
J. Phys. Chem. B 2019, 123, 1453−1480